THE UNIVERSITY OF CHICAGO

ELECTRON-ELECTRON AND ELECTRON-PHONON INTERACTIONS IN SEMICONDUCTORS AND INSULATORS FROM MANY-BODY PERTURBATION THEORY

A DISSERTATION SUBMITTED TO
THE FACULTY OF THE DIVISION OF THE PHYSICAL SCIENCES
IN CANDIDACY FOR THE DEGREE OF
DOCTOR OF PHILOSOPHY

DEPARTMENT OF CHEMISTRY

BY
HAN YANG

CHICAGO, ILLINOIS
DECEMBER 2021

To my parents

TABLE OF CONTENTS

LIST OF FIGURES

LIST OF TABLES

ACKNOWLEDGMENTS

Firstly, I would like to thank my advisor, Professor Dr. Giulia Galli, for her kind support during the past years. Although many of my projects failed, Giulia did not give me up, and she helped me out of the difficulties. Without her encouragement and patience, I would not figure out my projects and present this dissertation.

Secondly, I thank my mentor Dr. Marco Govoni, who assisted me in every stage of my research. Marco helped me with the first Feynman diagram I drew, the first line I edited in the `WEST` code, and the first rebuttal I wrote. Whenever I have a bug in the code or get stuck in the derivations, I can always find useful advice from him.

I thank my colleagues and collaborators in the Galli group: Ryan L. McAvoy and Dr. Arpan Kundu for useful discussions of the electron-phonon interactions, Dr. He Ma for the help of GW calculations and the technical details in the `WEST` code, and Yu Jin for the help with the BSE/TDDFT code.

I express my special thanks to Chang Liu.

Finally, I thank my parents, who shared the joy and pain in my Ph.D. journey.

ABSTRACT

An accurate description of the electronic structure of semiconductors and insulators is essential in materials discovery. However, the Schrödinger equation[124] of many-body systems, e.g., electrons in solids or molecules, *cannot* be solved exactly. Many approaches have been proposed to solve approximately the Schrödinger equation of interacting electrons, and new methods and algorithms are still being developed to improve the efficiency and accuracy of the calculations, and/or to incorporate new physics.

This dissertation focuses on the developments of methods to study the electronic structure of solids, in particular electron-phonon interactions in semiconductors and insulators, using many-body perturbation theory (MBPT). We start with a brief review of existing methods to study electron-electron interactions in solids, including density functional theory (DFT)[63, 71] and post-DFT methods (GW approximation),[61, 65, 8] and methods to study electron-phonon interactions including density functional perturbation theory (DFPT).[10] Then we describe our developments to: (i) improve the efficiency of G_0W_0 calculations in Chapter 3, (ii) combine electron-electron and electron-phonon calculations in solids in Chapter 4, and (iii) compute electron-phonon interactions at the hybrid functional level of theory in Chapter 5.

First, we develop an approximation to increase the efficiency of the G_0W_0 calculations in molecules and heterogeneous systems. The G_0W_0 approximation predicts the electronic energy gap of materials, but at a higher computational cost compared to DFT. Starting from an existing implementation of the G_0W_0 method, where the dielectric function is represented using a low-rank approximation,[51] we present an algorithm to improve the efficiency of the calculations by solving an approximate form of the Sternheimer equation.[132] The method presented here speeds up the calculation by 50%, without significant loss of accuracy.

Then, we develop a method to effectively combine the calculation of electron-electron and electron-phonon interactions at the G_0W_0 level of theory in extended systems. Our

method allows for the calculations of the electron-electron and electron-phonon interaction without the separate evaluation of screening effects as well as for calculations beyond the Allen-Heine-Cardona (AHC) formalism[4].

In the last part of the dissertation, we propose a method to compute electron-phonon interactions at the level of hybrid functionals based on density matrix perturbation theory (DMPT).

CHAPTER 1

INTRODUCTION

All chemical processes obey the fundamental laws of quantum mechanics. After quantum mechanics was developed in the early 20th century and especially after the Schrödinger equation was derived in 1920s,[124] several physicists started to believe that all chemistry problems were solved and what remained was nothing but a tedious job that would solve the Schrödinger equation of molecules and solids.[33] Nevertheless, solving the Schrödinger equation for real molecules or solids turned out to be not that trivial. In the famous article *More is different*,[5] the Nobel laureate P. W. Anderson wrote "The ability to reduce everything to simple fundamental laws does not imply the ability to start from those laws and reconstruct the universe". Anderson was right, and there are still countless chemical problems that remain unsolved today, almost one century after Schödinger's equation was written. Researchers are still pursuing the developments of new methods, approximations, and numerical techniques based on the fundamental laws of quantum mechanics to explain experiments, to predict new chemistry, and to discover new materials.

In quantum chemistry, the electronic structure of a molecule or a solid is arguably one of the most fundamental properties, describing the energies of the electrons in the systems. However, the exact solution of the electronic structure problem is not possible for realistic systems, and thus many approximations to the solution of the Schrödinger equation have been proposed. Using the variational principle, the Hartree method[59] was proposed in 1927, and then followed by the Hartree-Fock (HF) method.[60] In the Hartree method, one writes the many-body wavefunction as a product of single-particle orbitals, failing to satisfy the Pauli principle.[102] This problem was fixed when the many-body wavefunction was approximated by a Slater determinant.[130] The HF method is still used today, and it is also the starting point for many higher-level theories, including configuration interactions (CI)[127] and coupled clusters (CC)[28].

While HF and its derivatives lay their foundation in the electronic wavefunctions, it is also possible to reformulate the solution of Schrödinger equation in terms of the electron densities $n(\mathbf{r})$. The Hohenberg-Kohn (HK) theorems established the one-on-one mapping between the external potential acting on the system of electrons and the electronic density.[63] As a result, the dimensionality of the system containing N electrons was *in principle* reduced from $3N$ to 3. However, the HK theorem does not provide any practical solutions to the Schrödinger equation. Inspired by orbital-based methods, the Kohn-Sham formalism was derived and it is the de facto standard formulation of DFT theory calculations used today.[71] The Kohn-Sham equation maps the interacting system to an artificial non-interacting system that shares the same electron density, and solves for the single-particle orbitals of the non-interacting system. In the derivation of the Kohn-Sham formalism, the exchange-correlation potential V_{xc} was introduced whose exact expression is unknown. To apply the Kohn-Sham formalism to realistic materials, proper approximate forms of the exchange-correlation potential must be chosen. Examples of approximate exchange-correlation functionals include the local density approximation (LDA),[105] the generalized gradient approximations (GGA),[103, 12] and hybrid functionals.[13, 104] We will explore the Kohn-Sham formalism in more detail in Chapter 2.

Despite the success of DFT in many applications,[21] the approximate forms of the theory suffer from inaccuracies including energy gap underestimations and poor description of the long-range interaction in several weekly bonded solids.[141, 91] The many-body perturbation theory (MBPT) was proposed as an alternative formulation of the Schrödinger equation using Green's functions.[61] It improves over DFT calculations by considering dynamically screened interactions. The dynamical screening effects are computationally demanding, thus the first *GW* calculation[65] was done twenty years after the MBPT was proposed. Since then, many implementations of the *GW* approximation were proposed in the literature, and they are included in codes such as `BerkeleyGW`,[32, 66, 120] `Yambo`,[89] `Abinit`,[48]

SternheimerGW[45, 73] and the WEST[51] code, developed in our group. These implementations take advantage of different techniques to speed up the calculations. For example, to compute the frequency integration of the *GW* self-energy, the plasmon-pole model (PPM) has been used to speed up the frequency integration in BerkeleyGW, Yambo, and Abinit, while an analytical continuation is used in SternheimerGW. WEST adopted the Lanczos algorithm[74] as well as the contour deformation technique to obtain self-energies with high accuracy. To improve the convergence of the summation of empty bands, the so-called simple approximate physical orbitals (SAPO)[121] are used in BerkeleyGW. In WEST, we approximate the dielectric function with its low-rank decomposition, which usually exhibits fast convergence, and the summation of empty bands is completely circumvented. In Chapter 3, we will present a method to approximate the low-rank decomposition of the dielectric function implemented in the WEST code that reduces the computational cost of the *GW* approximation without significant loss of accuracy.[147]

The above methods to compute the electronic structure of solids and molecules rely on the Born-Oppenheimer (BO) approximation, and do not include the effect of the ionic vibrations on the electronic structure. However, the interactions between the electrons and the motions of ions, i.e., phonons, are responsible for many phenomena, including thermal transport,[14, 85] conventional super-conductivity,[9] and the electron-phonon renormalization of energy levels[4, 6, 148, 72].

Early studies of the electron-phonon interaction relied on semi-empirical models,[15, 36] e.g., the Fröhlich model.[36], and it is only in recent years that electron-phonon interactions were computed from first principles. As the dynamical matrices[88] are defined as the second derivative of the total energy and the electron-phonon renormalizations of energy levels are defined as the derivative of energy levels relative to ionic positions, the straightforward approach to compute electron-phonon interaction is to displace atomic positions by finite differences and evaluate the derivatives numerically.[27, 6, 24] The finite difference approach

is known as the frozen-phonon (FPH) method,[27, 6, 24] and its application is limited as it converges slowly as a function of the size of the supercell. Other methods to study electron-phonon interactions are molecular dynamics (MD)[35, 68] and path-integral molecular dynamics (PIMD)[113, 114, 72]. The PIMD and MD approaches incorporate the temperature dependence of electron-phonon interactions and go beyond the harmonic approximation[72], and the former also includes nuclear quantum effects.

In this dissertation, we focus on density functional perturbation theory (DFPT)[10, 42], which is widely adopted to compute phonon frequencies and electron-phonon coupling matrices, and FPH or PIMD methods are only used to verify our results when needed.

In the past decades, the DFPT was first implemented to compute phonon frequencies in the `PHonon` package as a part of the `Quantum Espresso` code[41, 40] and it was later implemented in other codes such as `Abinit`.[48] The DFPT was used, for example, to compute electron-phonon interactions in diamond[44, 45] within the Allen-Heine-Cardona (AHC) formalism.[4, 3] However, the AHC formalism relied on a set of approximations, that might lead to an incorrect description of the electron-phonon self-energies in certain systems. Thus, other studies tried to understand how these approximations affect the computed self-energies by including dynamical effects[22, 23] and non-adiabaticity[23, 23, 93] of the Fan-Migdal part of the self-energy, and by eliminating the rigid-ion approximation (RIA)[109, 110] of the Debye-Waller part of the self-energy.

To speed up the convergence of electron-phonon calculations based on DFPT, many researchers interpolated electron-phonon coupling matrices using a real-space basis. For example, Wannier functions[108] are used in the `EPW` code as a part of `Quantum Espresso`,[111] atomic orbitals are used in the `Perturbo` code,[149] and the Fourier interpolation is used in the `Abinit` code[48]. These interpolation techniques make it possible to converge electron-phonon interactions with dense sampling of the Brillouin zone.

In Chapter 4, we are interested in understanding how G_0W_0 corrections affect the com-

puted electron-phonon self-energies at the DFT level, and we developed a protocol to combine the calculations of electron-electron interactions at the GW level of theory with the calculations of electron-phonon interactions in solids, without repeating the calculation of the dielectric screening. We carried out calculations of defects in diamond to show the ability of our approach to deal with large-scale systems. Moreover, we showed that our implementation is capable of going beyond the widely used AHC formalism.

The calculations described so far used DFPT on top of DFT wavefunctions obtained at the LDA/GGA level of theory. In Chapter 5, we present a method to compute phonons and electron-phonon interactions at the hybrid functional level of theory based on density matrix perturbation theory.

We conclude the dissertation with a brief summary of the methods we developed to compute the electron-electron and electron-phonon interactions as well as the possible directions for further research that this dissertation points toward..

CHAPTER 2

THEORETICAL FOUNDATIONS

In this chapter, we describe the theoretical foundations on which our methodological developments are based. We begin with a description of the electronic structure problem in Section 2.1. Then we go through existing methods to study electron-electron and electron-phonon interactions. We introduce Density Functional Theory (DFT) in Section 2.2, and the *GW* approximation based on Many-body Perturbation Theory (MBPT) in Section 2.3. To compute electron-phonon interaction, we summarize Density Functional Perturbation Theory (DFPT) in Section 2.4, as well as Density Matrix Perturbation Theory (DMPT), which is the foundation of our recently proposed method described in Chapter 5.

2.1 The electronic structure problem

The Born-Oppenheimer (BO) approximation[16] assumes that electrons move much faster than ions and thus we can decouple the Schrödinger equation into an electronic and ionic part. Within the BO approximation, the time-independent Schrödinger's equation of a many-body system with N electrons is,[90, 53]

$$H\Psi_0(\mathbf{r}_1, \mathbf{r}_2, \cdots, \mathbf{r}_N) = E_0\Psi_0(\mathbf{r}_1, \mathbf{r}_2, \cdots, \mathbf{r}_N), \tag{2.1}$$

where H is the Hamiltonian of the system, E_0 and Ψ_0 are the ground state total energy and ground state N-particle wavefunction, and $\mathbf{r}_1$, $\mathbf{r}_2$, $\cdots$, $\mathbf{r}_N$ are the coordinates of the electrons.

The Hamiltonian H can be decomposed into several terms: the kinetic energies of the

electrons, electron-electron Coulomb interactions, and electron-ion Coulomb interactions,[53]

$$H = -\frac{1}{2}\sum_{i}^{N}\nabla_i^2 + \sum_{i}^{N}\sum_{j>i}^{N}\frac{1}{|\mathbf{r}_i - \mathbf{r}_j|} - \sum_{i}^{N}\sum_{I}^{\text{ion}}\frac{Z_I}{|\mathbf{r}_i - \mathbf{R}_I|}, \tag{2.2}$$

where i, j are the indices of electrons, I is the index of ions, Z_I is the nuclear charge of I-th ion and we assume Hartree atomic unit $\hbar = m_e = e = 1$. The direct and exact solution of the Schrödinger's equation is only possible for a limited subset of systems, a famous example being the hydrogen atom.[53] Thus one has to employ physical numerical approximations to solve the Schrödinger equations for a given material. In 1929, the many-body wavefunction was written using a Slater determinant of a set of single-particle wavefunctions,[130]

$$\Psi(\mathbf{r}_1, \mathbf{r}_2, \cdots, \mathbf{r}_N) = \frac{1}{\sqrt{N!}}\begin{vmatrix} \psi_1(\mathbf{r}_1) & \psi_2(\mathbf{r}_1) & \cdots & \psi_N(\mathbf{r}_1) \\ \psi_1(\mathbf{r}_2) & \psi_2(\mathbf{r}_2) & \cdots & \psi_N(\mathbf{r}_2) \\ \vdots & \vdots & \ddots & \vdots \\ \psi_1(\mathbf{r}_N) & \psi_2(\mathbf{r}_N) & \cdots & \psi_N(\mathbf{r}_N) \end{vmatrix}, \tag{2.3}$$

where $\psi(\mathbf{r})$ is a single-particle wavefunction and we omit spins for simplicity. It is worth noting that the use of a single Slater determinant fails for some systems, e.g., systems with strong correlation, but such systems are beyond the scope of this dissertation. Using a Slater determinant, solving the Schrödinger equation for N-particle wavefunction $\Psi(\mathbf{r}_1, \mathbf{r}_2, \cdots, \mathbf{r}_N)$ is equivalent to solve for a set of single-particle wavefunctions $\psi_i(\mathbf{r})$ and their corresponding energies ε_i.

The electronic structure problem studied in this dissertation is formulated in terms of solution for the pairs of energy levels and single-particle wavefunctions (ε_i, ψ_i) *for a given system.* Among the existing methods, we will introduce density functional theory (DFT)[63, 71, 90] and many-body perturbation theory (MBPT)[91, 55, 61].

The discussion above deals purely with the electron-electron interactions, but electron-

phonon interactions are known to affect the electronic energy levels ε_i.[43] Thus, to obtain an accurate description of the electronic structures of solids and molecules, it is necessary to study the effect of electron-phonon interaction on the energy levels. In this chapter, we will introduce density functional perturbation theory (DFPT) to compute phonon frequencies and electron-phonon coupling matrices in Section 2.4 and Section 2.5, and density matrix perturbation thoery (DMPT) in Section 2.7.

2.2 Density functional theory (DFT)

2.2.1 The Kohn-Sham equations

Density functional theory (DFT)[63] is arguably the most widely used theory in the computational chemistry community. It formulates the electronic structure problem in terms of charge densities $n(\mathbf{r})$ rather than wavefunctions. For a system with N electrons, DFT significantly reduces the dimension of the problem from $3N$ to 3.

The idea to connect the physical observables of interacting systems with the electronic charge density $n(\mathbf{r})$ is old and can be traced back to the Thomas-Fermi (TF) model,[137], where the kinetic energy (T) is written as,

$$T = C_{\mathrm{TF}} \int [n(\mathbf{r})]^{5/3} \mathrm{d}\mathbf{r}, \tag{2.4}$$

where C_{TF} is a constant prefactor. The TF model was inaccurate for many systems except simple metals and lacked mathematical and physical rigor. The proof of the mapping between charge densities and physical observables was proposed many years later in the two Honhenberg-Kohn (HK) theorems,[63]

1. The external potentials $V_{\mathrm{ext}}(\mathbf{r})$ and hence the total energies of the interacting electronic system are unique functionals of the ground-state charge densities $n(\mathbf{r})$;

2. The total energies of the interacting system can be written as a functional in terms of the charge density,

$$E_{\mathrm{HK}}[n(\mathbf{r})] = F_{\mathrm{HK}}[n(\mathbf{r})] + \int V_{\mathrm{ext}}(\mathbf{r}) n(\mathbf{r}) \mathrm{d}\mathbf{r}, \tag{2.5}$$

where F_{HK} is a universal functional. The charge density that minimizes the functional E_{HK} is guaranteed to be the exact ground-state charge density of the interacting system.

The first HK theorem establishes a one-on-one mapping between the ground-state charge density of the interacting system and the external potentials it feels, and the second HK theorem indicates the total energy and ground-state charge density can be obtained using the variational principle. However, the functional F_{HK} is unknown, thus the HK theorems cannot be applied to study materials directly.

A practical formalism that can be applied to realistic materials was proposed one year after the HK theorems, and is known as the Kohn-Sham (KS) formalism.[71] The Kohn-Sham formalism introduces a non-interacting system that has the same charge density as the interacting system, and the total energy functional of the non-interacting system is written as,

$$E_{\mathrm{HK}}[n] = T_0[n] + E_{\mathrm{H}}[n] + E_{\mathrm{xc}}[n] + \int V_{\mathrm{ext}}(\mathbf{r}) n(\mathbf{r}) \mathrm{d}\mathbf{r}, \tag{2.6}$$

where $T_0[n]$ is the kinetic energy of the non-interacting system, $E_{\mathrm{H}}[n]$ is the Coulomb interactions between electrons in the non-interacting system,

$$E_{\mathrm{H}}[n] = \frac{1}{2} \iint \frac{n(\mathbf{r}) n(\mathbf{r}')}{|\mathbf{r} - \mathbf{r}'|^2} \mathrm{d}\mathbf{r} \mathrm{d}\mathbf{r}' \tag{2.7}$$

and E_{xc} is the exchange-correlation energy defined as,

$$E_{\mathrm{xc}}[n] = F_{\mathrm{HK}}[n] - T_0[n] - E_{\mathrm{H}}[n]. \tag{2.8}$$

By minimizing the HK energy in Eq. (2.6), one obtains the famous Kohn-Sham equations,

$$H^{\mathrm{KS}}\psi_n(\mathbf{r}) = \varepsilon_n\psi_n(\mathbf{r}), \tag{2.9}$$

where the eigenvalue ε_n and the eigenvector ψ_n are Kohn-Sham single-particle energy levels and orbitals. When periodic systems are studied and $\mathbf{k}$ point sampling is used, the Kohn-Sham equations are solved at every $\mathbf{k}$ point,

$$H^{\mathrm{KS}}\psi_{n\mathbf{k}}(\mathbf{r}) = \varepsilon_{n\mathbf{k}}\psi_{n\mathbf{k}}(\mathbf{r}). \tag{2.10}$$

H^{KS} is the Kohn-Sham Hamiltonian,

$$\begin{aligned} H^{\mathrm{KS}} &= K + V_{\mathrm{scf}} \\ &= -\frac{1}{2}\nabla^2 + V_{\mathrm{H}} + V_{\mathrm{ext}} + V_{\mathrm{xc}}, \end{aligned} \tag{2.11}$$

where $K = -1/2\nabla^2$ is the kinetic operator, the Hartree potential is

$$V_{\mathrm{H}}(\mathbf{r}) = \int \frac{n(\mathbf{r}')}{|\mathbf{r} - \mathbf{r}'|}\mathrm{d}\mathbf{r}', \tag{2.12}$$

the external potential is

$$V_{\mathrm{ext}}(\mathbf{r}) = -\sum_I \frac{Z_I}{|\mathbf{r} - \mathbf{R}_I|^2} \tag{2.13}$$

and the exchange-correlation potential is defined as the functional derivative of exchange-correlation energy

$$V_{\mathrm{xc}}(\mathbf{r}) = \frac{\delta E_{\mathrm{xc}}}{\delta n(\mathbf{r})}. \tag{2.14}$$

For convenience, we define the short-hand notation

$$V_{\mathrm{Hxc}} = V_{\mathrm{H}} + V_{\mathrm{xc}} \tag{2.15}$$

and it will be used later in our phonon calculations.

By solving the Kohn-Sham equations (2.9), the charge density can be constructed from the Kohn-Sham wavefunctions,

$$n(\mathbf{r}) = 2 \sum_{n}^{N_{\text{occ}}} |\psi_n(\mathbf{r})|^2, \tag{2.16}$$

where the summation runs over occupied bands and the prefactor 2 accounts for spin.

It is worth noting that the HK theorems do not require the introduction of wavefunctions, and the wavefunctions in the Kohn-Sham equation are introduced to carry out practical calculations. An orbital-free density function theory (OF-DFT)[78] has been proposed, but it is beyond the discussion of the current dissertation since it works best for metals.

2.2.2 Approximations to the exchange-correlation functionals

The exact expression of the exchange-correlation potential is unknown, thus proper approximations must be made to do practical calculations.

One of the most famous approximate exchange-correlation potential is the local density approximation (LDA), which explicitly writes the exchange-correlation potential as a functional of the electron density,[105] and it was derived from the homogeneous electron gas model (HEG).

$$E_{\text{xc}} = \int V_{\text{xc}}^{\text{HEG}}[n(\mathbf{r})] n(\mathbf{r}) \mathrm{d}\mathbf{r} \tag{2.17}$$

Although HEG is a coarse model and it does not reflect the charge density in most real materials, LDA functionals succeeded in the description of some solids in the early days of DFT calculations.

To improve the performance of the LDA, the generalized gradient approximation (GGA) was proposed, which writes the exchange-correlation potential as a functional of the electron

density and its gradient,[103]

$$E_{\mathrm{xc}} = \int V_{\mathrm{xc}}^{\mathrm{GGA}}[n(\mathbf{r}), \nabla n(\mathbf{r})] n(\mathbf{r}) \mathrm{d}\mathbf{r} \tag{2.18}$$

The widely-used PBE functional is a famous example of this category.[103]

In LDA and GGA, the exchange potentials are local in space. However, the exchange interaction is known to be non-local.[90] To account for the non-locality of the exchange interaction, a portion of Hartree-Fock exchange is added to the exchange-correlation functional, and such approximate functionals are called hybrid functionals. As an example, the PBE0 functional[1] has the following form,

$$V_{\mathrm{xc}}^{\mathrm{PBE0}}(\mathbf{r}, \mathbf{r}') = (1-\alpha) V_{\mathrm{x}}^{\mathrm{PBE}}(\mathbf{r}) + V_{\mathrm{c}}^{\mathrm{PBE}}(\mathbf{r}) + \alpha V_{\mathrm{x}}^{\mathrm{HF}}(\mathbf{r}, \mathbf{r}') \tag{2.19}$$

with α being 0.25. The dielectric-dependent hybrid (DDH) functional is another example, where the α parameter is tuned for each system using the dielectric constant.[128, 129, 18, 17]

Despite its success in many applications, the Kohn-Sham equations fail to describe the single-particle energies of real systems in many cases.[91, 141] We recall that in the derivation of the Kohn-Sham orbitals, the energy levels are those of the non-interacting system instead of the real system.

2.2.3 Solution of the Kohn-Sham equations using the planewave basis sets and pseudopotentials

In the quantum chemistry community, it is common practice to write the wavefunctions in terms of a selected set of basis functions, and planewave basis sets are used throughout this

dissertation. Thus, the Kohn-Sham orbitals are expanded as,

$$\psi_{n\mathbf{k}}(\mathbf{r}) = \sum_{\mathbf{G}} c_{n\mathbf{k}}(\mathbf{G}) \mathrm{e}^{i(\mathbf{k}+\mathbf{G})\cdot\mathbf{r}}, \tag{2.20}$$

where the coefficients $c_{n\mathbf{k}}(\mathbf{G})$ represents the contributions of the planewaves with index $\mathbf{G}$. The planewaves used in our calculations are truncated with an energy cutoff E_{cut},

$$\frac{\hbar^2}{2m_e} |\mathbf{k}+\mathbf{G}| \leq E_{\mathrm{cut}}. \tag{2.21}$$

The index $\mathbf{k}$ is the point in the Brillouin zone.

In the Kohn-Sham Hamiltonian, the external potential $V_{\mathrm{ext}}(\mathbf{r})$ is the interaction between electrons and nuclei. However, this interaction is singular as an electron gets closer to an ion. To describe such singularity, one would need a huge number of planewaves, and the convergence of the calculations will be very difficult. Considering the fact that chemical properties are dominated by valence electrons, we can express the interaction between core electrons, ions and valence electrons in an effective potential, which is commonly referred to as pseudopotential.[125]

Throughout this dissertation, we use norm-conserving (NC) type pseudopotentials.[58, 57] In general, the NC pseudopotentials contain two parts, the local part and non-local part,

$$V_{\mathrm{NC}}(r, r') = V^l(r) + \sum_{ij} |\beta_i(r)\rangle \, V_{ij}^{nl} \, \langle \beta_j(r') | \,, \tag{2.22}$$

where β is a set of projection basis and V_{ij}^{nl} is the contribution of the projection basis, and r is the norm of the position vector $\mathbf{r}$ to the atom nuclear, $r = |\mathbf{r}|$.

2.3 Many-body perturbation theory

2.3.1 Hedin's equations

In 1965, L. Hedin reformulated the Schrödinger equation in terms of a set of self-consistent equations based on Green's functions, and the method is known as many-body perturbation theory (MBPT) today.[61] The complete set of Hedin's equations reads: (see also Figure 2.1a)

$$G(1,2) = G_0(1,2) + \iint \mathrm{d3d4}\, G_0(1,3)\Sigma(3,4)G(4,2) \tag{2.23a}$$

$$\Gamma(1,2,3) = \delta(1,2)\delta(1,3) + \iint\iint \mathrm{d4d5d6d7}\, \frac{\delta\Sigma(2,3)}{\delta G(5,6)} G(4,5)G(6,7)\Gamma(1,4,7) \tag{2.23b}$$

$$\chi_0(1,2) = -i \iint \mathrm{d3d4}\, G(1,3)G(1,4)\Gamma(2,3,4) \tag{2.23c}$$

$$W(1,2) = v_c(1,2) + \iint \mathrm{d3d4}\, v_c(1,3)\chi_0(3,4)W(4,2) \tag{2.23d}$$

$$\Sigma(1,2) = i \iint \mathrm{d3d}\, 4G(1,4)W(1,3)\Gamma(2,3,4) \tag{2.23e}$$

where the numbers are compact notations of coordinate and time $1 = (\mathbf{r}_1, t_1)$, $2 = (\mathbf{r}_2, t_2)$, etc; G_0 and G are the Green's function of the non-interacting and interacting systems; Σ is the self-energy; Γ is the vertex function; χ_0 is the irreducible polarizibility; v_c and W are the bare and screened Coulomb interactions, respectively. In addition to the equations above, we define the dielectric function

$$\epsilon(1,2) = 1 - \int \mathrm{d3}\, v_c(1,3)\chi_0(3,2) \tag{2.24}$$

and Eq. (2.23d) can be equivalently written in terms of the dielectric function,

$$W(1,2) = \int \mathrm{d3}\, \epsilon^{-1}(1,3)v_c(2,3). \tag{2.25}$$

The exact self-consistent solution of Hedin equation is still not feasible even with today's computing capability. Thus, it is necessary to make approximations to the original Hedin equations to conduct practical calculations for realistic materials, and the most famous one is the GW approximation.[8, 65, 64, 66]

2.3.2 GW approximation

Within the GW approximation, (see Figure 2.1b) the vertex function Γ is neglected and the irreducible polarizibility and self-energy read,

$$\chi_0(1,2) = -iG(1,2)G(1,2) \tag{2.26a}$$

$$\Sigma(1,2) = iG(1,2)W(1,2). \tag{2.26b}$$

The expression Eq. (2.26a) for χ_0 is known as the random phase approximation (RPA)[39] and the expression of self-energy Eq. (2.26b) gives rise to the name GW approximation.

The GW approximation ignores the vertex, but it still requires running self-consistent calculations. The G_0W_0 approximation, where no self-consistent procedure is performed, is widely employed, because it is computationally more affordable (see Figure 2.1c). The subscript 0 in G_0W_0 approximation indicates non-self-consistency.

The discussion above is a general framework of the G_0W_0 approximation, and now we define the numerical methods[143, 144, 51, 52, 147] we use in this dissertation (see Figure 2.1c). As G_0W_0 is a perturbative method, the initial guess of G does make a difference. A common practice is to construct the initial Green's function from DFT wavefunctions ψ_n and DFT energy levels ε_n,

$$G_0(\mathbf{r},\mathbf{r}',\omega) = \sum_n \frac{\psi_n(\mathbf{r})\psi_n^*(\mathbf{r}')}{\omega - \varepsilon_n + i0^+\mathrm{sgn}(\varepsilon_n - \varepsilon_F)}, \tag{2.27}$$

where ε_F is the Fermi level. Then the irreducible polarization χ_0 is approximated with,

$$\chi_0 = -iG_0G_0, \tag{2.28}$$

and it can be written in terms of Kohn-Sham wavefunctions using the Alder-Wiser expression: [145]

$$\begin{aligned}\chi_0(\mathbf{r},\mathbf{r}',\omega) = &\sum_{nm} \psi_n(\mathbf{r})\psi_n^*(\mathbf{r}')\psi_m(\mathbf{r}')\psi_m^*(\mathbf{r})\times \\ &\left[\frac{\theta(\varepsilon_n-\varepsilon_F)\theta(\varepsilon_F-\varepsilon_m)}{\omega-(\varepsilon_n-\varepsilon_m)+i0^+} - \frac{\theta(\varepsilon_F-\varepsilon_n)\theta(\varepsilon_m-\varepsilon_F)}{\omega-(\varepsilon_n-\varepsilon_m)-i0^+}\right]\end{aligned} \tag{2.29}$$

The screened Coulomb interaction is constructed from Eq. (2.23d), and the G_0W_0 self-energy reads:

$$\Sigma(1,2) = iG_0(1,2)W_0(1,2). \tag{2.30}$$

Once we have the self-energy, the G_0W_0 quasiparticle energy is computed perturbatively onto DFT energy levels,

$$\varepsilon_n^{\mathrm{QP}} = \varepsilon_n^{\mathrm{KS}} + \left\langle \psi_n \middle| \Sigma_n(\varepsilon_n^{\mathrm{QP}}) - V_{\mathrm{xc}} \middle| \psi_n \right\rangle \tag{2.31}$$

Unless otherwise indicated, all of the G_0W_0 calculations in this dissertation follows the procedure described above and illustrated in Figure 2.1c.

2.3.3 Low-rank decomposition of the irreducible polarizibility

Within the RPA and using DFT wavefunctions, the irreducible polarizability can be evaluated with Eq. (2.29). However, the summation runs over all unoccupied bands and it is only doable for small systems, but not for large supercells.

Recently, the low-rank decomposition of the irreducible polarizability has been proposed to implement G_0W_0 calculations for large scale systems. [143, 144, 51, 52, 84, 147] The low-rank decomposition expresses the symmetrized polarizability $\tilde{\chi}_0$ in terms of its leading

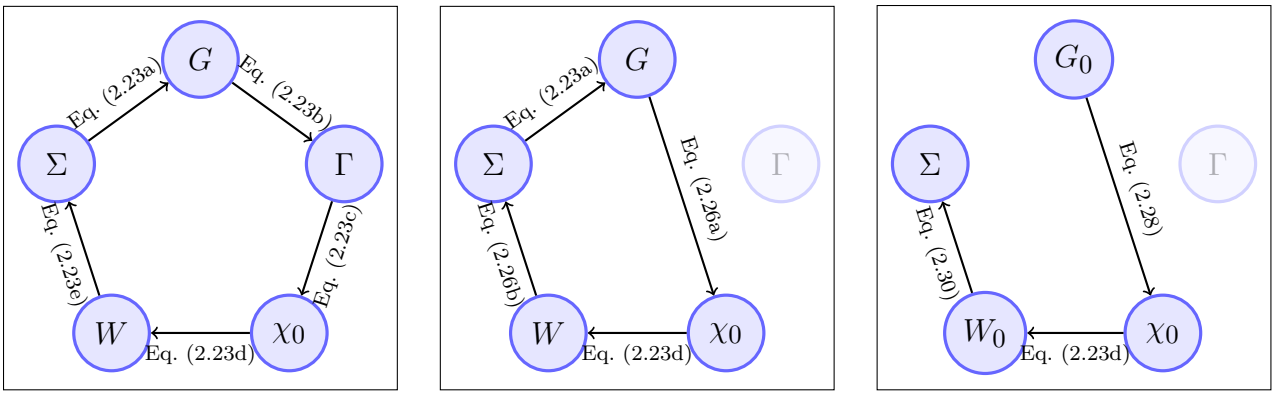

(a) MBPT (b) GW (c) G_0W_0 with RPA

Figure 2.1: Illustration of the quantities involved in the (a) original Hedin's equations, (b) the GW approximation, (c) the G_0W_0 approximation within the random phase approximation (RPA).

eigenvectors ϕ,

$$\tilde{\chi}_0(\mathbf{q}) = \sum_i^{N_{\mathrm{PDEP}}} |\phi_i(\mathbf{q})\rangle \, \lambda_i(\mathbf{q}) \, \langle \phi_i(\mathbf{q})| \,, \tag{2.32}$$

where $\tilde{\chi}_0$ is the symmetrized irreducible polarizability $\tilde{\chi}_0 = v_c^{1/2} \chi_0 v_c^{1/2}$, $\phi_i(\mathbf{q})$ is the eigenvector of $\tilde{\chi}_0$ and λ_i is the corresponding eigenvalue and $\mathbf{q}$ is the difference between $\mathbf{k}$ points in the Brillouin zone. The eigenvectors of $\tilde{\chi}_0$ are known as projective dielectric eigenpotentials (PDEP).

The PDEPs from a general orthonormal basis and can be used to represent Green's functions G and screened Coulomb interactions W, and the G_0W_0 approximation can be implemented within the PDEP basis. For details of the implementation, please refer to Ref. 143, 144, 51.

2.4 Density functional perturbation theory (DFPT)

Phonon modes are the collective vibrations of atoms in solids.[15, 10, 87] Within the harmonic approximation, the phonon modes can be obtained by diagonalizing the dynamical matrix $D_{I\alpha,J\beta}$, whose elements are defined as the derivative of the total energy with respect to

atomic displacements,

$$D_{I\alpha,J\beta} = \frac{1}{\sqrt{M_I M_J}} C_{I\alpha,J\beta} = \frac{1}{\sqrt{M_I M_J}} \frac{\partial^2 E_{\text{tot}}}{\partial u_{I\alpha} \partial u_{J\beta}}, \tag{2.33}$$

where $C_{I\alpha,J\beta}$ is known as the force constant matrix, I and J are indices of atoms, α and β are the three directions to displace atoms, u is the coordinate of the atom, M are atomic masses, and E_{tot} is the total energy of the system.

Eq. (2.33) can be evaluated by a finite difference method, known as the frozen-phonon (FPH) approach.[30] This approach is straightforward to implement, but in general it requires large supercells for semiconductors to converge.

An alternative method is the density functional perturbation theory (DFPT), which has been widely used. We briefly explain the method below, and throughout this dissertation, we use the short-hand notations ∂ to represent a generic change of densities $\partial n(\mathbf{r})$, wavefunctions $\partial\psi(\mathbf{r})$ or potentials $\partial V(\mathbf{r})$, and $\partial_{I\alpha}$ to represent the changes due to the displacements of I-th atom along direction α.

When the external potential V_{ext} in the Kohn-Sham Hamiltonian is varied, the Kohn-Sham wavefunctions ψ, electron densities $n(\mathbf{r})$ and the potentials V_{H} and V_{xc} will change accordingly. The central idea of DFPT is to adjust the potentials, wavefunctions, and densities self-consistently according to the perturbation until convergence is achieved. The key steps are:

1. Solve for the change of DFT wavefunctions $\partial\psi(\mathbf{r})$ with the change of external potential V_{ext} as the initial perturbation.

2. Construct the change of density $\partial n(\mathbf{r})$ from the change of wavefunctions.

3. Update the change of Hartree potential ∂V_{H} and exchange-correlation potential ∂V_{xc}.

4. Repeat the calculations until convergence is achieved.

In DFPT, a $\mathbf{k}$-point sampling of the Brillouin zone is used for wavefunctions, and phonons are computed at each $\mathbf{q}$-point, where the $\mathbf{q}$ point is defined as the differences between $\mathbf{k}$ points and is associated with the wavelength of the phonon mode. For each $\mathbf{q}$ point, we rewrite the definition of force constants as:

$$C_{I\alpha,J\beta}(\mathbf{q}) = \frac{\partial^2 E_{\text{tot}}}{\partial u^*_{I\alpha\mathbf{q}} \partial u_{J\beta\mathbf{q}}}. \tag{2.34}$$

The connection between Eq. (2.33) and Eq. (2.34) can be found in Appendix A.

The most difficult component of force constants is the so-called electronic contribution,[10]

$$C^{\text{el}}_{I\alpha,J\beta}(\mathbf{q}) \propto \left\langle \partial_{I\alpha\mathbf{q}} \psi_{n\mathbf{k}} \left| \partial_{J\beta\mathbf{q}} V_{\text{ext}} \right| \psi_{n\mathbf{k}} \right\rangle, \tag{2.35}$$

where $\partial\psi_{n\mathbf{k}}$ is the change of wavefunctions due to the displacements of atomic positions. Other parts of the force constants are trivial to compute and they are discussed in Appendix A.

Given a change of scf potential ∂V_{scf}, the change of wavefunction can be obtained by solving Sternheimer's equation[132],

$$(H^{\text{KS}}_{\mathbf{k}+\mathbf{q}} - \varepsilon_{n\mathbf{k}}) \left| \partial_{I\alpha\mathbf{q}} \psi_{n\mathbf{k}} \right\rangle = -\mathcal{P}^c_{\mathbf{k}+\mathbf{q}} \partial_{I\alpha\mathbf{q}} V_{\text{scf}} \left| \psi_{n\mathbf{k}} \right\rangle, \tag{2.36}$$

where $\mathcal{P}^c_{\mathbf{k}+\mathbf{q}} = \sum_c \left| \psi_{c\mathbf{k}+\mathbf{q}} \right\rangle \left\langle \psi_{c\mathbf{k}+\mathbf{q}} \right|$ is the projector operator on to the conduction bands manifold and c is the index of conduction band. $\tilde{H}_{\mathbf{k}+\mathbf{q}}$ is the Hamiltonian projected to the conduction band manifold, $H^{\text{KS}}_{\mathbf{k}+\mathbf{q}} = \mathcal{P}^c_{\mathbf{k}+\mathbf{q}} H^{\text{KS}} \mathcal{P}^c_{\mathbf{k}+\mathbf{q}}$. The detailed derivation of the Sternheimer equation can be found in Appendix A.

Only the change of external potential ∂V_{ext} is known from phonon calculations. Thus, a self-consistent strategy is usually employed to update V_{scf} until the change of density is converged and this is implemented in the `PHonon` package of the `Quantum Espresso`

software.[41]. In Chapter 4, we developed a protocol to run phonon calculations without running self-consistent calculations.

During the iterations of DFPT, the potentials are updated using the change of density

$$\partial_{\mathbf{q}} V_{\mathrm{Hxc}} = \partial_{\mathbf{q}} V_{\mathrm{H}} + \partial_{\mathbf{q}} V_{\mathrm{xc}} = (v_c + f_{\mathrm{xc}}) \partial_{\mathbf{q}} n(\mathbf{r}), \tag{2.37}$$

where f_{xc} is the exchange-correlation kernel defined as the functional derivative of the exchange-correlation potential,

$$f_{\mathrm{xc}}(\mathbf{r}, \mathbf{r}') = \frac{\delta V_{\mathrm{xc}}(\mathbf{r})}{\delta n(\mathbf{r}')}, \tag{2.38}$$

and it is simple to compute for a given LDA/GGA functionals, but not for hybrid functionals. In Chapter 5, we implement an approach to compute phonons at the hybrid functional level of theory.

The change of density is constructed from the change of wavefunctions,

$$\partial_{\mathbf{q}} n(\mathbf{r}) = 2 \sum_{n}^{\mathrm{occ}} \sum_{\mathbf{k}} \left[\partial_{\mathbf{q}} \psi^*_{n\mathbf{k}}(\mathbf{r}) \psi_{n\mathbf{k}}(\mathbf{r}) + c.c. \right] \tag{2.39}$$

where the summation runs over all occupied bands at every $\mathbf{k}$ point and the prefactor 2 accounts for spin.

Once the we have the force constants and dynamical matrices are obtained, the phonon frequencies can be computed by diagonalizing the dynamical matrix:

$$\sum_{J\beta} D_{I\alpha, J\beta}(\mathbf{q}) \xi_{J\beta, \mathbf{q}\nu} = \omega^2_{\mathbf{q}\nu} \xi_{I\alpha, \mathbf{q}\nu}, \tag{2.40}$$

where $\omega_{\mathbf{q}\nu}$ is the phonon frequency of mode ν at $\mathbf{q}$ point, and $\xi_{\mathbf{q}\nu}$ is the polarization of the phonon mode.

Another useful result of a DFPT calculation is the converged change of potential $\partial V_{\mathrm{scf}}$, which will be used in electron-phonon calculations.

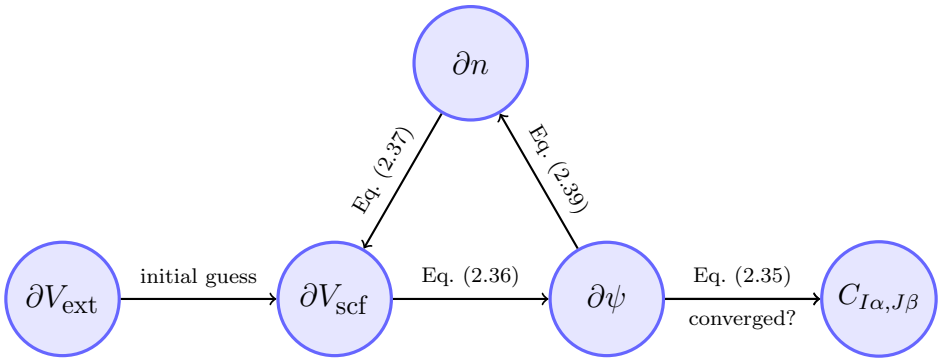

Figure 2.2: The procedure to compute phonons based on density functional perturbation theory (DFPT). DFPT uses the change of external potential ∂V_{ext} due to nuclear displacements as initial perturbation, and solves for the change of the self-consistent (scf) potential ∂V_{scf}, change of wavefunctions $\partial\psi$, and change of density ∂n self-consistently until converge of these three quantities is achieved.

2.5 Electron-phonon interaction from DFPT

To compute electron-phonon interaction, we write the first-order electron-phonon coupling Hamiltonian in second quantization,

$$H^{\text{ep}} = \sum_{mn\nu\mathbf{kq}} g_{mn\nu}(\mathbf{k},\mathbf{q})\hat{c}^{\dagger}_{m\mathbf{k}+\mathbf{q}}\hat{c}_{n\mathbf{k}}(\hat{b}_{\mathbf{q}\nu} + \hat{b}^{\dagger}_{-\mathbf{q}\nu}), \tag{2.41}$$

where $\hat{c}^{\dagger}$ and $\hat{c}$ are creation and annihilation operators of electrons, $\hat{b}^{\dagger}$ and $\hat{b}$ are creation and annihilation operators of phonons associated to phonon mode ν and momentum $\mathbf{q}$. The central quantity is the electron-phonon coupling matrices $g_{mn\nu}(\mathbf{k},\mathbf{q})$, see Figure 2.3.

Early studies relied on model coupling matrices, e.g., the Fröhlich model,[36], but now we can compute the electron-phonon coupling matrices from first-principles with DFPT. Within DFPT, the electron-phonon coupling matrix can be evaluated with the change of scf potential,

$$g_{mn\nu}(\mathbf{k},\mathbf{q}) = \left\langle \psi_{m\mathbf{k}+\mathbf{q}} \left| \partial_{\mathbf{q}\nu} V_{\text{scf}} \right| \psi_{n\mathbf{k}} \right\rangle, \tag{2.42}$$

or alternatively in the basis of atomic perturbations, $g_{mnI\alpha}(\mathbf{k},\mathbf{q})$.

$$g_{mnI\alpha}(\mathbf{k},\mathbf{q}) = \left\langle \psi_{m\mathbf{k}+\mathbf{q}} \left| \partial_{I\alpha\mathbf{q}} V_{\mathrm{scf}} \right| \psi_{n\mathbf{k}} \right\rangle . \tag{2.43}$$

These two forms are equivalent and can be easily related:

$$g_{mn\nu}(\mathbf{k},\mathbf{q}) = \sum_{I\alpha} \frac{\xi_{I\alpha,\mathbf{q}\nu}}{\sqrt{2M_I\omega_{\mathbf{q}\nu}}} g_{mnI\alpha}(\mathbf{k},\mathbf{q}). \tag{2.44}$$

The electron-phonon self-energy is the energy of an electron with the electron-phonon interactions included. It has two parts, the Fan-Migdal (FM) part,

$$\Sigma^{\mathrm{FM}}_{n\mathbf{k}}(\omega,T) = \sum_{m\nu\mathbf{q}} |g_{mn\nu}(\mathbf{k},\mathbf{q})|^2 \left[\frac{n_{\mathbf{q}\nu} + f_{m\mathbf{k}+\mathbf{q}}}{\omega - \varepsilon_{m\mathbf{k}+\mathbf{q}} + \omega_{\mathbf{q}\nu} - i0^+} + \frac{n_{\mathbf{q}\nu} + 1 - f_{m\mathbf{k}+\mathbf{q}}}{\omega - \varepsilon_{m\mathbf{k}+\mathbf{q}} - \omega_{\mathbf{q}\nu} - i0^+} \right] \tag{2.45}$$

and Debye-Waller part,

$$\begin{aligned} \Sigma^{\mathrm{DW}}_{n\mathbf{k}}(T) = -\sum_{m\nu\mathbf{q}} \sum_{I\alpha J\beta} \frac{2n_{\mathbf{q}\nu}+1}{\varepsilon_{n\mathbf{k}} - \varepsilon_{m\mathbf{k}}} \frac{1}{4\omega_{\mathbf{q}\nu}} \left[\frac{\xi_{I\alpha,\mathbf{q}\nu}\xi^*_{I\beta,\mathbf{q}\nu}}{M_I} + \frac{\xi_{J\alpha,\mathbf{q}\nu}\xi^*_{J\beta,\mathbf{q}\nu}}{M_J} \right] \times \\ g^*_{mnI\alpha}(\mathbf{k},\mathbf{0}) g_{mnJ\beta}(\mathbf{k},\mathbf{0}), \end{aligned} \tag{2.46}$$

where T is the temperature.

It is worth noting that the Debye-Waller self-energy is in fact due to second-order electron-phonon interaction, but the second-order electron-phonon coupling matrices $g_{mn\nu\nu'}(\mathbf{k},\mathbf{q},\mathbf{q}')$ are commonly approximated with first-order electron-phonon coupling matrices $g_{mn\nu}(\mathbf{k},\mathbf{q})$. The technique is known as rigid-ion approximation (RIA) [4, 109, 49], and it has already been used in the DW self-energy written above.

Using the frequency-dependent Fan-Migdal self-energy, the renormalized energy levels

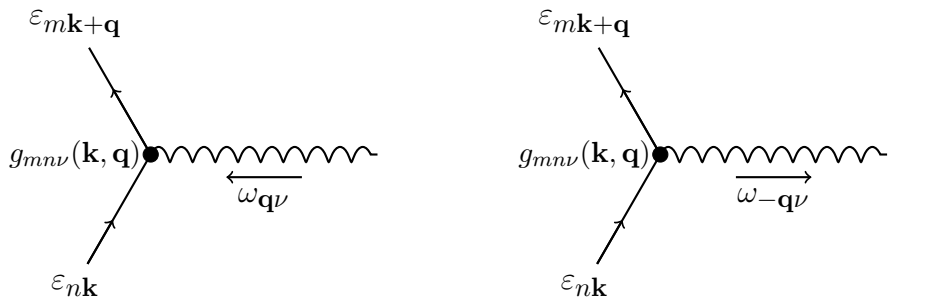

(a) $g_{mn\nu}(\mathbf{k},\mathbf{q})\hat{c}^{\dagger}_{m\mathbf{k}+\mathbf{q}}\hat{c}_{n\mathbf{k}}\hat{b}_{\mathbf{q}\nu}$ (b) $g_{mn\nu}(\mathbf{k},\mathbf{q})\hat{c}^{\dagger}_{m\mathbf{k}+\mathbf{q}}\hat{c}_{n\mathbf{k}}\hat{b}^{\dagger}_{-\mathbf{q}\nu}$

Figure 2.3: Illustration of two electron-phonon processes in the electron-phonon interacting Hamiltonian of Eq. (2.41).

can be computed self-consistently,

$$\omega = \varepsilon_{n\mathbf{k}} + \left\langle \psi_{n\mathbf{k}} \middle| \Sigma^{FM}_{n\mathbf{k}}(\omega, T) + \Sigma^{DW}_{n\mathbf{k}}(T) \middle| \psi_{n\mathbf{k}} \right\rangle, \tag{2.47}$$

with initial guess $\omega_0 = \varepsilon_{n\mathbf{k}}$. But the frequency-dependence makes calculations difficult, and thus the Allen-Heine-Cardona (AHC) formalism has been widely adopted. In the AHC formalism, two approximations are used to simplify the calculations of the Fan-Migdal self-energy,

1. The On-the-Mass-Shell (OMS) approximation neglects the frequency-dependence of the Fan-Migdal self-energy and approximates it with the self-energy evaluated at $\omega = \varepsilon_{n\mathbf{k}}$: $\Sigma^{\mathrm{FM}}_{n\mathbf{k}}(\omega) = \Sigma^{\mathrm{FM}}_{n\mathbf{k}}(\varepsilon_{n\mathbf{k}})$. It assumes that the FM self-energy is the same at all frequencies.

2. The adiabatic approximation[1] neglects the phonon frequencies in the denominator of the FM self-energy assuming that $\varepsilon_{n\mathbf{k}} - \varepsilon_{m\mathbf{k}+\mathbf{q}}$ is much larger than phonon frequency $\omega_{\mathbf{q}\nu}$.

1. The adiabatic approximation mentioned here is not related to the Born-Oppenheimer approximation, which is often also referred to as adiabatic approximation.

Table 2.1: A list of theoretical approximations used to compute the Fan-Migdal self-energy, where we specify whether the on-the-mass-shell (OMS) and the adiabatic approximations are applied (✓) or not (×) applied.

Level of theory	OMS	Adiabatic	Equation
AHC	✓	✓	(2.48)
Non-adiabatic AHC	✓	×	(2.50)
FF-AD	×	✓	(2.49)
FF-NA	×	×	(2.45)

Within the AHC formalism, the Fan-Migdal self-energy is simplified to,

$$\Sigma^{FM}_{n\mathbf{k}}(T) \simeq \sum_{m\nu\mathbf{q}} |g_{mn\nu}(\mathbf{k},\mathbf{q})|^2 \frac{2n_{\mathbf{q}\nu}+1}{\varepsilon_{n\mathbf{k}} - \varepsilon_{m\mathbf{k}+\mathbf{q}}}. \tag{2.48}$$

Despite its success, the AHC formalism fails to include non-adiabaticity and the frequency dependence, thus in thie dissertation we will go beyond the AHC formalism. When the frequency-dependence is restored and the adiabatic appoximation is still applied, we refer to the self-energy as full frequency-dependent adiabatic (FF-AD) FM self-energy:

$$\Sigma^{FM}_{n\mathbf{k}}(\omega, T) \simeq \sum_{m\nu\mathbf{q}} |g_{mn\nu}(\mathbf{k},\mathbf{q})|^2 \frac{2n_{\mathbf{q}\nu}+1}{\omega - \varepsilon_{m\mathbf{k}+\mathbf{q}}}. \tag{2.49}$$

If we restore the phonon frequencies in the denominator of the FM self-energy but still keep the OMS approximation,

$$\Sigma^{\mathrm{FM}}_{n\mathbf{k}}(T) = \sum_{m\nu\mathbf{q}} |g_{mn\nu}(\mathbf{k},\mathbf{q})|^2 \left[\frac{n_{\mathbf{q}\nu} + f_{m\mathbf{k}+\mathbf{q}}}{\varepsilon_{n\mathbf{k}} - \varepsilon_{m\mathbf{k}+\mathbf{q}} + \omega_{\mathbf{q}\nu} - i0^+} + \frac{n_{\mathbf{q}\nu} + 1 - f_{m\mathbf{k}+\mathbf{q}}}{\varepsilon_{n\mathbf{k}} - \varepsilon_{m\mathbf{k}+\mathbf{q}} - \omega_{\mathbf{q}\nu} - i0^+} \right], \tag{2.50}$$

we have the so-called non-adiabatic AHC. Thus, the original FM self-energy in Eq. (2.45) is full frequency-dependent and non-adiabatic (FF-NA). We summarized the levels of approximations applied to the FM self-energy in Table 2.1.

Table 2.2: A comparison of the approximations used in density functional perturbation theory (DFPT), frozen-phonon (FPH) and path-integral molecular dynamics (PIMD) methods. The symbols (✓) and (×) are used to indicated whether the approximations are applied or not, respectively.

Method	Rigid-ion	Anharmonic
DFPT	✓	×
FPH	×	×
PIMD	×	✓

2.6 Electron-phonon interaction from non-perturbative methods

In addition to the DFPT, the frozen-phonon approach (FPH), first-principles molecular dynamics (FPMD) and path-integral molecular dynamics (PIMD) are also used to compute electron-phonon interactions. In this dissertation, these methods are often employed to generate reference results to verify our findings.

For the FPH approach, one computes the change of energy levels due to phonon vibrations $\partial\varepsilon_n/\partial n_\nu$ using finite differences, where ε_n is the n-th Kohn-Sham energy level and n_ν is the phonon occupation number of ν-th mode, and one evaluates the change of energy levels as

$$\partial\varepsilon_n(T) = \sum_\nu \frac{\partial\varepsilon_n}{\partial n_\nu}\left[n_\nu(T) + \frac{1}{2}\right]. \tag{2.51}$$

The derivative $\partial\varepsilon_n/\partial n_\nu$ is called the electron-phonon coupling energy (EPCE)[6, 109], and it is equivalent to the expression in the AHC formalism, except that the rigid-ion approximation is not needed in the FPH approach.

The DFPT and FPH methods rely on the harmonic approximation. We note that the PIMD incorporates anharmonic effects, and thus it can be used to compute electron-phonon interactions for disordered systems, for example amorphous diamond.[72]

We summarize the differences among the DFPT, FPH and PIMD methods in Table 2.2. In Chapter 4 and Chapter 5, we compare our DFPT results with literature results and our own FPH and PIMD results.

2.7 Density matrix perturbation theory (DMPT)

Density matrix perturbation theory (DMPT) was implemented to compute excitation and absorption spectra using time-dependent density functional theory (TDDFT)[115, 117] and the Bethe-Salpeter equation (BSE).[118, 119, 116, 99] Unlike the Casida equation,[135, 25, 100] DMPT does not require the summation over empty bands and it is very useful to conduct calculations of large systems.

While the Schrödinger equation describes the evolution of wavefunctions, the Liouville-von Neumann equation governs the evolution of density matrices,

$$i\frac{\mathrm{d}\gamma}{\mathrm{d}t} = [H, \gamma], \tag{2.52}$$

where γ is the density matrix $\gamma(\mathbf{r}, \mathbf{r'}, t) = \sum_n^{\mathrm{occ}} \psi_n(\mathbf{r}, t)\psi_n^*(\mathbf{r'}, t)$, here we omit k points and spins for simplicity.

When a system is perturbed, the change of the density matrix obeys the following the equation,

$$i\frac{\mathrm{d}}{\mathrm{d}t}\partial\gamma(t) = \mathcal{L} \cdot \partial\gamma(t) + [\partial V_{\mathrm{ext}}, \gamma], \tag{2.53}$$

where $\mathcal{L}$ is the Liouville superoperator and $\partial\gamma$ it the change of density matrix.[115, 117].

By solving Eq. (2.53), we will obtain the change of wavefunctions due to the displacements of atomic positions like we did for DFPT method. In Chapter 5, we employ the DMPT and solve the Liouville equation for atomic displacements to compute phonons and electron-phonon self-energies. This approach allows one to compute phonons at the hybrid functional level of theory and can be seen as a generalization of the Sternheimer equation.

CHAPTER 3

IMPROVING THE EFFICIENCY OF G_0W_0 CALCULATIONS WITH APPROXIMATE SPECTRAL DECOMPOSITIONS OF DIELECTRIC MATRICES

As briefly introduced in Section 2.3, many-body perturbation theory (MBPT) is a method that computes accurate electronic structure of semiconductors and insulators. Due to the computational cost of MBPT, the G_0W_0 approximation is the practical method to implement MBPT. In this chapter, we developed an approximate basis of dielectric function to speed up G_0W_0 calculations. This chapter is reproduced from Han Yang, Marco Govoni, and Giulia Galli. *Improving the efficiency of G_0W_0 calculations with approximate spectral decompositions of dielectric matrices* The Journal of Chemical Physics 151 (22), 224102, with the permission of AIP Publishing. https://doi.org/10.1063/1.5126214

3.1 Introduction

Devising accurate and efficient methods to predict the electronic properties of molecules and condensed systems is an active field of research. Density functional theory (DFT) has been widely used for electronic structure calculations.[63, 71, 90] However, the exact form of the exchange-correlation functional is unknown and therefore DFT results depend on the choice of approximate functionals. Improvement over DFT results may be obtained by using many-body perturbation theory (MBPT).[100, 91] A practical formulation of MBPT for many electron systems was proposed by Hedin,[61] where the self-energy Σ is written in terms of the Green's function G and the screened Coulomb interaction W.

The GW approximation[61, 91] has been successful in the description of the electronic properties of several classes of materials and molecules;[142, 86, 52, 122, 18, 47] however the computational cost of GW calculations remains rather demanding and many complex

systems cannot yet be studied using MBPT. Hence, algorithmic improvements are required to apply MBPT to realistic systems. One of the most demanding steps of the original implementation of GW calculations[65, 64, 66, 133, 134] involves an explicit summation over a large number of unoccupied single particle electronic orbitals, which enter the evaluation of the dielectric matrix ϵ[2, 145] defining the screened Coulomb interaction W ($W = \epsilon^{-1} v_c$, where v_c is the Coulomb interaction). The summation usually converges slowly as a function of the number of virtual orbitals (N_c). In recent years, several approaches have been proposed to improve the efficiency of GW calculations. For example, in Ref. 121 it was suggested to replace unoccupied orbitals with approximate physical orbitals (SAPOs); the author of Ref. 19 simply truncated the sum over empty states entering the calculation of the irreducible density-density response function, and assigned the same, average energy to all the empty states higher than a preset value; in a similar fashion, in Ref. 38 an integration over the density of empty states higher than a preset value was used. Other approaches adopted sophisticated algorithms to invert the dielectric matrix, e.g., in Ref. 131, they employed a Lanczos algorithm.

Recently, an implementation of G_0W_0 calculations avoiding altogether explicit summations over unoccupied orbitals, as well as the necessity to invert dielectric matrices, has been proposed,[143, 144, 98, 107, 51] based on the spectral decomposition of density-density response functions in terms of eigenvectors (also known as projective dielectric eigenpotentials, PDEPs). In spite of the efficiency improvement introduced by such formulation, G_0W_0 calculations for large systems remain computationally demanding.

In this chapter, we propose an approximation to the projective dielectric technique,[143] which in many cases leads to computational savings of G_0W_0 calculations of 10-50%, without compromising accuracy. The rest of the chapter is organized as follows: we describe the proposed methodology in Section 3.2 and then we present results for several systems in Section 3.3, followed by our conclusions.

3.2 Methodology

We compute the density-density response function of solids and molecules within the framework of the random phase approximation (RPA), using projective dielectric eigenpotentials (PDEP)[143, 144, 51]. The accuracy of this approach has been extensively tested for molecules and solids.[144] The technique relies on the solution of the Sternheimer's equation [132]

$$(\hat{H} - \varepsilon_v \hat{I})|\Delta\psi_v\rangle = -\hat{P}_c \Delta\hat{V}|\psi_v\rangle \tag{3.1}$$

to obtain the linear variation of the v-th occupied electronic orbital, $|\Delta\psi_v\rangle$, induced by the external perturbation $\Delta\hat{V}$. In Equation 3.1, $\hat{I}$ is the identity operator, $\hat{P}_c$ is the projector onto the unoccupied states, ε_v and ψ_v are the v-th eigenvalue and eigenvector of the unperturbed Kohn-Sham Hamiltonian $\hat{H} = \hat{K} + \hat{V}_{\text{SCF}}$, respectively, where $\hat{K} = -\frac{\nabla^2}{2}$ is the kinetic energy, $\hat{V}_{\text{SCF}}$ is the self-consistent potential. For each perturbation, the first order response of the density Δn can be obtained as [10]

$$\Delta n = 2 \sum_v \psi_v \Delta\psi_v + c.c. \tag{3.2}$$

Equation 3.1 and (3.2) can be used to iteratively diagonalize the static symmetrized *irreducible* density-density response, $\tilde{\chi}_0$:[143, 144, 51]

$$\tilde{\chi}_0 = \sum_{i=1}^{N_{\text{PDEP}}} |\xi_i\rangle \, \lambda_i \, \langle \xi_i| \,, \tag{3.3}$$

where λ_i and ξ_i are eigenvalues and eigenvectors of $\tilde{\chi}_0$ and N_{PDEP} is the number of eigenvectors of $\tilde{\chi}_0$, respectively. The eigenvectors ξ_i are called PDEPs: projective dielectric eigenpotentials throughout the manuscript. The symmetrized irreducible density-density response function is defined as $\tilde{\chi}_0 = v_c^{1/2} \chi_0 v_c^{1/2}$, where v_c is the Coulomb potential.[51] Within the RPA, the symmetrized *reducible* density-density response can be expressed as

$\tilde{\chi} = (1 - \tilde{\chi}_0)^{-1} \tilde{\chi}_0$, therefore the ξ_i are also eigenvectors of $\tilde{\chi}$. The projective dielectric technique has also been recently applied beyond the RPA using a finite field method.[84]

When solving the Sternheimer equation, it is not necessary to compute explicitly the electronic empty states, because one can write $\hat{P}_c = \hat{I} - \hat{P}_v$, since the eigenvectors of $\hat{H}$ form a complete basis set ($\hat{P}_v$ is the projector onto the occupied states). The use of Eq. (3.3) significantly reduces the cost of G_0W_0 calculation from $N_{\mathrm{pw}}^2 N_v N_c$ to $N_{\mathrm{PDEP}} N_{\mathrm{pw}} N_v^2$ where N_v, N_c, N_{PDEP}, N_{pw} are numbers of occupied orbitals (valence bands in solids), virtual orbitals (conduction bands in solids), PDEPs, and plane waves, respectively. Importantly $N_{\mathrm{PDEP}} \ll N_{\mathrm{pw}}$.

The application of the algorithm described above to large systems is hindered by the cost of solving Eq. (3.1). However, we note that the eigenvalues of $\tilde{\chi}_0$ rapidly converge to zero,[82, 143, 144, 52] (an example is shown in Figure 3.1). In addition, as shown in Ref. 144, the eigenvalue spectrum of the dielectric function for eigenvectors higher than the first few, is similar to that of the Lindhard function.[79] Hence we propose to compute the PDEPs of $\tilde{\chi}_0$ corresponding to the lowest eigenvalues using Equation 3.1 and (3.2) and to compute the remaining ones with a less costly approach. Inspired by the work of Ref. 116, we approximate the eigenpotentials corresponding to higher eigenvalues with kinetic eigenpotentials, which are obtained approximating the full Hamiltonian entering Equation 3.1 with the kinetic operator($\hat{K}$):[83, 116]

$$(\hat{K} - \varepsilon_v \hat{I})|\Delta\psi_v\rangle = -\hat{P}_c \Delta\hat{V}|\psi_v\rangle. \tag{3.4}$$

In the following, we refer to the eigenpotentials from Equation 3.1 as standard PDEPs (stdPDEP, $\xi_i,\ i = 1, \cdots, N_{\mathrm{stdPDEP}}$) and those from Equation 3.4 as kinetic PDEPs (kin-PDEP, $\eta_i,\ i = 1, \cdots, N_{\mathrm{kinPDEP}}$) and we rewrite the irreducible density-density response function as

$$\tilde{\chi}_0 = \sum_{i=1}^{N_{\mathrm{stdPDEP}}} |\xi_i\rangle \lambda_i \langle\xi_i| + \sum_{j=1}^{N_{\mathrm{kinPDEP}}} |\eta_j\rangle \mu_j \langle\eta_j|, \tag{3.5}$$

where ξ_i and η_j are standard and kinetic PDEPs, respectively, and λ_i and μ_j are their corresponding eigenvalues. The procedure to generate stdPDEPs and kinPDEPs is summarized in Figure 3.2. We note that during the construction of kinetic PDEPs, the projection operator $\hat{P} = \hat{I} - \sum_{N_{\mathrm{stdPDEP}}} |\xi_i\rangle \langle\xi_i|$ was applied so as to satisfy the orthonormality constrain, $\langle\xi_i|\xi_j\rangle = \delta_{ij}$, $\langle\eta_i|\eta_j\rangle = \delta_{ij}$ and $\langle\xi_i|\eta_j\rangle = 0$, $\forall(i,j)$; in addition we applied $v_c^{1/2}$ to perturbations to yield a *symmetrized* irreducible response function $\tilde{\chi}_0$.

In our G_0W_0 calculations, both the static Green's function and the statically screened Coulomb interaction are written in the basis of eigenpotentials of the dielectric matrix. Frequency integration is performed using a contour deformation algorithm. A detailed description of the implementation of G_0W_0 calculations in the basis of eigenpotentials can be found in Ref. 98, 107, 51.

3.3 Validation and results

We now turn to discussing results for molecules and solids obtained by using a combination of standard and kinetic PDEPs. To examine the efficiency and applicability of the approximation proposed in Section 3.2, we performed G_0W_0 calculations for a set of closed-shell small molecules, a larger molecule (Buckminsterfullerene C_{60}), and an amorphous silicon nitride/silicon interface (Si_3N_4/Si) with a total of 1152 valence electrons. All Kohn-Sham eigenvalues and eigenvectors were obtained with the QuantumEspresso package,[41, 40] using the PBE approximation[103], SG15[123] ONCV[57] pseudopotentials and G_0W_0 calculations were carried out with the WEST code.[51]

We first considered a subset of molecules taken from the G2/97 test set[29] and calculated their vertical ionization potential (VIP) and electron affinity (EA) using different numbers

of stdPDEPs (N_{stdPDEP}) and kinPDEPs (N_{kinPDEP}). We chose a plane wave cutoff of 85 Ry and a periodic box of edge 30 Bohr. For all molecules, we included either 20 or 100 stdPDEPs in our calculations, then added 100, 200, 300, 400 kinPDEPs in subsequent calculations, after which an extrapolation was performed ($a + \frac{b}{N_{\mathrm{stdPDEP}}+N_{\mathrm{kinPDEP}}}$) to find converged values (one example is shown in Figure 3.3). These results are given in the second (A) and third columns (B) of Table 3.1 and Table 3.2. The reference results reported in the last column (C) of the two tables were obtained with 200, 300, 400, 500 stdPDEPs and an extrapolation was applied. We found that including only 20 stdPDEPs yields quasiparticle energies accurate within 0.1 eV relative to the reference G_0W_0 values obtained using only standard eigenpotentials. The two data sets starting from 20 or 100 stdPDEPs enabled us to save 40% and 10% of computer time compared to the time usage needed with only standard eigenpotentials.

As a representative example, we present the computed eigenvalues of symmetrized irreducible density-density response function of CH_4 molecule in Figure 3.4, and the calculated vertical ionization with different number of eigenpotentials in Figure 3.5 In Figure 3.4, we compare the eigenvalues for the symmetrized irreducible density-density response function of the methane molecule: 500 stdPDEPs and 100 stdPDEPs + 400 kinPDEPs. On the scale of the figure the results are indistinguishable. In Figure 3.5, we show the results for the vertical ionization potential of the CH_4 molecule computed with 5, 10, 20 standard PDEPs (N_{stdPDEP}), and the remaining 100, 200, 300 and 400 PDEPs treated as kinetic PDEPs. When setting $N_{\mathrm{stdPDEP}} = 10$ or 20 we obtain results accurate within 0.02 eV, as compared to the ones obtained using only standard PDEP. When using 5 stdPDEPs we obtain instead an error more than 10 times larger (0.25 eV).

Table 3.3 shows our results for the C_{60} molecule. The structure of C_{60} (point group I_h) was also taken from the NIST computational chemistry database,[67] (optimized with the ωB97X-D functional and cc-pVTZ basis sets) and no further optimization was carried out.

Table 3.1: Vertical ionization potential (eV) obtained at the G_0W_0@PBE level of theory with different numbers of standard and kinetic PDEPs. (A) 20 stdPDEPs + up to 400 kinPDEPs and extrapolated; (B) 100 stdPDEPs + up to 400 kinPDEPs and extrapolated; (C) pure stdPDEPs and extrapolated. A detailed discussion of extrapolations of quasiparticle energies can be found in Ref. 52.

Molecule	A	B	C
C_2H_2	11.07	11.06	11.06
C_2H_4	10.41	10.40	10.40
C_4H_4S	8.80	8.77	8.76
C_6H_6	9.17	9.14	9.13
CH_3Cl	11.28	11.26	11.25
CH_3OH	10.58	10.56	10.56
CH_3SH	9.39	9.36	9.36
CH_4	14.01	14.01	14.01
Cl_2	11.51	11.51	11.50
ClF	12.55	12.55	12.54
CO	13.51	13.50	13.50
CO_2	13.32	13.31	13.31
CS	11.00	10.98	10.98
F_2	14.99	14.97	14.97
H_2CO	10.43	10.42	10.42
H_2O	11.82	11.82	11.81
H_2O_2	10.87	10.87	10.86
HCl	12.50	12.50	12.50
HCN	13.20	13.20	13.20
Na_2	4.95	4.95	4.95

Table 3.2: Vertical electron affinity (eV) obtained at the G_0W_0@PBE level of theory with different numbers of standard and kinetic PDEPs. (A) 20 stdPDEPs + up to 400 kinPDEPs and extrapolated; (B) 100 stdPDEPs + up to 400 kinPDEPs and extrapolated; (C) pure stdPDEPs and extrapolated. A detailed discussion of extrapolations of quasiparticle energies can be found in Ref. 52.

Molecule	A	B	C
C_2H_2	-2.42	-2.41	-2.41
C_2H_4	-1.75	-1.75	-1.75
C_4H_4S	-0.85	-0.81	-0.80
C_6H_6	-1.01	-0.96	-0.96
CH_3Cl	-1.17	-1.16	-1.16
CH_3OH	-0.89	-0.89	-0.89
CH_3SH	-0.88	-0.88	-0.88
CH_4	-0.64	-0.64	-0.64
Cl_2	1.65	1.64	1.65
ClF	1.28	1.28	1.28
CO	-1.56	-1.57	-1.57
CO_2	-0.97	-0.97	-0.97
CS	0.49	0.51	0.51
F_2	1.16	1.16	1.16
H_2CO	-0.69	-0.68	-0.68
H_2O	-0.90	-0.90	-0.90
H_2O_2	-1.80	-1.79	-1.79
HCl	-1.07	-1.07	-1.07
HCN	-2.08	-2.08	-2.08
Na_2	0.64	0.63	0.63

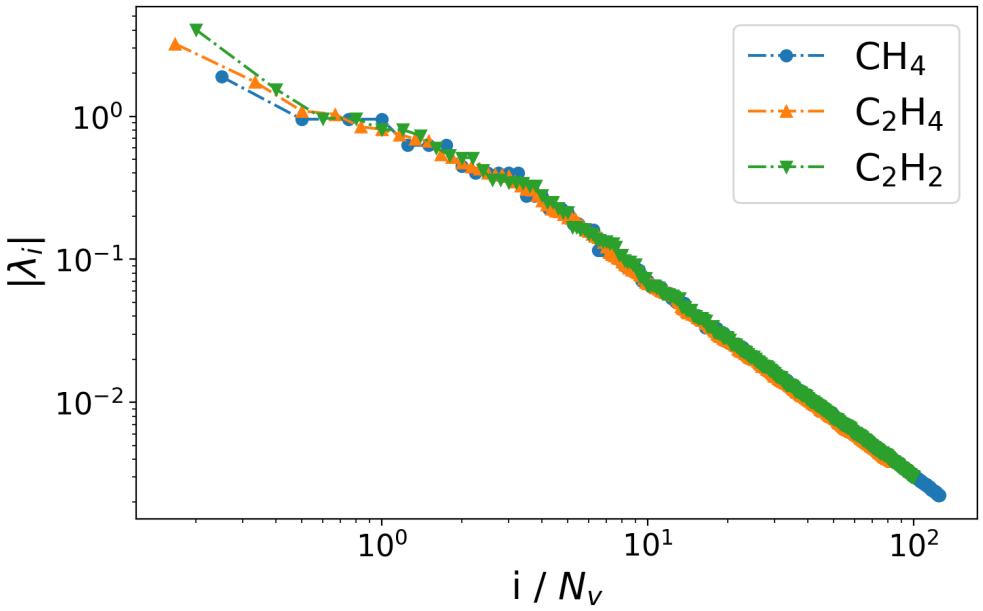

Figure 3.1: First 500 eigenvalues λ_i of the symmetrized irreducible density-density response function $\tilde{\chi}_0$ (see text), for three small molecules: CH_4 (blue dots), C_2H_4 (orange up triangles), and C_2H_2 (green down triangles). N_v is the number of occupied orbitals.

We used the PBE exchange-correlation functional, a plane wave energy cutoff of 40 Ry and cell size of 40 bohr, the same as used in Ref. 107. We performed two groups of calculations starting with 100 and 200 standard eigenpotentials, respectively. For both calculations, we computed quasiparticle energies by adding 100, 200, 300, 400 kinetic eigenpotentials and extrapolation was done in the same manner. As seen in Table 3.3, the results obtained with 200 standard eigenpotentials and additional kinetic eigenpotentials differ at most by 0.1 eV from those computed with standard eigenpotentials (extrapolated up to $N_{\text{stdPDEP}} = 2000$). The two sets of calculations starting with $N_{\text{stdPDEP}} = 100$ and $N_{\text{kinPDEP}} = 200$ amounted to savings of 32% and 15%, respectively.

We now turn to a more complex system, amorphous silicon nitride interfaced with a silicon surface (Si_3N_4/Si(100)), whose structure was taken from Ref. 106 (See Figure 3.6). This interface is representative of a heterogeneous, low dimensional system.

We computed band offsets (BO) by employing two different methods. The first one is

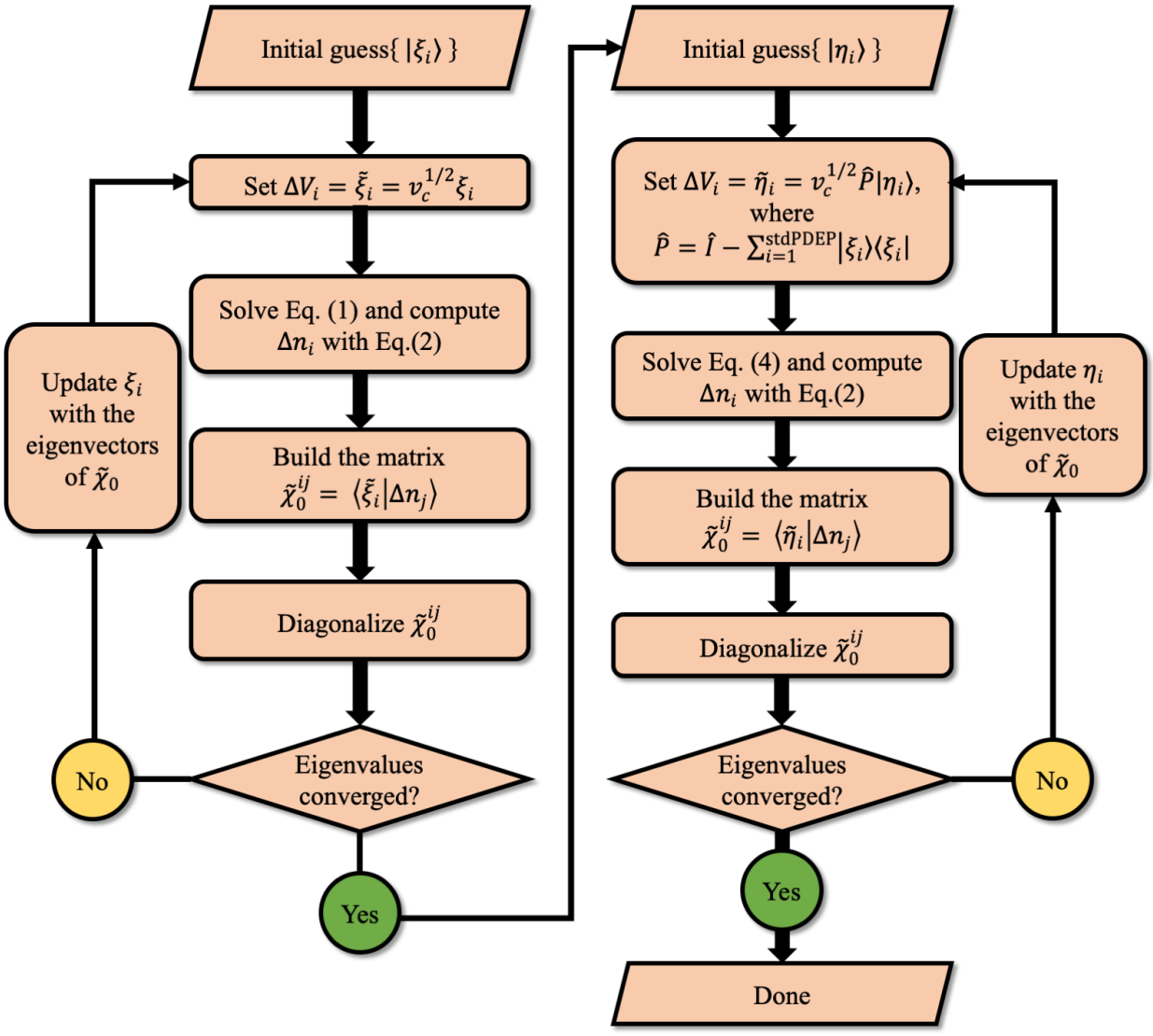

Figure 3.2: The workflow used in this work to generate eigenvectors of the dielectric matrix using the Kohn-Sham Hamiltonian (stdPDEP) and using the kinetic operator (kinPDEP). See text.

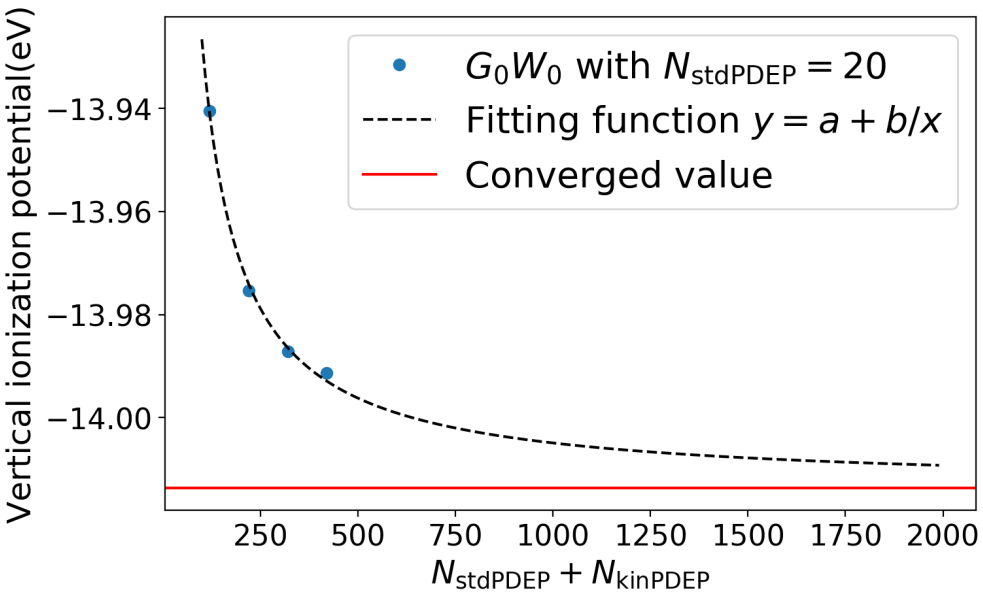

Figure 3.3: Extrapolation of G_0W_0 energy of highest occupied orbital of methane with respect to total number of eigenpotential used ($N_{\text{stdPDEP}} + N_{\text{kinPDEP}}$). In this plot, $N_{\text{stdPDEP}} = 20$ and $N_{\text{kinPDEP}} = 100$, 200, 300, 400 for the four points, respectively.

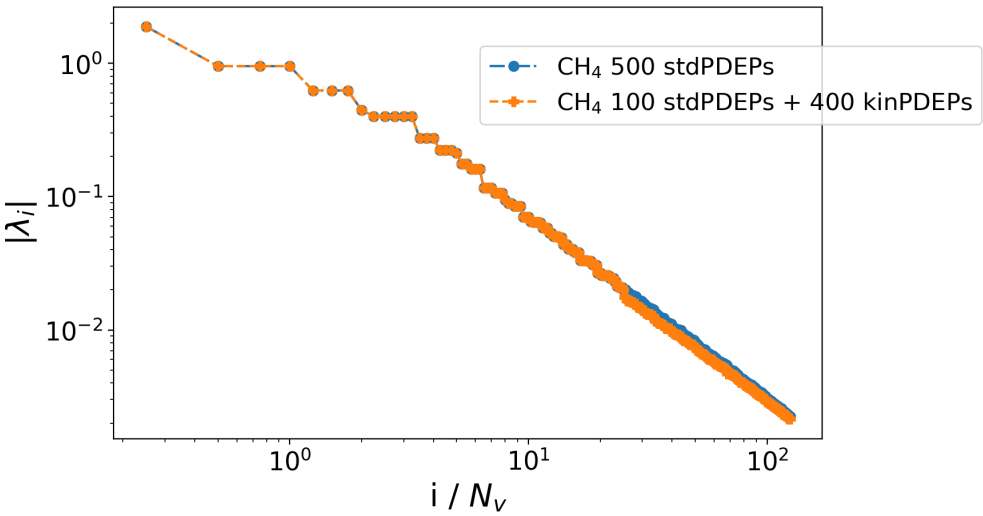

Figure 3.4: Comparison between the eigenvalues (λ_i) of the leading 500 stdPDEPs and the eigenvalues of the 100 leading stdPDEPs followed by 400 kinPDEPs of the CH4 molecule. N_v is the number of occupied states and stdPDEPs and kinPDEPs are eigenvectors of the symmetrized irreducible density-density response function($\tilde{\chi}_0$) solved using Kohn-Sham Hamiltonian and kinetic operator.

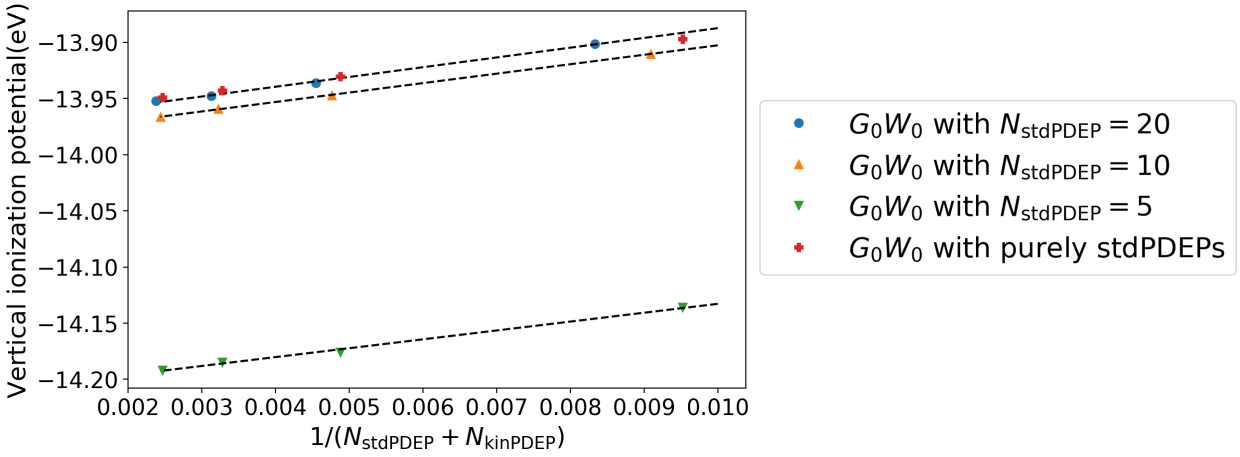

Figure 3.5: Calculations of the vertical ionization potential of the methane molecule with 20, 10, 5 standard eigenpotentials (stdPDEP) and up to 400 kinetic eigenpotentials (kinPDEP) compared to calculations (red symbols) performed with purely stdPDEPs.

Table 3.3: Quasiparticle energies (eV) of C_{60} calculated at the G_0W_0@PBE level of theory. Energy levels are labeled by their symmetry in point group I_h. $N_{\mathrm{stdPDEP}} = 100$ and $N_{\mathrm{stdPDEP}} = 200$ are calculations with 100 and 200 stdPDEPs and up to 400 kinPDEPs and extrapolated. $N_{\mathrm{kinPDEP}} = 0$ is the calculation with pure stdPDEPs and extrapolated. (See text)

Energy levels	$N_{\mathrm{stdPDEP}} = 100$	$N_{\mathrm{stdPDEP}} = 200$	$N_{\mathrm{kinPDEP}} = 0$	G_0W_0	Expt
t_{1g}	-1.70	-1.66	-1.70		
t_{1u}	-2.70	-2.77	-2.82	-2.74[a] -2.62[b] -2.82[c]	-2.69[d]
h_u	-7.32	-7.32	-7.38	-7.31[a] -7.21[b] -7.37[c]	-7.61[d] -7.6[e]
$g_g + h_g$	-8.46, -8.52	-8.46, -8.51	-8.51, -8.56	-8.68[c] -8.69[c]	-8.59[e]

[a] Ref. 107: with 700 standard eigenpotentials;
[b] Ref. 121: with 27387 SAPOs, where SAPO stands for simple approximate physical orbitals;
[c] Ref. 112: plane wave energy cutoff of 45 Ry and cell edge of 31.7 bohr;
[d] Ref. 80;
[e] Ref. 77.

based on the calculation of the local density of electronic states (LDOS);[106, 146] the second one is based on the calculation of the average electrostatic potential which is then used to set a common zero of energy on the two parts of the slab representing the two solids interfaced with each other.[140] The average electrostatic potential was fitted with the method proposed in Ref. 136. We used a plane wave energy cutoff of 70 Ry. We also performed G_0W_0@PBE calculations for each bulk system separately and obtained quasiparticle energies.

The local density of states is given by:

$$D(\varepsilon, z) = 2\sum_i \int \frac{\mathrm{d}x}{L_x} \int \frac{\mathrm{d}y}{L_y} |\psi_i(x, y, z)|^2 \delta(\varepsilon - \varepsilon_i), \tag{3.6}$$

where z is the direction perpendicular to the interface, $\psi_i(x, y, z)$ is the wavefunction, the factor 2 represents spin degeneracy. We computed the variation of the valence band maximum(VBM) and conduction band minimum(CBM) as a function of the direction (z) perpendicular to the interface[106]

$$\int_{\mathrm{VBM}}^{E_F} D(\varepsilon, z)\,\mathrm{d}\varepsilon = \int_{E_F}^{\mathrm{CBM}} D(\varepsilon, z)\,\mathrm{d}\varepsilon = \Delta \int_{-\infty}^{E_F} D(\varepsilon, z)\,\mathrm{d}\varepsilon, \tag{3.7}$$

where E_F is the Fermi energy and Δ is an constant that is chosen to be 0.003.[106] We follow a common procedure adopted to describe the electronic structure of interfaces described in Ref. 106 and 146. The band offsets (see Table 3.5) at the PBE level of theory were determined to be 0.83 eV and 1.49 eV for the valence band and conduction band, respectively, which are in agreement with the results of 0.8 eV and 1.5 eV reported in Ref. 106.

As mentioned above, another method to obtain the valence band offset (VBO) and conduction band offset (CBO) is to align energy levels with respect to electrostatic potentials. Following Ref. 136, the electrostatic potential was computed as:

$$\bar{V}(\mathbf{r}) = V_H(\mathbf{r}) + V_{\mathrm{loc}}(\mathbf{r}) - \sum_i \bar{V}_{\mathrm{at}}^{(i)}(|\mathbf{r} - \mathbf{r}_i|), \tag{3.8}$$

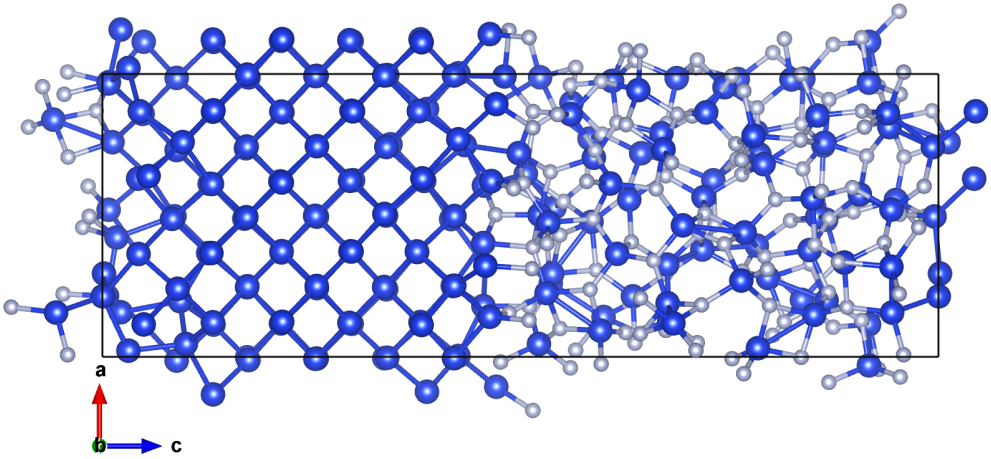

Figure 3.6: Ball and stick representation of the atomistic structure[106] of the Si_3N_4/Si(100) interface used in our study.

where $\bar{V}_{\text{at}}^{(i)}$ is the potential near the core region obtained from neutral atom calculations. With this method, VBO and CBO at the PBE level are found to be 0.89 eV and 1.63 eV.

To compute G_0W_0 corrections on band offsets, we performed G_0W_0@PBE calculations of bulk silicon and amorphous silicon nitride. In Table 3.4, quasiparticle corrections to Kohn-Sham energies of bulk silicon and amorphous silicon nitride are shown. The second and third columns are computed with 1000 and 2000 standard eigenpotentials. The fitted G_0W_0 reference results are extrapolated with 500, 1000, 1500 and 2000 standard eigenpotentials. To test accuracy of kinetic eigenpotentials, we started with 400 stdPDEPs and added 100, 200, 300, 400 kinPDEPs, after which the same extrapolation was applied. We calculated VBO and CBO at the G_0W_0 level by applying quasiparticle corrections on PBE results. After applying quasiparticle corrections on LDOS results, VBO and CBO are 1.41 eV and 1.88 eV while the VBO and CBO are found to be 1.46 eV and 2.02 eV after applying corrections to results based on electrostatic potential alignment. Both of them are close to the range of experimental results of $1.5 - 1.78$ eV and $1.82 - 2.83$ eV. Time saving when using kinetic eigenpotentials to obtain quasiparticle corrections was approximately $\sim 50\%$.

Table 3.4: Quasiparticle energies of valence band maximum (VBM) and conduction band minimum (CBM) of bulk silicon and amorphous Si_3N_4 computed with standard eigenpotentials and by combining standard and kinetic eigenpotentials. Columns $N_{\text{stdPDEP}} = 1000$ and $N_{\text{stdPDEP}} = 2000$ report calculations performed with 1000 and 2000 stdPDEPs; column Fit reports extrapolated results; column $N_{\text{kinPDEP}} = 400$ reports calculations with up to 400 kinPDEPs and then extrapolated. (See text)

	$N_{\text{stdPDEP}} = 1000$	$N_{\text{stdPDEP}} = 2000$	Fit	$N_{\text{kinPDEP}} = 400$
Si VBM	5.70	5.55	5.45	5.53
Si CBM	7.03	6.91	6.79	6.82
$a - Si_3N_4$ VBM	7.14	7.01	7.01	6.99
$a - Si_3N_4$ CBM	11.99	11.87	11.83	11.83

Table 3.5: Band gaps of bulk Si, $a - Si_3N_4$, and band offsets (VBO&CBO) of the interface.(see Figure 3.6) All values are in eV.

Method \ Energy		VBO	CBO	E_g^{Si}	$E_g^{Si_3N_4}$
PBE	LDOS	0.83	1.49	0.67	3.19
	Potential	0.89	1.63	0.76	3.19
	Ref[a]	0.8	1.5	0.7	3.17
G_0W_0	LDOS	1.41	1.88	1.29	4.77
	Potential	1.46	2.02	1.29	4.77
	Ref[a]	1.5	1.9	1.3	4.87
Expt		1.5-1.78[b]	1.82-2.83[c]	1.17[d]	4.5-5.5[e]

[a] Ref. 106;
[b] Ref. 69, 54, 62;
[c] Estimated by the other three experimental values;
[d] Ref. 70;
[e] Ref. 50, 11, 31.

3.4 Conclusion

The method introduced in Ref. 98, 107, 51, 52 to compute quasiparticle energies using the G_0W_0 approximation avoids the calculation of virtual electronic states and the inversion and storage of large dielectric matrices, thus leading to substantial computational savings. Building on the strategy proposed in Ref. [143, 144] and implemented in the WEST code,[51] here we proposed an approximation of the spectral decomposition of dielectric matrices that further improve the efficiency of G_0W_0 calculations. In particular we built sets of eigenpotentials used as a basis to expand the Green function and the screened Coulomb interaction by solving two separate Sternheimer equations: one using the Hamiltonian of the system to obtain the eigenvectors corresponding to the lowest eigenvalues of the response function, and the other using just the kinetic energy operator to obtain the eigenpotentials corresponding to higher eigenvalues. We showed that without compromising much accuracy, this approximation reduces the cost of G_0W_0 calculations by 10%-50%, depending on the system, with the most savings observed for the largest systems studied here.

CHAPTER 4

COMBINED FIRST-PRINCIPLES CALCULATIONS OF ELECTRON-ELECTRON AND ELECTRON-PHONON SELF-ENERGIES IN CONDENSED SYSTEMS

We present a method to efficiently combine the computation of electron-electron and electron-phonon self-energies, which enables the evaluation of electron-phonon coupling at the G_0W_0 level of theory for systems with hundreds of atoms. In addition, our approach, which is a generalization of a method recently proposed for molecules,[92] enables the inclusion of non-adiabatic and temperature effects at no additional computational cost. We present results for diamond and defects in diamond and discuss the importance of numerically accurate G_0W_0 band structures to obtain robust predictions of zero point renormalization (ZPR) of band gaps, and of the inclusion of non-adiabatic effect to accurately compute the ZPR of defect states in the band gap. The Illustration of the development is shown in Figure 4.1.

This chapter is reproduced from Han Yang, Marco Govoni, Arpan Kundu, and Giulia Galli. *Combined first-principles calculations of electron-electron and electron-phonon self-energies in condensed systems.* https://arxiv.org/abs/2106.10373, which is under review in the Journal of Chemical Theory and Computation and Arpan Kundu, Marco Govoni, Han Yang, Michele Ceriotti, Francois Gygi, and Giulia Galli *Quantum vibronic effects on the electronic properties of solid and molecular carbon.* https://doi.org/10.1103/PhysRevMaterials.5.L070801

4.1 Introduction

The interaction between electrons and phonons in solids[43, 45, 6] gives rise to a variety of interesting physical phenomena, including superconductivity[9], and to complex electronic structure properties in metals, semiconductors and insulators[34]. Electron-phonon coupling

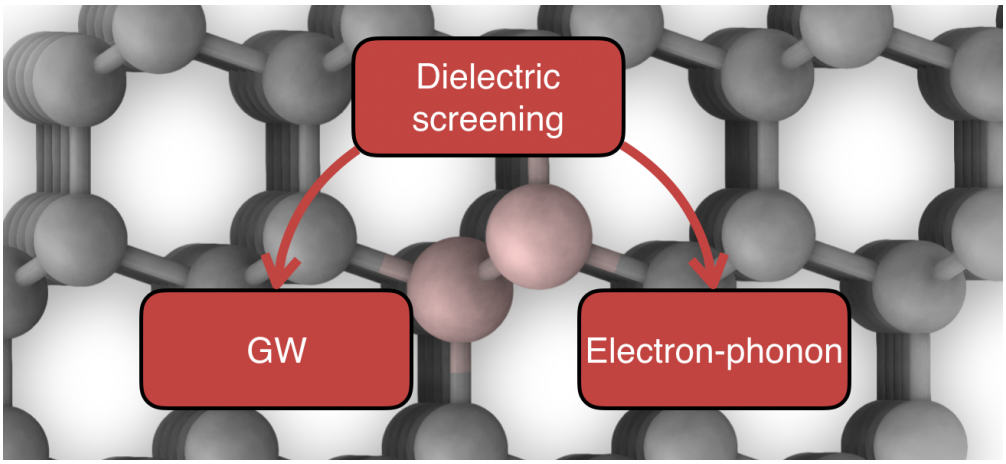

Figure 4.1: Illustration of the idea to combine the calculations of electron-electron and electron-phonon interactions by reusing the dielectric screening. In the background, we are showing a specific defect in diamond to showcase our ability to perform calculations for large-scale systems.

has been widely studied for more than half a century[36]. However, it is only in the last two decades that first principles, quantum mechanical methods have been applied to carry out quantitative calculations[44, 43, 6], based on frozen-phonon approaches[96, 94, 95, 6, 68], density functional perturbation theory (DFPT)[42, 10, 43, 6, 109, 22, 23] and, very recently, path-integral molecular dynamics simulations based on density functional theory (DFT)[72].

The frozen-phonon approach is straightforward to implement, compared to other methods, as the phonon frequencies and electron-phonon renormalization energies are simply computed by displacing the nuclear positions and solving the Kohn-Sham equations at each displaced position[6, 24, 96, 94]. However, the frozen-phonon approach is difficult to converge with respect to the supercell size, [10, 43] and using this method it is challenging to accurately describe polar systems[110, 93]. Hence, perturbative approaches have been widely used. Most of them solve the electronic structure problem at the level of density functional theory (DFT)[6, 22, 23] and compute electron-phonon coupling within the Allen-Heine-Cardona (AHC) formalism[4, 3, 45]. However, some formulations have been recently proposed to go beyond the approximations of the AHC approach, and include non-adiabatic [109, 110, 93], dynamical[22, 23, 7] and/or non-rigid-ion[109] effects in the calculation of

electron-phonon interactions. It has also been shown that for several solids many-body perturbation theory (MBPT)[45, 6, 94] is necessary in order to obtain results in quantitative agreement with experiments, and GW corrections have been applied to compute electron-coupling matrices[75, 76] and/or DFT single particle energy levels[45, 6, 92]. Given the computational cost involved in electron-phonon calculations based on MBPT, e.g., at the G_0W_0 level, plasmon-pole models (PPM) are often employed[66, 6, 94, 75, 46] to approximate the frequency dependence of the self-energy, in spite of some known deficiencies of such models[91].

With the goal of improving the accuracy and efficiency of electron-phonon calculations within MBPT, we recently proposed [92] a method that combines the evaluation of electron–electron and electron–phonon self-energies. The dielectric matrix is represented in terms of dielectric eigenpotentials[143, 144], utilized for both the calculation of G_0W_0 quasiparticle energies and the diagonalization of the dynamical matrix; virtual electronic states are not explicitly computed; dielectric matrices, being represented using a spectral decomposition, are never inverted, and all self-energies are evaluated over the full frequency spectrum using the Lanczos algorithm.[107, 51, 52]. Importantly, our implementation also enables at no extra cost the evaluation of non-adiabatic effects and electron-phonon self energies at multiple temperatures and frequencies. Although in principle the method is general, in practice it has so far been applied only to finite systems within the adiabatic approximation.

In this work, we generalize the combined electron-electron and electron-phonon approach described in Ref. 92 to solids and, after presenting a detailed verification and validation protocol, we apply the approach to large supercells with about 1000 electrons, which are representative of defective solids. We report results as a function of temperature and we study in detail the effect of including non-adiabatic terms in the zero point renormalization of the band gap of pristine and defective diamond and on defect states.

The rest of this work is organized as follows: we first describe our methodology and

then verify our implementation and validate our results for specific systems; we then present applications of the method to point defects in diamond.

4.2 Methodology

4.2.1 Dynamical and electron-phonon coupling matrices

In a periodic system, phonon frequencies are computed by diagonalizing the dynamical matrix[10]

$$D_{I\alpha,J\beta}(\mathbf{q}) = \frac{1}{\sqrt{M_I M_J}} C_{I\alpha,J\beta}(\mathbf{q}) = \frac{1}{\sqrt{M_I M_J}} \frac{\partial^2 E}{\partial u^*_{I\alpha}(\mathbf{q}) \partial u_{J\beta}(\mathbf{q})}, \tag{4.1}$$

where $C_{I\alpha,J\beta}(\mathbf{q})$ is a force constant, E is the total energy of the system, u denotes displacements from equilibrium atomic positions, M_I, M_J are atomic masses, I, J are indices of atoms, α, β are Cartesian directions, and $\mathbf{q}$ is the wave-vector of the phonon mode.

The force constants are given by the sum of an electronic and ionic part, with the latter being trivial to evaluate. Within the framework of density functional perturbation theory (DFPT), the electronic contribution can be written as

$$C^{elec}_{I\alpha,J\beta}(\mathbf{q}) = \sum_{n}^{occ} \sum_{\mathbf{k}} \left\langle \psi_{n\mathbf{k}} \left| \partial_{J\beta,\mathbf{q}} V_{ext} \right| \partial_{I\alpha,\mathbf{q}} \psi_{n\mathbf{k}} \right\rangle + c.c., \tag{4.2}$$

where $\mathbf{k}$ is a k-point within the Brillouin zone, $\psi_{n\mathbf{k}}$ is the wavefunction of the n-th band at $\mathbf{k}$, and V_{ext} is the external ionic potential. For simplicity, we denoted the derivative $\partial / \partial u_{I\alpha}(\mathbf{q})$ as $\partial_{I\alpha,\mathbf{q}}$. The braket in Eq. (4.2) is commonly computed by solving the Sternheimer equation self-consistently,

$$(\hat{H}_{KS} - \varepsilon_{n\mathbf{k}}) \left| \partial_{I\alpha,\mathbf{q}} \psi_{n\mathbf{k}} \right\rangle = -\hat{\mathcal{P}}^{c}_{\mathbf{k}+\mathbf{q}} \partial_{I\alpha,\mathbf{q}} \hat{V}_{SCF} \left| \psi_{n\mathbf{k}} \right\rangle, \tag{4.3}$$

where $\hat{H}_{KS} = \hat{K} + \hat{V}_{SCF}$ is the Kohn-Sham Hamiltonian; $\hat{K}$ is the kinetic operator; $\hat{V}_{SCF}$ is the self-consistent potential operator; $\varepsilon_{n\mathbf{k}}$ is the Kohn-Sham eigenvalue of the n-th band at the $\mathbf{k}$ point, $\partial_{I\alpha,\mathbf{q}}\hat{V}_{SCF}$ is the first order change of the self-consistent potential due to atomic displacements, $\partial_{I\alpha,\mathbf{q}}\psi_{n\mathbf{k}}$ denotes the first order change of the wavefunction, and $\hat{\mathcal{P}}^{c}_{\mathbf{k}+\mathbf{q}} = \hat{I} - \sum_{v}^{occ} \left|\psi_{v\mathbf{k}+\mathbf{q}}\right\rangle \left\langle\psi_{v\mathbf{k}+\mathbf{q}}\right|$ is the projection operator onto the manifold of unoccupied (virtual) single particle electronic states.

Instead of solving the Sternheimer equation self-consistently, we write the braket in Eq. (4.2) as:[92]

$$\left\langle \psi_{n\mathbf{k}} \left| \partial_{J\beta,\mathbf{q}} V_{ext} \right| \partial_{I\alpha,\mathbf{q}} \psi_{n\mathbf{k}} \right\rangle = \left\langle \partial_{J\beta,\mathbf{q}} \psi^{bare}_{n\mathbf{k}} \left| \partial_{I\alpha,\mathbf{q}} V_{SCF} \right| \psi_{n\mathbf{k}} \right\rangle, \tag{4.4}$$

where the change of the wavefunction is obtained through the one-shot solution of the Sternheimer equation

$$(\hat{H}_{KS} - \varepsilon_{n\mathbf{k}}) \left| \partial_{I\alpha,\mathbf{q}} \psi^{bare}_{n\mathbf{k}} \right\rangle = -\hat{\mathcal{P}}^{c}_{\mathbf{k}+\mathbf{q}} \partial_{I\alpha,\mathbf{q}} \hat{V}_{ext} \left| \psi_{n\mathbf{k}} \right\rangle. \tag{4.5}$$

The change of SCF potential can be evaluated from $\partial_{I\alpha,\mathbf{q}}\hat{V}_{ext}$ as

$$\partial_{I\alpha,\mathbf{q}} V_{SCF} = \partial_{I\alpha,\mathbf{q}} V_{ext} + [f_{Hxc} + f_{Hxc}\chi f_{Hxc}] \partial_{I\alpha,\mathbf{q}} \rho^{bare}, \tag{4.6}$$

where $f_{Hxc} = v_c + f_{xc}$ is the sum of the bare Coulomb potential, v_c, and the exchange-correlation kernel, f_{xc}; χ is the reducible density-density response function and $\partial_{I\alpha,\mathbf{q}}\rho^{bare}$ is the derivative of the bare change of density,

$$\partial_{I\alpha,\mathbf{q}} \rho^{bare} = \sum_{n}^{occ} \sum_{\mathbf{k}} \left[\psi^{*}_{n\mathbf{k}} \partial_{I\alpha,\mathbf{q}} \psi^{bare}_{n\mathbf{k}} + c.c. \right]. \tag{4.7}$$

In order to efficiently evaluate the reducible density-density response function, χ, we represent the irreducible density-density response function, χ_0, in terms of projective dielectric

eigenpotentials (PDEP)[144, 107, 51, 147] and we represent χ with the same basis used as that of χ_0:

$$\chi_0(\mathbf{q}) = \sum_{i}^{N_{\mathrm{PDEP}}} |\phi_i(\mathbf{q})\rangle \, \lambda_i(\mathbf{q}) \, \langle \phi_i(\mathbf{q})| \,, \tag{4.8}$$

where i is the index of the PDEP basis, $\phi_i(\mathbf{q})$ and $\lambda_i(\mathbf{q})$ are the i-th eigenvector and eigenvalue of the symmetrized reducible polarizability, N_{PDEP} is the number of PDEP basis functions, respectively. Using the Dyson equation $\chi = \chi_0 + \chi_0 f_{Hxc} \chi$, the reducible density-density response function can be evaluated using the PDEP basis set:

$$\chi = (1 - \chi_0 f_{Hxc})^{-1} \chi_0. \tag{4.9}$$

Adopting the procedure described above, we can compute the dynamical matrix $D(\mathbf{q})$:

$$\sum_{J\beta} D_{I\alpha,J\beta}(\mathbf{q}) \xi_{J\beta,\mathbf{q}\nu} = \omega^2_{\mathbf{q}\nu} \xi_{I\alpha,\mathbf{q}\nu}, \tag{4.10}$$

where $\omega_{\mathbf{q}\nu}$ are phonon frequencies and $\xi_{I\alpha,\mathbf{q}\nu}$ are phonon eigenvectors. Finally, Eq. (4.6) is used to evaluate the electron-phonon coupling matrix elements g given by:[43]

$$g_{mn\nu}(\mathbf{k},\mathbf{q}) = \left\langle \psi_{m\mathbf{k}+\mathbf{q}} \left| \partial_{\mathbf{q}\nu} V_{SCF} \right| \psi_{n\mathbf{k}} \right\rangle, \tag{4.11}$$

where $\partial_{\mathbf{q}\nu} V_{SCF}$ is the mode-resolved change of potential,

$$\partial_{\mathbf{q}\nu} V_{SCF} = \sum_{I\alpha} \frac{\xi_{I\alpha,\mathbf{q}\nu}}{\sqrt{2M_I \omega_{\mathbf{q}\nu}}} \partial_{I\alpha,\mathbf{q}} V_{SCF}. \tag{4.12}$$

4.2.2 Electron-phonon self-energy

Within many-body perturbation theory (MBPT)[43, 91], the electron-phonon self-energy has two components, the Fan-Migdal:

$$\Sigma^{\rm FM}_{n\mathbf{k}}(\omega,T)=\sum_{m\nu\mathbf{q}}|g_{mn\nu}(\mathbf{k},\mathbf{q})|^2\left[\frac{n_{\mathbf{q}\nu}+f_{m\mathbf{k}+\mathbf{q}}}{\omega-\varepsilon_{m\mathbf{k}+\mathbf{q}}+\omega_{\mathbf{q}\nu}-i0^+}+\frac{n_{\mathbf{q}\nu}+1-f_{m\mathbf{k}+\mathbf{q}}}{\omega-\varepsilon_{m\mathbf{k}+\mathbf{q}}-\omega_{\mathbf{q}\nu}-i0^+}\right] \tag{4.13}$$

and Debye-Waller:

$$\Sigma^{DW}_{n\mathbf{k}}(T)=-\sum_{m\nu\mathbf{q}}\sum_{I\alpha J\beta}\frac{2n_{\mathbf{q}\nu}+1}{\varepsilon_{n\mathbf{k}}-\varepsilon_{m\mathbf{k}}}\frac{1}{4\omega_{\mathbf{q}\nu}}\left[\frac{\xi_{I\alpha,\mathbf{q}\nu}\xi^*_{I\beta,\mathbf{q}\nu}}{M_I}+\frac{\xi_{J\alpha,\mathbf{q}\nu}\xi^*_{J\beta,\mathbf{q}\nu}}{M_J}\right]g^{*,I\alpha}_{mn}(\mathbf{k},\mathbf{0})g^{J\beta}_{mn}(\mathbf{k},\mathbf{0}), \tag{4.14}$$

where $n_{\mathbf{q}\nu}$ and $f_{m\mathbf{k}+\mathbf{q}}$ are Bose-Einstein and Fermi-Dirac distributions, respectively. We note that the expression of the Debye-Waller self-energy of Eq. (4.14) is written by assuming the rigid-ion approximation, in which the second-order expression of the electron-phonon coupling matrix elements are approximated with their respective first-order expressions. The effect of this approximation has been thoroughly studied in Ref. 109. When adopting the AHC formalism,[4, 3] in our calculations, we assume the on-mass-shell approximation i.e., $\omega=\varepsilon_{n\mathbf{k}}$ and the adiabatic approximation, i.e., $\varepsilon_{n\mathbf{k}}-\varepsilon_{m\mathbf{k}+\mathbf{q}}\gg\omega_{\mathbf{q}\nu}$. However, in some cases discussed below we did not adopt the adiabatic approximation. Within the AHC formalism, the real part of the Fan-Migdal self-energy can be simplified:

$$\mathbf{Re}\,\Sigma^{FM}_{n\mathbf{k}}(T)\approx\sum_{m\nu\mathbf{q}}|g_{mn\nu}(\mathbf{k},\mathbf{q})|^2\left[\frac{2n_{\mathbf{q}\nu}+1}{\varepsilon_{n\mathbf{k}}-\varepsilon_{m\mathbf{k}+\mathbf{q}}}\right]. \tag{4.15}$$

To avoid summations over empty bands in the evaluation of Fan-Migdal and Debye-Waller self-energies (Eq. (4.13) – (4.15)), here we use the Lanczos approach. Writing the Fan-Migdal self-energy within the AHC approximation (Eq. (4.15)) as an example, we first

expand the electron-phonon coupling matrix using Eq. (4.11),

$$\Sigma^{FM}_{n\mathbf{k}} = \sum_{m\nu\mathbf{q}} \left\langle \psi_{n\mathbf{k}} \left| \partial_{-\mathbf{q}\nu} V_{SCF} \right| \psi_{m\mathbf{k}+\mathbf{q}} \right\rangle \frac{2n_{\mathbf{q}\nu}+1}{\varepsilon_{n\mathbf{k}} - \varepsilon_{m\mathbf{k}+\mathbf{q}}} \left\langle \psi_{m\mathbf{k}+\mathbf{q}} \left| \partial_{\mathbf{q}\nu} V_{SCF} \right| \psi_{n\mathbf{k}} \right\rangle . \quad (4.16)$$

Given the projection of the Hamiltonian on the conduction (virtual) manifold, i.e., $\tilde{H}_{\mathbf{k}+\mathbf{q}} = \hat{\mathcal{P}}^{c}_{\mathbf{k}+\mathbf{q}} H \hat{\mathcal{P}}^{c}_{\mathbf{k}+\mathbf{q}}$, we can write

$$\sum_{m} \left| \psi_{m\mathbf{k}+\mathbf{q}} \right\rangle (\varepsilon_{n\mathbf{k}} - \varepsilon_{m\mathbf{k}+\mathbf{q}})^{-1} \left\langle \psi_{m\mathbf{k}+\mathbf{q}} \right| = (\varepsilon_{n\mathbf{k}} - \tilde{H}_{\mathbf{k}+\mathbf{q}})^{-1}. \quad (4.17)$$

Eq. (4.17) may be efficiently solved using the Lanczos approach, and the imaginary part of the Fan-Migdal self energy and the Debye-Waller self-energy (Eq. (4.13)-(4.14)) may be computed in a similar manner.

Staring from Eq.(4.17), we define $A_{n\mathbf{k}}(\tilde{H}_{\mathbf{k}+\mathbf{q}}) = (\varepsilon_{n\mathbf{k}} - \tilde{H}_{\mathbf{k}+\mathbf{q}})^{-1}$, and Eq.(4.17) can be written as,

$$A_{n\mathbf{k}}(\tilde{H}_{\mathbf{k}+\mathbf{q}}) = \sum_{m} \left| \psi_{m\mathbf{k}+\mathbf{q}} \right\rangle A_{n\mathbf{k}}(\varepsilon_{m\mathbf{k}+\mathbf{q}}) \left\langle \psi_{m\mathbf{k}+\mathbf{q}} \right| \quad (4.18)$$

Following references[74, 92], we obtain the Lanczos basis $\tilde{q}_l$ and corresponding eigenvalues d_l of $\tilde{H}_{\mathbf{k}+\mathbf{q}}$, and thus the self-energy can be written as

$$\Sigma^{FM}_{n\mathbf{k}}(T) = \sum_{\nu\mathbf{q}l} \left\langle L^{\mathbf{q}\nu}_{n\mathbf{k}} | \tilde{q}_l \right\rangle A_{n\mathbf{k}}(d_l) \left\langle \tilde{q}_l | R^{\mathbf{q}\nu}_{n\mathbf{k}} \right\rangle [2n_{\mathbf{q}\nu}(T) + 1], \quad (4.19)$$

where $\left| L^{\mathbf{q}\nu}_{n\mathbf{k}} \right\rangle$ and $\left| R^{\mathbf{q}\nu}_{n\mathbf{k}} \right\rangle$ are vectors within the set $\{ \left| \partial_{\mathbf{q}\nu} V_{SCF} \psi_{n\mathbf{k}} \right\rangle , n = 1, 2, \cdots \}$.

In the following, we describe how to compute Lanczos basis functions, and hereafter we drop the superscripts and subscripts of $|L\rangle$ and $|R\rangle$ for simplicity. The Lanczos basis

functions and eigenvalues can be obtained by diagonalizing the matrix

$$Q^{\dagger}\tilde{H}Q = \begin{pmatrix} \alpha_1 & \beta_2 & & & \\ \beta_2 & \alpha_2 & \beta_3 & & \\ & \beta_3 & \ddots & \ddots & \\ & & \ddots & \ddots & \beta_n \\ & & & \beta_n & \alpha_n \end{pmatrix}, \tag{4.20}$$

where $Q = \{|q_l\rangle\,,\, l = 1, 2, \cdots, N_{\text{Lanczos}}\}$ with $|q_1\rangle = |R\rangle$ are a set of orthonormal vectors, and the elements of the matrix are obtained from

$$\alpha_n = \left\langle q_l \left| \tilde{H} \right| q_l \right\rangle \tag{4.21}$$

and

$$\beta_{n+1} = ||(\tilde{H} - \alpha_n)\,|q_n\rangle - \beta_n\,|q_{n-1}\rangle\,||. \tag{4.22}$$

The vectors $|q_l\rangle$ are orthogonalized with a recursive process by applying

$$|q_{n+1}\rangle = \frac{1}{\beta_{n+1}}\left[(\tilde{H} - \alpha_n)\,|q_n\rangle - \beta_n\,|q_{n-1}\rangle\right]. \tag{4.23}$$

The diagonalization of Eq. (4.20) yields the eigenvalues d_l and corresponding eigenvectors U_l. We then define a modified basis set $|\tilde{q}_l\rangle$ as a linear combination of the original basis $|q_l\rangle$,

$$|\tilde{q}_l\rangle = \sum_{k}^{N_{\text{Lanczos}}} U_l^k\,|q_k\rangle\,. \tag{4.24}$$

Having obtained the eigenvalues d_l of the matrix $Q^{\dagger}\tilde{H}Q$ and using the modified basis $|\tilde{q}_l\rangle$, we can evaluate the Fan-Migdal self-energy in Eq. (4.19), without summations over empty bands. A similar technique can be applied to obtain the Debye-Waller self-energy.

Table 4.1: First principles calculations of electron-phonon self-energies based on the G_0W_0 approximation. The integral of the self energy as a function of frequency is evaluated using either a plasmon-pole model (PPM) or by carrying out full-frequency (FF) integration using contour deformation.[51, 46] Evaluation of the G_0W_0 self-energy ($\Sigma_{G_0W_0}$) and of the electron-phonon self-energy (Σ_{ep}) are performed with algorithms requiring summation (S) over virtual states or no summation (NS) over virtual states. The evaluation of $\Sigma_{G_0W_0}$ and Σ_{ep} is combined in this work (Y) but carried out separately (N) in previous works.

	Ref. 45	Ref. 6	This work
Frequency Integration	PPM	PPM	FF
Evaluation of $\Sigma_{G_0W_0}$	S[a]	S	NS
Evaluation of Σ_{ep}	S	S/NS[b]	NS
Combined evaluation of $\Sigma_{G_0W_0}$ and Σ_{ep}	N	N	Y

[a] The G_0W_0 energy levels were not used in the evaluation of electron-phonon self-energies at G_0W_0 level, instead a scissor operator corresponding to the G_0W_0 correction was applied to DFT energy levels.

[b] No empty bands were used in the evaluation of electron-phonon self-energies at the DFT level. No information was provided on the calculations of empty states for G_0W_0 calculations.

In addition, we can compute the temperature-dependent, non-adiabatic or frequency-dependent self-energies without any extra computational cost, by reusing the Lanczos basis set defined above.

The approach described above was implemented in the `WEST` code[51, 92], interfaced with `Quantum Espresso` (version 6.1)[41] and the symmetries at $\mathbf{k}$ and $\mathbf{q}$ points were analyzed using the `PHonon` package[41].

A brief summary of the main features of the methodology presented here, compared to the implementations of first principles electron-phonon calculations used in the current literature, is given in Table (4.1).

4.3 Verification protocol

Our verification protocol includes first the comparison of phonon frequencies computed with standard DFPT based approaches with those of our methodology (Eq. (4.6)); we then carry out a study of the numerical parameters affecting the calculations of the ZPR of diamond within DFT and G_0W_0 and compare our results with those present in the literature.

Phonon frequencies – To verify our implementation, we first compared the phonon frequencies of the diamond crystal obtained with the method described above to those computed with the `PHonon` package in `Quantum Espresso`[41]. For verification purposes we carried out our calculations using the local density approximation (LDA), a cutoff of 60 Ry, Trouiller-Martins type pseudopotentials[139] generated with the `FHI98pp` code[37], and a $3 \times 3 \times 3$ **k**-point mesh.

Figure 4.2 shows that the interpolated phonon dispersion curves in diamond obtained with the two approaches are indistinguishable, with a mean absolute difference less than $1\,\mathrm{cm}^{-1}$. The comparison was repeated using energy cutoffs of 80, 100, and 120 Ry, for which we converged the phonon frequencies with respect to the number of PDEP eigenpotentials in the basis set. We found that the remaining small discrepancies not visible on the figure can be further reduced by increasing the cutoff Figure 4.3.

Zero point renormalization of energy levels at the DFT level of theory – We now turn to the discussion of electron-phonon self-energies. The real and imaginary parts of the electron-phonon self-energy yield the zero point renormalization and the lifetime of the single particle energy levels, respectively. To verify our implementation, we computed the ZPR of single particle energy levels in diamond at the DFT/LDA level of theory and compared our results with those reported in Ref. 6 and Ref. 109. In these two papers, the ZPRs are computed as

$$\Delta\varepsilon_{n\mathbf{k}}(T) = \frac{1}{N_{\mathbf{q}}} \sum_{\mathbf{q}\nu} \frac{\partial \varepsilon_{n\mathbf{k}}}{\partial n_{\mathbf{q}\nu}} \left[n_{\mathbf{q}\nu}(T) + \frac{1}{2} \right], \tag{4.25}$$

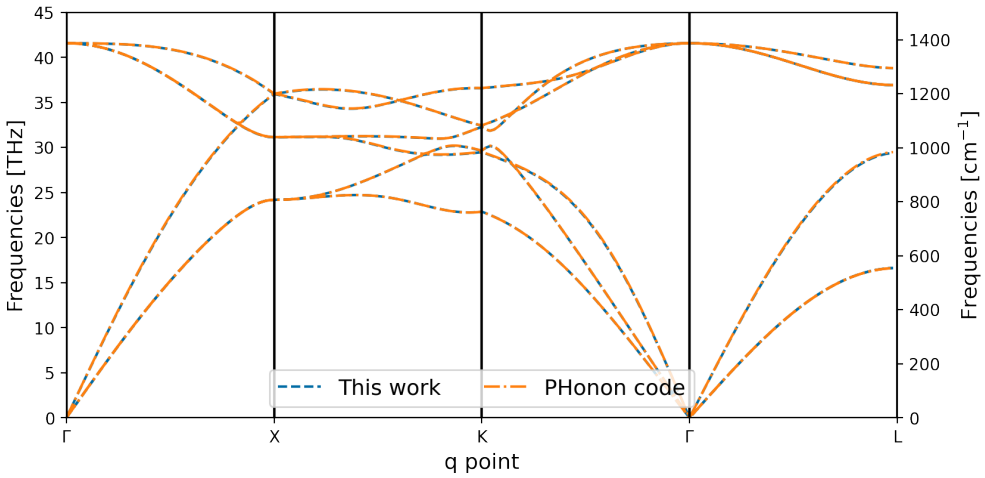

Figure 4.2: Phonon dispersion of diamond interpolated from $3 \times 3 \times 3$ **q**-point sampling.

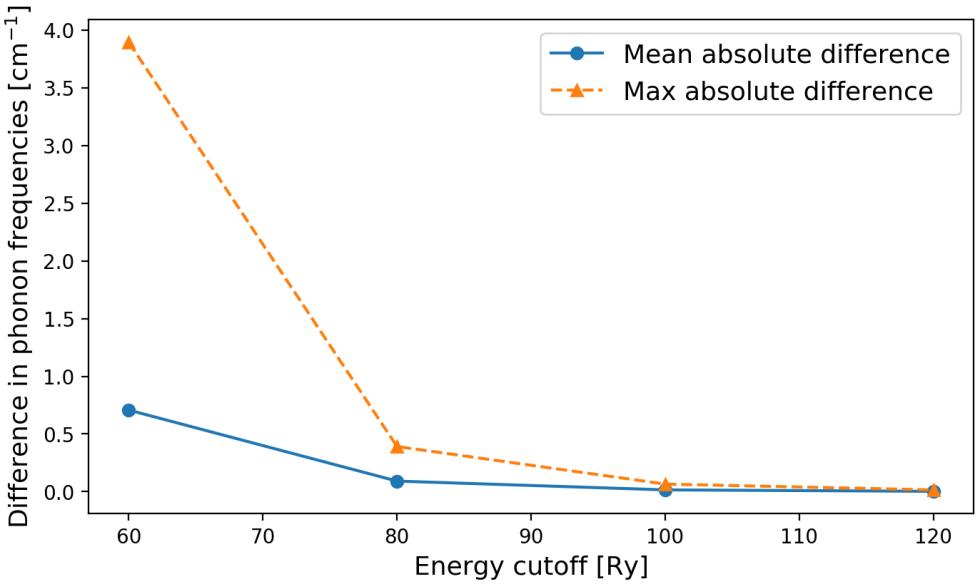

Figure 4.3: Difference in phonon frequencies [in cm^{-1}] computed with this work and `PHonon` package in `Quantum Espresso`.

where $N_{\mathbf{q}}$ is the number of $\mathbf{q}$ points and $\partial\varepsilon/\partial n$ is the electron-phonon coupling energy (EPCE). The latter can be evaluated using frozen-phonon or DFPT calculations,[109, 95] and here we report our results using DFPT and the AHC approximation,[4, 3, 109]

$$\frac{\partial\varepsilon^{FM}_{n\mathbf{k}}}{\partial n_{\nu\mathbf{q}}} = 2\sum_{m}\frac{|g_{nm\nu}(\mathbf{k},\mathbf{q})|^2}{\varepsilon_{n\mathbf{k}}-\varepsilon_{m\mathbf{k}+\mathbf{q}}}, \tag{4.26}$$

$$\frac{\partial\varepsilon^{DW}_{n\mathbf{k}}}{\partial n_{\nu\mathbf{q}}} = -\frac{1}{2\omega_{\mathbf{q}\nu}}\sum_{m}\sum_{I\alpha J\beta}\frac{1}{\varepsilon_{n\mathbf{k}}-\varepsilon_{m\mathbf{k}}}\left[\frac{\xi_{I\alpha,\mathbf{q}\nu}\xi^{*}_{I\beta,\mathbf{q}\nu}}{M_I}+\frac{\xi_{J\alpha,\mathbf{q}\nu}\xi^{*}_{J\beta,\mathbf{q}\nu}}{M_J}\right] g^{*,I\alpha}_{mn}(\mathbf{k},\mathbf{0})g^{J\beta}_{mn}(\mathbf{k},\mathbf{0}). \tag{4.27}$$

We computed EPCEs with the Troullier-Martins type pseudopotential[139], an energy cutoff of 60 Ry, and 6×6×6 **k**-point sampling, as in Ref. 109. We performed two sets of calculations, one using the lattice constant that we optimized at the LDA level (3.5185 Å), and the other using the lattice parameter (3.5323 Å) reported in Ref. 109. In Table 4.2 we compare the computed EPCEs with those in Ref.109 at $\mathbf{k}=\Gamma,\ L$ and $\mathbf{q}=\Gamma,\ L$. We find a mean absolute difference less than 3 meV and the mean absolute relative difference is $\sim 2\,\%$. The largest differences are observed at ($\mathbf{q}=\Gamma$, $\mathbf{k}=L_3$) and ($\mathbf{q}=L$, $\mathbf{k}=\Gamma_{2'}$). For ($\mathbf{q}=\Gamma,\mathbf{k}=L_3$), the EPCE computed with the optimized structure is −162.66 meV and the value reported in Ref.109 is −180.55 meV; for ($\mathbf{q}=L,\mathbf{k}=\Gamma_{2'}$), the EPCE computed with our code and the lattice constant of Ref.109 is −294.70 meV, to be compared to −307.54 meV, reported in Ref.109.

Ref. 109 reported EPCEs' values but did not report renormalizations of energy levels in diamond. Therefore, to verify our computed renormalizations, we compare our results with those of Ref. 6, using the same lattice parameter (3.5473 Å) and 4 × 4 × 4 **k**-point sampling. The computed renormalization of the highest occupied and lowest unoccupied bands at the Γ point are 116 and −319 meV, respectively, in good agreement with the values of 113 and −314 meV, reported in Ref.6. As a result, our computed renormalization of the direct gap in diamond is −439 meV, which also agrees very well with the result −427 meV of

Table 4.2: Electron-phonon coupling energies (see Eq. (4.25)) [meV] computed with optimized cell parameters (third column) and with the cell parameters reported by Ref. 109 (fourth column). Mean absolute differences (MAD)[meV] and mean absolute relative differences (MARD) are given in the last row.

q point	**k point**	**Optimized Cell**	**Cell parameter from Ref. 109**	**Ref. 109**
Γ	Γ_1	−12.55	−12.84	−12.53
	$\Gamma_{25'}$	25.13	24.86	24.83
	Γ_{15}	−14.87	−14.88	−14.23
	$\Gamma_{2'}$	−31.91	−30.86	−30.93
	$L_{2'}$	−21.18	−21.54	−20.98
	L_1	−16.72	−16.91	−16.60
	$L_{3'}$	10.14	10.02	10.10
	L_3	−162.66	−182.88	−180.55
L	Γ_1	−54.47	−55.15	−53.73
	$\Gamma_{25'}$	186.17	186.71	181.28
	Γ_{15}	−273.16	−274.86	−273.58
	$\Gamma_{2'}$	−311.89	−294.70	−307.54
	$L_{2'}$	−91.27	−91.96	−89.36
	L_1	−212.64	−224.15	−220.56
	$L_{3'}$	−26.88	−27.13	−25.91
	L_3	163.96	164.07	163.19
MAD [meV]		2.63	2.10	
MARD [%]		2.29 %	2.13 %	

Ref. 6. When using the lattice constant (3.5185 Å) optimized in our calculations, we obtain a renormalization energy of -429 meV and the difference compared to previously published values is only 2 meV.

We also evaluated the Fan-Migdal self-energy without adopting the AHC approximation and thus considering so called non-adiabatic terms, by including phonon frequencies in the denominator of Eq. (4.13). We emphasize that in our approach, which does not require summations over empty bands, the inclusion of non-adiabatic effects comes at no extra computational cost, as does the evaluation of electron-phonon self energies at multiple temperatures and frequencies. We found that the ZPR of the indirect band gap of diamond computed by including non-adiabatic effects is -332 meV, in good agreement with the value -327 meV reported in Ref. 109, where the LDA functional and $10 \times 10 \times 10$ **k**-point sampling were used, as in our work.

We close the discussion of our DFT results by presenting temperature-dependent renormalizations of both the direct and indirect gaps in diamond obtained with $4 \times 4 \times 4$ **q**-point sampling (Fig. (4.4)). We carried out the calculations with the LDA functional at the LDA lattice constant obtained in Ref.6, and with the PBE functional and the optimized lattice constant at the PBE level of theory. We find an almost identical temperature dependence with the two functionals. Our results for the direct gap renormalization compare well with those of Ref. 94 and 68; however, they differ from those of Ref. 6. As for the indirect gap, our results agree well with the findings of Ref. 68.

In collaboration with Dr. Arpan Kundu,[72] we compared the AHC formalism results with those obtained from path-integral molecular dynamics (PIMD)[26] and frozen-phonon approach. Although the rigid-ion approximation is used in the AHC formalism, the difference between AHC formalism and frozen-phonon approach or PIMD is negligible in crystal diamond. The rigid-ion approximation is valid for temperatures lower than 500 K, however we find larger differences at higher temperature.

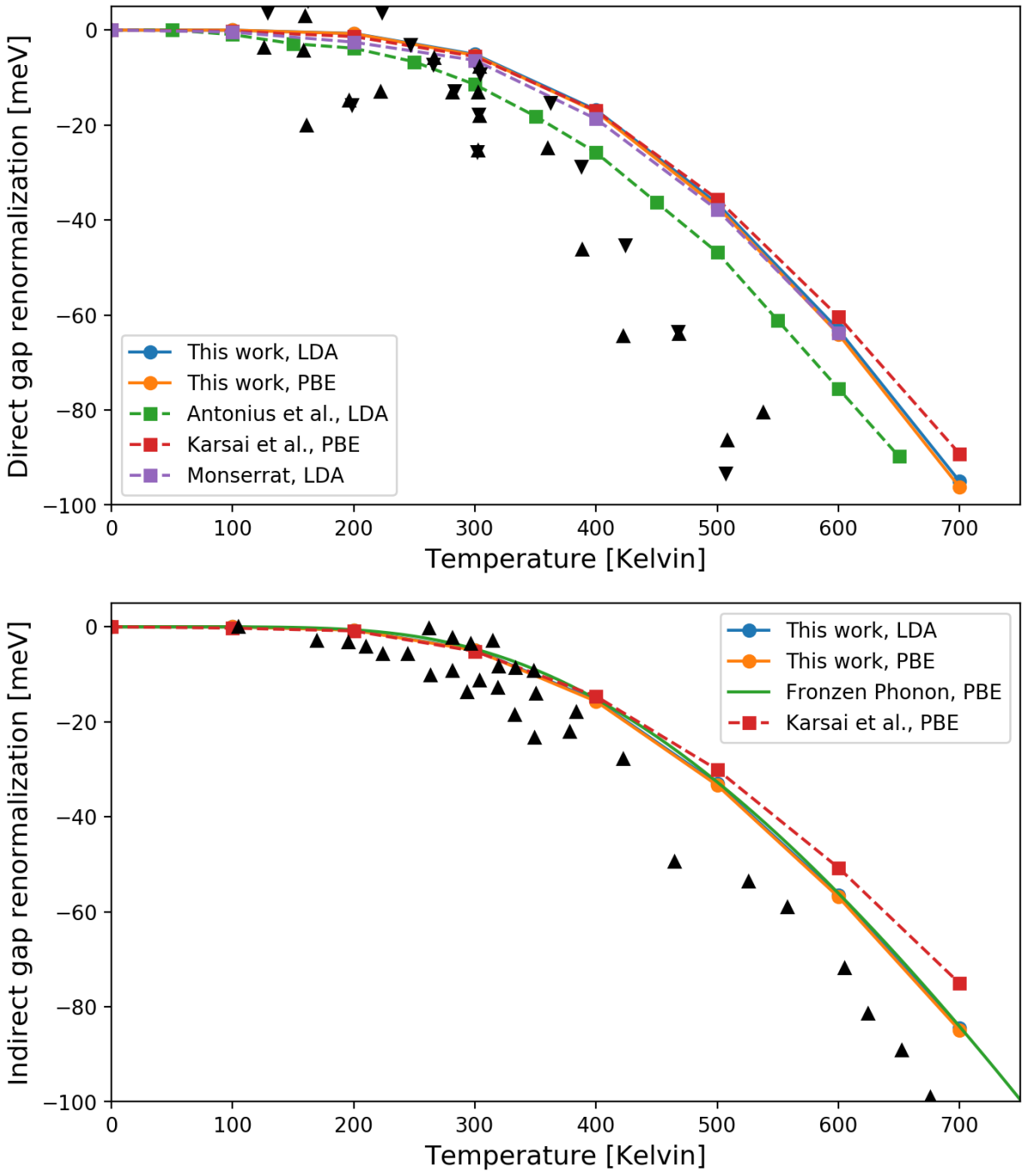

Figure 4.4: Temperature dependence of direct (upper) and indirect (lower) band gap in diamond. The renormalization at zero temperature was set at zero. The literature calculations are Ref. 6, Ref. 68 and Ref. 94, and the experimental renormalizations (black triangles) of direct and indirect gap are extracted from Ref. 81 and Ref. 101, respectively.

Zero point renormalization of energy levels at the G_0W_0 level of theory – We conducted a detailed study of the zero point renormalization of the direct gap of diamond at the level of G_0W_0, using different numerical protocols, denoted P1 – P5 in Table 4.3.

The G_0W_0 self-energy Σ contains an exchange term

$$\Sigma_x(\mathbf{r},\mathbf{r}') = -\sum_{n=1}^{N_{\rm occ}}\sum_{\mathbf{k}} \psi_{n\mathbf{k}}(\mathbf{r}) v_c(\mathbf{r},\mathbf{r}') \psi^*_{n\mathbf{k}}(\mathbf{r}') \tag{4.28}$$

and a correlation term

$$\Sigma_c(\mathbf{r},\mathbf{r}';\omega) = i\int_{-\infty}^{+\infty} \frac{\mathrm{d}\omega'}{2\pi} G_{\rm KS}(\mathbf{r},\mathbf{r}';\omega+\omega') W_p(\mathbf{r},\mathbf{r}';\omega'), \tag{4.29}$$

where $\psi_{n\mathbf{k}}$ are Kohn-Sham orbitals associated with the n-th level at the $\mathbf{k}$ point, v_c is the bare Coulomb potential, $G_{\rm KS}$ is the Green function written in terms of Kohn-Sham orbitals,

$$G_{\rm KS}(\mathbf{r},\mathbf{r}',\omega) = \sum_{n\mathbf{k}} \frac{\psi_{n\mathbf{k}}(\mathbf{r})\psi^*_{n\mathbf{k}}(\mathbf{r}')}{\omega-\varepsilon_{n\mathbf{k}}} \tag{4.30}$$

with $\varepsilon_{n\mathbf{k}}$ being the n-th Kohn-Sham energy at the $\mathbf{k}$ point, and W_p is the difference between the screened Coulomb potential and bare Coulomb potential,

$$W_p(\mathbf{r},\mathbf{r}';\omega) = W(\mathbf{r},\mathbf{r}';\omega) - v_c(\mathbf{r},\mathbf{r}'). \tag{4.31}$$

To improve the convergence of the calculations of the exchange part Σ_x with respect to the number of $\mathbf{k}$ points, the curvature technique developed by Gygi-Baldereschi[56] and further refined by Ref. 97 was used in most of our calculations. In Table 4.3, the curvature technique is used to obtain the results presented in P1 and P2, but not those of P3 – P5.

The screened Coulomb interaction W is evaluated by computing the dielectric matrix ϵ,

$$W(\mathbf{r},\mathbf{r}';\omega) = \epsilon^{-1}(\mathbf{r},\mathbf{r}';\omega) v_c(\mathbf{r},\mathbf{r}'). \tag{4.32}$$

and the symmetrized dielectric matrix $\tilde{\epsilon}$ is computed from the symmetrized polarizibility $\tilde{\chi}^0$,

$$\tilde{\epsilon}_{\mathbf{G}\mathbf{G}'}(\mathbf{q},\omega) = \delta_{\mathbf{G}\mathbf{G}'} - \tilde{\chi}^0_{\mathbf{G}\mathbf{G}'}(\mathbf{q},\omega). \tag{4.33}$$

The symmetrized polarizibility can be written as:

$$\begin{aligned}\tilde{\chi}^0_{\mathbf{G}\mathbf{G}'}(\mathbf{q};\omega) = &-4\pi e^2 \sum_{n}^{N_{\text{occ}}} \sum_{m=N_{\text{occ}}+1}^{+\infty} \sum_{\mathbf{k}} \frac{\rho^*_{mn\mathbf{k}}(\mathbf{q},\mathbf{G})\rho_{jmn\mathbf{k}}(\mathbf{q},\mathbf{G}')}{|\mathbf{q}+\mathbf{G}||\mathbf{q}+\mathbf{G}'|} \\ &\times \left[\frac{1}{\varepsilon_{m\mathbf{k}} - \varepsilon_{n\mathbf{k}-\mathbf{q}} + \omega - i0^+} + \frac{1}{\varepsilon_{m\mathbf{k}} - \varepsilon_{n\mathbf{k}-\mathbf{q}} - \omega - i0^+}\right]\end{aligned} \tag{4.34}$$

with

$$\rho_{mn\mathbf{k}}(\mathbf{q},\mathbf{G}) = \left\langle \psi_{m\mathbf{k}} \left| \mathbf{e}^{i(\mathbf{q}+\mathbf{G})\cdot\mathbf{r}} \right| \psi_{n\mathbf{k}-\mathbf{q}} \right\rangle. \tag{4.35}$$

The straightforward evaluation of the polarizibility $\tilde{\chi}^0$ is expensive because it requires the summation over empty bands and it is frequency dependent. In Table 4.3, the calculations presented in the last column used 100 states for the summation over empty bands. To compare our results with those if the literature, we also used 100 states for the results given in columns P2 – P5. By using the Lanczos algorithm, we can avoid the summation over empty bands and there is no need to truncate the summation. For the results of the P1 column, only 8 bands are used, and we show that the Lanczos algorithm yields the same result as that of the P2 column, where 100 bands are used.

In Table 4.3, the calculation shown in the last column used the Plasmon-Pole model (PPM),[66] a semi-empirical model, to compute the frequency dependence of the dielectric matrix, but our G_0W_0 calculation computes the full frequency (FF) dependence using the Lanczos approach without using any semi-empirical approximations. To compare our results with those existing in the literature, we used the PPM in column P5 and we did reproduce the literature result. However, FF is known to be more accurate than the PPM,[47] thus we used FF in obtaining the results of P1 – P4.

The calculation of electron-phonon self-eneriges also requires to carry out summations over empty bands, and we used the Lanczos technique for the electron-phonon self-energies in column P1 – P5.

We note that in our electron-phonon calculations at the G_0W_0 level, we apply G_0W_0 corrections only to DFT energy levels and we compute the electron-phonon coupling matrix elements at the DFT level. Our fully-converged result is $-545\,\mathrm{meV}$ (P1 in Table 4.3), which is smaller than the value reported in Ref. 6. We investigated the dependence of the results on N_{states}, the number of states used in the evaluation of the G_0W_0 self-energy; on whether the Lanczos approach was used in the evaluation of G_0W_0 and electron-phonon self-energies; and on whether a full-frequency (FF) integration or the Hybersten-Louie plasmon-pole model (PPM) was used in the evaluation of the G_0W_0 self-energy. The G_0W_0 calculation with the PPM was carried out with the `ABINIT` package.[48, 20] In addition, we used the curvature technique proposed in Ref. 97 in the calculation of the exchange part of the G_0W_0 self-energy.

In Table 4.3, P1 and P2 both yield what we consider a converged value of the ZPR $-545\,\mathrm{meV}$, obtained by using 8 bands (4 valence bands and 4 conduction bands) and 100 bands (4 valence bands and 96 conduction bands), respectively. In P3, the curvature correction was not adopted when computing the exchange part of the electron self-energies and the computed ZPR, $-562\,\mathrm{meV}$, was about 20 meV lower than our converged value. In P4, where the Lanczos approach was not adopted, we obtained an even lower value, $-600\,\mathrm{meV}$. For P1 – P4, the G_0W_0 quasiparticle energies were obtained with the `WEST` code[51] with full-frequency (FF) integration. Finally in P5 we used the G_0W_0 band structure obtained with the plasmon-pole model (PPM) computed with the `ABINIT` package, as input for our calculations. By doing so we obtain a ZPR of $-620\,\mathrm{meV}$, in good agreement with the result $-622\,\mathrm{meV}$ reported in Ref.6.

This comparison shows that the accuracy of G_0W_0 corrections to DFT eigenvalues has a significant impact on the computed electron-phonon self-energies; the comparison also shows

that the plasmon-pole model may not be sufficiently accurate even for a simple crystal such as diamond.

Table 4.3: Zero point renormalization (ZPR) of the direct gap of diamond obtained with different computational protocols (P) at the level of G_0W_0@LDA. N_{states} denotes the number of empty bands used in the evaluation of the G_0W_0 self-energy; Lanczos the algorithm used for the frequency integration; FF and PPM stand for full frequency and plasmon pole model, respectively. In the last row we indicate whether the curvature technique of Ref. 97 was included in the calculation of the exact exchange term of the self-energy.

	P1	**P2**	**P3**	**P4**	**P5**	**Ref. 6**
ZPR [meV]	-545	-545	-562	-600	-620	-622
N_{states} ($\Sigma_{G_0W_0}$)	8	100	100	100	100	100
Lanczos ($\Sigma_{G_0W_0}$)	Yes	Yes	Yes	No	No	No
Lanczos (Σ_{ep})	Yes	Yes	Yes	Yes	Yes	See text
Freq. integration	FF	FF	FF	FF	PPM	PPM
Curvature	Yes	Yes	No	No	No	N/A

4.4 Large scale calculations: zero point renormalization in defective solids

After verifying our implementation and examining the effect of various numerical approximations, we carried out calculations for supercells representative of defective solids, in particular defects in diamond (see Figure 4.5), showcasing the ability of the methodology developed here to carry out calculations for large systems. We considered two nearest neighbor carbon atoms replaced by either two boron or two nitrogen atoms. The electronic structure of the boron (nitrogen) pair exhibits one unoccupied (occupied) state in the band gap of the host. We carried out DFT calculations with the PBE functional[103], SG15[123] ONCV[57] pseudopotentials and an energy cutoff of 50 Ry. The G_0W_0 calculations were carried out with the `WEST` code. We report the electron-phonon renormalizations of the systems with defects in Table 4.4 and Table 4.5.

We first discuss the results using the AHC approximation (Table 4.4 and Table 4.5). The

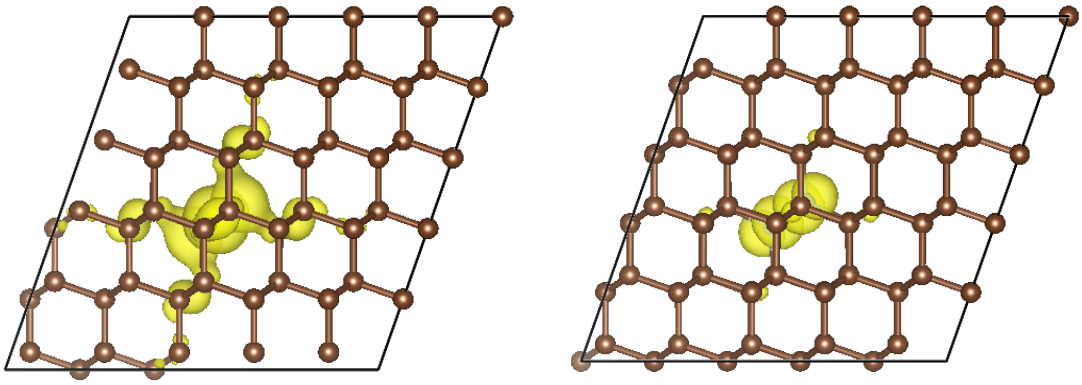

Figure 4.5: Isosurface (yellow) of the square moduli of the single particle orbitals of the boron pair unoccupied defect state (left) and nitrogen pair occupied defect state (right), as obtained in a $5 \times 5 \times 5$ supercell of diamond.

presence of defects affects the renormalizaton of the gap of the host crystal due to symmetry breaking,[72] with the effect decreasing in magnitude as the size of supercell increases, as expected. In order to find a converged value of the renormalization, we extrapolated our computed values as a function of the inverse of the supercell size for defective systems, and as a function of the inverse of the number of $\mathbf{q}$-points for pristine diamond. Our extrapolated values at the PBE level are -340 meV for the gap of pristine diamond and -338 and -370 meV for that of diamond with boron and nitrogen pairs, respectively. Once we add G_0W_0 corrections, the corresponding extrapolated values are -351 meV and -372 and -386 meV. In all cases, within the AHC approximations, we do not find significant differences between the renormalizations of the gap of pristine and defective diamond.

The renormalization of the defect state within the band gap is more interesting, as the renormalizations of the defect states arising from boron and nitrogen pairs are noticeably distinct, 51 meV and -7 meV, respectively, at the PBE level, after extrapolation. When adding G_0W_0 corrections, the extrapolated values are 40 meV and 1 meV.

Table 4.4: Zero point renormalization (ZPR) [meV] of the energy gap of pristine diamond evaluated with k-point sampling (last column), of the energy gap of a supercell of diamond hosting a boron defect (Host), and of the state of a boron impurity in a supercell of diamond (Defect).

	Supercell	ZPR (Defect)	ZPR (Host)	ZPR (Pristine)
Adiabatic DFT/PBE	$3 \times 3 \times 3$	36	-397	-277
	$4 \times 4 \times 4$	46	-401	-366
	$5 \times 5 \times 5$	47	-327	-316
	$6 \times 6 \times 6$	–	–	-324
	$8 \times 8 \times 8$	–	–	-330
	$10 \times 10 \times 10$	–	–	-341
	extrapolated	51[a]	-338[a]	-357;[a] -340[b]
Adiabatic G_0W_0@PBE	$3 \times 3 \times 3$	29	-416	-254
	$4 \times 4 \times 4$	37	-448	-380
	$5 \times 5 \times 5$	37	-346	-291
	extrapolated	40[a]	-372[a]	-351[a]
Non-adiabatic DFT/PBE	$3 \times 3 \times 3$	-267	-556	-637
	$4 \times 4 \times 4$	-152	-482	-510
	$5 \times 5 \times 5$	-131	-362	-372
	$6 \times 6 \times 6$	–	–	-353
	$8 \times 8 \times 8$	–	–	-330
	$10 \times 10 \times 10$	–	–	-329
	extrapolated	-86[a]	-346[a]	-338;[a] -320[b]
Non-adiabatic G_0W_0@PBE	$3 \times 3 \times 3$	-275	-574	-615
	$4 \times 4 \times 4$	-163	-518	-508
	$5 \times 5 \times 5$	-143	-379	-348
	extrapolated	-99[a]	-373[a]	-325[a]

[a] Extrapolated up to $5 \times 5 \times 5$
[b] Extrapolated up to $10 \times 10 \times 10$

Table 4.5: Zero point renormalization (ZPR) [meV] of the energy gap of pristine diamond evaluated with k-point sampling (last column), of the energy gap of a supercell of diamond hosting a nitrogen defect (Host), and of the state of a nitrogen impurity in a supercell of diamond (Defect).

	Supercell	ZPR (Defect)	ZPR (Host)	ZPR (Pristine)
Adiabatic DFT/PBE	$3 \times 3 \times 3$	22	-322	-277
	$4 \times 4 \times 4$	3	-394	-366
	$5 \times 5 \times 5$	1	-333	-316
	$6 \times 6 \times 6$	–	–	-324
	$8 \times 8 \times 8$	–	–	-330
	$10 \times 10 \times 10$	–	–	-341
	extrapolated	-7[a]	-370[a]	-357[a], -340[b]
Adiabatic G_0W_0@PBE	$3 \times 3 \times 3$	33	-339	-254
	$4 \times 4 \times 4$	12	-415	-380
	$5 \times 5 \times 5$	9	-346	-291
	extrapolated	1[a]	-386[a]	-351[a]
Non-adiabatic DFT/PBE	$3 \times 3 \times 3$	185	-459	-637
	$4 \times 4 \times 4$	156	-431	-510
	$5 \times 5 \times 5$	149	-345	-372
	$6 \times 6 \times 6$	–	–	-353
	$8 \times 8 \times 8$	–	–	-330
	$10 \times 10 \times 10$	–	–	-329
	extrapolated	138[a]	-344[a]	-338[a], -320[b]
Non-adiabatic G_0W_0@PBE	$3 \times 3 \times 3$	192	-473	-615
	$4 \times 4 \times 4$	161	-452	-508
	$5 \times 5 \times 5$	153	-359	-348
	extrapolated	141[a]	-362[a]	-325[a]

[a] Extrapolated up to $5 \times 5 \times 5$
[b] Extrapolated up to $10 \times 10 \times 10$

We now turn to discuss non-adiabatic effects. We found that including non-adiabatic effects in Eq. (4.13) changes substantially the renormalizations computed for defect states in diamond, although it has a smaller effect on the gap of diamond. Our results are reported in Table 4.4 and Table 4.5. The gap of diamond varies by -56, -35 and -12 meV – when including non-adiabatic effect – in the case of the pristine solid, boron and nitrogen defective systems, respectively, at the PBE level in the $5 \times 5 \times 5$ supercell. The magnitude of the renormalization of defect states increases by approximately a factor of 3 for boron pairs and by more than a factor of 10 for nitrogen in $5 \times 5 \times 5$ supercell, when including non-adiabatic effects. After extrapolation, the renormalization of the boron defect state is -86 meV (PBE) and -99 meV (G_0W_0) and that of the nitrogen pair is 138 meV (PBE) and 141 meV (G_0W_0).

To understand the difference between the results obtained with and without non-adiabatic effects, we plot in Figure 4.6 the contribution of each vibrational mode to the difference between the adiabatic and non-adiabatic renormalizations for the boron pair, described with a $5 \times 5 \times 5$ supercell; such difference is expressed in terms of the fractional contribution of defect atoms to each mode, $f_{\mathbf{q}\nu}^{\text{defect}} = \sum_I^{\text{defect}} \sum_\alpha |\xi_{I\alpha,\mathbf{q}\nu}|^2$, where the summation runs over the boron atoms. We define vibrational modes with $f_{\mathbf{q}\nu}^{\text{defect}} > 10\%$ as modes exhibiting defect relevant vibrations. Figure 4.6 shows that defect relevant vibrations are indeed responsible for the difference between adiabatic and non-adiabatic effects found in the case of defect states; however their contribution to the host gap renormalization are small. Quantitatively, the defect relevant vibrations contribute approximately -89 meV to the difference between adiabatic and non-adiabatic defect state renormalizations, with the remaining -88 meV being accounted for by coupling with lattice vibrations. Overall our results indicate that the AHC formalism and related adiabatic approximation are not sufficiently accurate to describe the electron-phonon renormalizations of carbon-based defect states, and that taking into account non-adiabatic effects is critical to obtain accurate results.

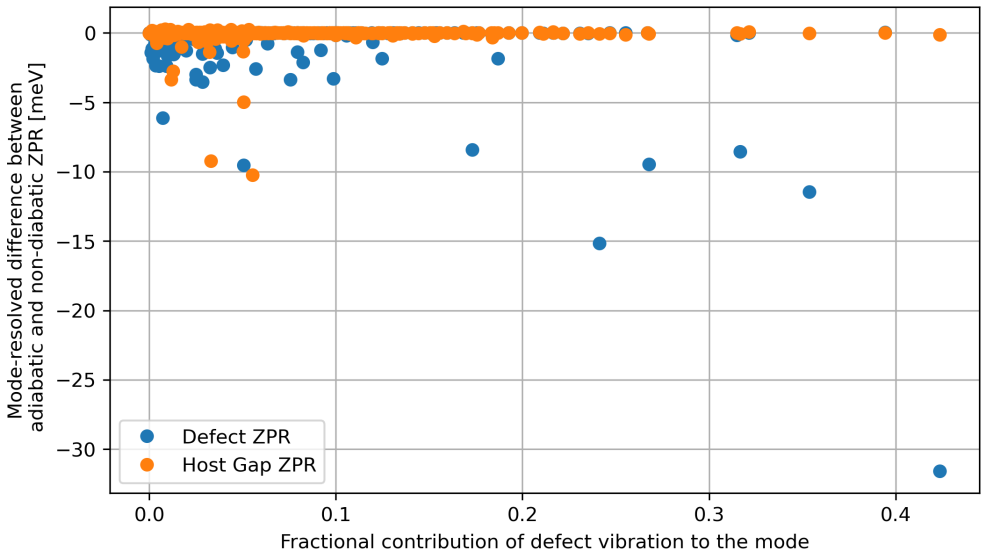

Figure 4.6: The contribution of vibration modes to the difference between adiabatic and non-adiabatic renormalizations for a boron pair in diamond, described in a $5 \times 5 \times 5$ supercell, with respect to the fractional contribution of the vibration of defect atoms $f_{\mathbf{q}\nu}^{\text{defect}}$ (see text).

4.5 Conclusions

In summary, we presented an efficient, combined approach to compute electron-electron and electron-phonon self-energies in solids, which can be used for large scale calculations, and enables the inclusion of non-adiabatic and temperature effects in a simple, straightforward manner, at no extra computational cost. This approach is a generalization to solid of the method proposed for molecules in Ref. 92. We discussed in detail verification and validation strategies for calculations at the DFT and G_0W_0 level of theory; we found that the numerical accuracy of G_0W_0 band structures is critical to obtain robust predictions of zero point renormalizations of energy levels and that carrying out full frequency integration is necessary to reach the required accuracy. We presented calculations for pristine diamond and defects in diamonds with supercells containing ~ 1000 electrons; we found that while the inclusion of non-adiabatic effects leads to moderate changes in the renormalization of the diamond band gap, it is essential to obtain accurate results for defect levels in the gap. Work is in progress to apply our methodology to the study of spin-defects in diamond and in other

insulators and semiconductors, including spin-phonon interaction.

CHAPTER 5

ELECTRON-PHONON INTERACTION USING HYBRID FUNCTIONALS

As briefly discussed in Section 2.7, density matrix perturbation theory and the Liouville equation can be used to compute the change of charge density due to atomic displacements. In this chapter, we describe the implementation of density matrix perturbation theory to compute phonon frequencies and electron-phonon interactions at the level of hybrid functionals.

5.1 Introduction

In the previous chapter, we implemented a method to combine the computation of electron-electron interactions at the G_0W_0 level of the theory and the computation of electron-phonon interactions by writing the dielectric functions in terms of dielectric eigenpotentials.[143]

The Green's functions used in G_0W_0 calculations are constructed from density functional theory (DFT) energy levels ε and wavefunctions ψ, thus the G_0W_0 quasiparticle energies depend on the choice of the DFT exchange-correlation functional. Figure 5.1 shows the G_0W_0 HOMO energy levels of the H_2O molecule starting from Hartree-Fock (HF), PBE, and hybrid functionals with various fraction of exact exchange (EX), as well as a comparison to self-consistent GW calculations (scGW) and experimental results. The different starting points may lead to a variation of the computed G_0W_0 energy levels that are as large as $\sim 1\,\text{eV}$, and the use of hybrid functionals in general improves the comparison between self-consistent GW calculations and experiments. The electron-phonon interactions also depend on the chosen starting-point to compute the electronic structure of the system. In Section 4.3, we compared the electron-phonon renormalizations of the energy levels of diamond obtained with different G_0W_0 approximations; we show that the chosen numerical approximations

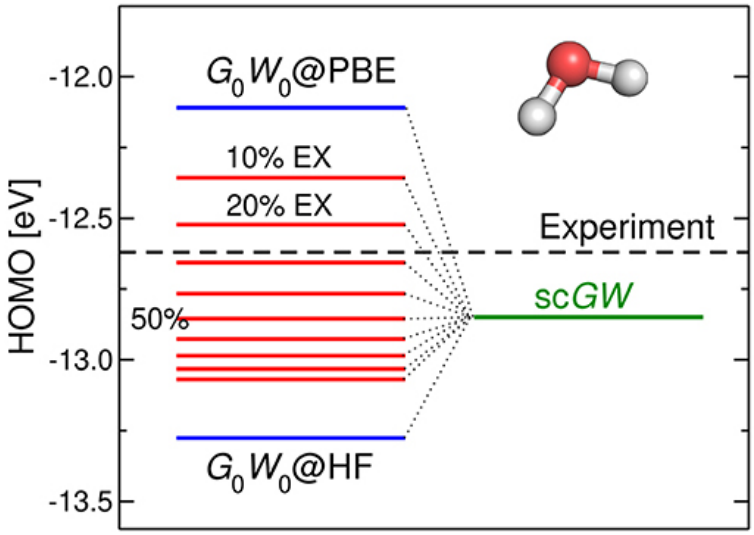

Figure 5.1: The HOMO energy level of the water molecule computed with the G_0W_0 approximation and using different DFT energies and wavefunctions as starting points, including DFT calculations at the PBE and Hartree-Fock (HF) level of theory and with hybrid functionals with various portions of exact exchange (EX). The value obtained with self-consistent GW calculations is indicated in green. Credit: Golze D, Dvorak M and Rinke P (2019). *The GW Compendium: A Practical Guide to Theoretical Photoemission Spectroscopy.* Front. Chem. 7:377. doi: 10.3389/fchem.2019.00377. Permission granted under the Creative Commons Attribution (CC BY) licence, version 4.0.

may result in 80 meV differences. These observations indicate that the quality of the band structure and single particple wavefunction does make a difference in the computation of electron-phonon interactions. In addition, we note that the method employed in Chapter 4 only makes corrections to the DFT energy levels, but the electron-phonon coupling matrices are not corrected and only computed at the DFT level. In this thesis we evaluate electron-electron and electron-phonon interactions at the level of hybrid functionals, where both the energy levels and electron-phonon coupling matrices are computed at the same level of theory.

Existing methods such as the frozen-phonon (FPH) approach[6, 24], first-principles molecular dynamics (FPMD)[96, 94, 68, 72] and path-integral molecular dynamics (PIMD)[72, 26] can *in principle* be used to compute phonons or electron-phonon self-energies at the hybrid level of theory, but such calculations are computationally very demanding. This is due to the

necessity of using large supercells which makes these methods difficult to scale as a function of size and thus applicable to large systems. Thus, a scalable and affordable implementation of hybrid level phonon and electron-phonon calculations is desirable.

As an alternative to the solution of the Sternheimer equation[132], density matrix perturbation theory (DMPT) was adopted to compute excitation energies and absorption spectra in molecules and solids in conjunction with time-dependent density functional theory (TDDFT)[115, 117], and was later implemented to solve the Bethe-Salpeter equation (BSE)[118, 119, 116, 99]. In the latter case, the DMPT was applied to find the change of wavefunctions due to the perturbation of an electric field in molecules or solids. However, as a general formalism, the DMPT can be used to compute the response of a system to perturbations of any form, including the atomic displacements in the case of phonon calculations.

In this chapter, we first derive the DMPT formalism for phonon calculations starting from the quantum Liouville-von Neumann's equation in Section 5.2; we then verify the method by comparing the results with the FPH and PIMD methods in Section 5.3; we conclude this chapter in Section 5.4 with our summay and conclusions.

5.2 Methodology

We start with the quantum Liouville's equation, and within Kohn-Sham density functional theory,

$$i\frac{\mathrm{d}}{\mathrm{d}t}\gamma(t) = [H^{\mathrm{KS}}(t), \gamma(t)], \tag{5.1}$$

where $[\cdot,\cdot]$ is the anti-commutator, $H^{\mathrm{KS}}(t)$ is the Kohn-Sham Hamiltonian and γ is the density matrix that can be written in terms of Kohn-Sham single-particle orbitals

$$\gamma(\mathbf{r},\mathbf{r}',t) = 2\sum_{n}^{N_{\mathrm{occ}}} \psi_n(\mathbf{r},t)\psi_n^*(\mathbf{r}',t), \tag{5.2}$$

where the prefactor 2 accounts for spin. In the following discussion, we dropped the indices $\mathbf{k}$ and $\mathbf{q}$ used for sampling of the Brillouin zone for convenience.

Given a perturbation ∂V_{ext} to the Hamiltonian, the change of the density matrix $\partial\gamma$ satisfies the following equation,

$$i\frac{\mathrm{d}}{\mathrm{d}t}\partial\gamma(t) = \mathcal{L}\cdot\partial\gamma(t) + [\partial V_{\text{ext}}, \gamma], \tag{5.3}$$

where $\mathcal{L}$ is the Liouville super-operator,

$$\mathcal{L}\cdot\partial\gamma(t) = [H^{\text{KS}}(t), \partial\gamma] + [\partial V_{\text{H}}[\partial\gamma](t), \gamma] + [\partial V_{\text{xc}}[\partial\gamma](t), \gamma]. \tag{5.4}$$

For simplicity, we use the notation ∂ to represent the change of potentials ∂V, wavefunctions $\partial\psi$, charge densities $\partial n(\mathbf{r})$ and density matrices $\partial\gamma(\mathbf{r}, \mathbf{r}')$. Later in the discussion, we also use the notation $\partial_{I\alpha}$ ($\partial_{J\beta}$) to represent a change due to the displacement of atom I (J) along the direction α (β).

Taking the Fourier transform of the time-dependent Eq. (5.3), we rewrite it in the frequency domain,

$$(\omega - \mathcal{L})\cdot\partial\gamma(\omega) = [\partial V_{\text{ext}}(\omega), \gamma]. \tag{5.5}$$

In phonon calculations, the Born-Oppenheimer approximation[16] is applied and no retardation effects are included. Hence we only need to solve the equation at $\omega = 0$,

$$\mathcal{L}\cdot\partial\gamma = -[\partial V_{\text{ext}}, \gamma]. \tag{5.6}$$

The equation can be expressed as,

$$\begin{bmatrix} \mathcal{D}+\mathcal{K}^{1e}-\mathcal{K}^{1d} & \mathcal{K}^{2e}-\mathcal{K}^{2d} \\ -\mathcal{K}^{2e}+\mathcal{K}^{2d} & -\mathcal{D}-\mathcal{K}^{1e}+\mathcal{K}^{1d} \end{bmatrix} \begin{bmatrix} \mathcal{A} \\ \mathcal{B} \end{bmatrix} = \begin{bmatrix} \{|-\mathcal{P}^c \partial V_{\text{ext}} \psi_n\rangle : n=1,\cdots,N_{\text{occ}}\} \\ \{|\ \ \mathcal{P}^c \partial V_{\text{ext}} \psi_n\rangle : n=1,\cdots,N_{\text{occ}}\} \end{bmatrix} \tag{5.7}$$

where $\mathcal{P}^c$ is the projection operator onto the virtual bands manifold, and the solutions $\mathcal{A}$ and $\mathcal{B}$ are collections of change of wavefunctions a_n and b_n, $n=1,\cdots,N_{\text{occ}}$, that can be used to evaluate the change of density matrices,

$$\partial\gamma = 2\sum_{n}^{N_{\text{occ}}} |a_n\rangle\langle\psi_n| + |\psi_n\rangle\langle b_n| \tag{5.8}$$

In phonon calculations with $\omega=0$, we have $a_n = b_n = \partial\psi_n$ and thus we write Eq. (5.7) as:

$$\left[\mathcal{D}+\mathcal{K}^{1e}-\mathcal{K}^{1d}+\mathcal{K}^{2e}-\mathcal{K}^{2d}\right]\mathcal{A} = \{|-\mathcal{P}^c\partial V_{\text{ext}}\psi_n\rangle : n=1,\cdots,N_{\text{occ}}\}, \tag{5.9}$$

and this is a generalized Sternheimer equation, where the operators are defined below.

$$\mathcal{D}\mathcal{A} = \left\{\mathcal{P}^c(H^{\text{KS}}-\varepsilon_n)|a_n\rangle : n=1,\cdots,N_{\text{occ}}\right\}. \tag{5.10}$$

When using LDA/GGA functionals, the K^{1e} and K^{2e} operators are defined as,

$$\mathcal{K}^{1e}\mathcal{A} = \left\{2\int \mathrm{d}\mathbf{r}'\mathcal{P}^c(\mathbf{r},\mathbf{r}')\psi_n(\mathbf{r}')\sum_{n'}^{N_{\text{occ}}}\int \mathrm{d}\mathbf{r}'' f_{\text{Hxc}}(\mathbf{r}',\mathbf{r}'')\psi^*_{n'}(\mathbf{r}'')a_{n'}(\mathbf{r}'') : n=1,\cdots,N_{\text{occ}}\right\}, \tag{5.11}$$

$$\mathcal{K}^{2e}\mathcal{A} = \left\{2\int \mathrm{d}\mathbf{r}'\mathcal{P}^c(\mathbf{r},\mathbf{r}')\psi_n(\mathbf{r}')\sum_{n'}^{N_{\text{occ}}}\int \mathrm{d}\mathbf{r}'' f_{\text{Hxc}}(\mathbf{r}',\mathbf{r}'')a^*_{n'}(\mathbf{r}'')\psi_{n'}(\mathbf{r}'') : n=1,\cdots,N_{\text{occ}}\right\}, \tag{5.12}$$

where $f_{\text{Hxc}} = v_{\text{c}} + f_{\text{xc}}$ is the sum of the bare Coulomb potential v_c and the exchange-correlation kernel f_{xc}. $\mathcal{K}^{1d}$ and the $\mathcal{K}^{2d}$ operators are zero for LDA/GGA functionals.

When using hybrid functionals, the operators are defined as,

$$\mathcal{K}^{1e}\mathcal{A} = \left\{ 2 \int \mathrm{d}\mathbf{r}' \mathcal{P}^c(\mathbf{r}, \mathbf{r}') \psi_n(\mathbf{r}') \sum_{n'}^{N_{\text{occ}}} \int \mathrm{d}\mathbf{r}'' f_{\text{Hxc}}^{\text{loc}}(\mathbf{r}', \mathbf{r}'') \psi_{n'}^*(\mathbf{r}'') a_{n'}(\mathbf{r}'') : n = 1, \cdots, N_{\text{occ}} \right\}, \tag{5.13}$$

$$\mathcal{K}^{2e}\mathcal{A} = \left\{ 2 \int \mathrm{d}\mathbf{r}' \mathcal{P}^c(\mathbf{r}, \mathbf{r}') \psi_n(\mathbf{r}') \sum_{n'}^{N_{\text{occ}}} \int \mathrm{d}\mathbf{r}'' f_{\text{Hxc}}^{\text{loc}}(\mathbf{r}', \mathbf{r}'') a_{n'}^*(\mathbf{r}'') \psi_{v'}(\mathbf{r}'') : n = 1, \cdots, N_{\text{occ}} \right\}, \tag{5.14}$$

$$\mathcal{K}^{1d}\mathcal{A} = \left\{ \alpha \int \mathrm{d}\mathbf{r}' \mathcal{P}^c(\mathbf{r}, \mathbf{r}') \sum_{n'}^{N_{\text{occ}}} a_{n'}(\mathbf{r}') \int \mathrm{d}\mathbf{r}'' v_c(\mathbf{r}', \mathbf{r}'') \psi_{n'}^*(\mathbf{r}'') \psi_n(\mathbf{r}'') : n = 1, \cdots, N_{\text{occ}} \right\} \tag{5.15}$$

$$\mathcal{K}^{2d}\mathcal{A} = \left\{ \alpha \int \mathrm{d}\mathbf{r}' \mathcal{P}^c(\mathbf{r}, \mathbf{r}') \sum_{n'}^{N_{\text{occ}}} \psi_{n'}(\mathbf{r}') \int \mathrm{d}\mathbf{r}'' v_c(\mathbf{r}', \mathbf{r}'') a_{n'}^*(\mathbf{r}'') \psi_n(\mathbf{r}'') : n = 1, \cdots, N_{\text{occ}} \right\} \tag{5.16}$$

where $f_{\text{Hxc}}^{\text{loc}} = v_c + f_{\text{xc}}^{\text{loc}}$ is the sum of the bare Coulomb potential and the local part of the exchange-correlation kernel $f_{\text{xc}}^{\text{loc}}$ and the parameter α is the fraction of the Hartree-Fock exchange included in the hybrid functional.

Once we have the the solutions a_n of the Liouville equation (Eq. (5.7) or Eq. (5.9)), i.e., the change of wavefunction $\partial\psi_n$, we can compute the change of the density matrix with Eq. (5.8), the change of density with

$$\partial n(\mathbf{r}) = 2 \sum_{n}^{N_{\text{occ}}} \partial\psi_n^*(\mathbf{r}) \psi_n(\mathbf{r}) + \psi_n^*(\mathbf{r}) \partial\psi_n(\mathbf{r}) \tag{5.17}$$

and force constants

$$C_{I\alpha,J\beta} \propto \left\langle \partial_{I\alpha}\psi_n \left| \partial_{J\beta} V_{\text{ext}} \right| \psi_n \right\rangle . \tag{5.18}$$

By diagonalizing the dynamics matrix,

$$\sum_{J\beta} \frac{1}{\sqrt{M_I M_J}} C_{I\alpha,J\beta}\xi_{J\beta,\nu} = \omega_\nu^2 \xi_{I\alpha,\nu}, \tag{5.19}$$

where M_I, M_J are atomic masses, we obtain the frequency ω_ν of mode ν and the polarization of the mode $\xi_{I\alpha,\nu}$.

To compute the electron-phonon coupling matrices in Cartesian basis:

$$g_{mnI\alpha} = \langle \psi_m \left| \partial_{I\alpha} V_{\text{scf}} \right| \psi_n \rangle \tag{5.20}$$

or in phonon mode basis:

$$g_{mn\nu} = \sum_{I\alpha} \frac{\xi_{I\alpha,\nu}}{\sqrt{M_I}} g_{mnI\alpha}, \tag{5.21}$$

where $\xi_{I\alpha,\nu}$ is the ν-th vibrational mode, the change of the self-consistent (scf) potential ∂V_{scf} needs to be evaluated. The scf potential consists of the Hartree potential V_{H}, the local part of the exchange-correlation potential $V_{\text{xc}}^{\text{loc}}$ and the non-local Hatree-Fock exchange $V_{\text{xc}}^{\text{nl}}$. Thus, the change of the scf potential $\partial V_{\text{scf}} |\psi_n\rangle$ is the sum of the three terms,

$$\partial V_{\text{H}}(\mathbf{r}) |\psi_n(\mathbf{r})\rangle = \psi_n(\mathbf{r}) \int \mathrm{d}\mathbf{r}' v_c(\mathbf{r},\mathbf{r}') \partial n(\mathbf{r}'), \tag{5.22}$$

$$\partial V_{\text{xc}}^{\text{loc}}(\mathbf{r}) |\psi_n(\mathbf{r})\rangle = \psi_n(\mathbf{r}) \int \mathrm{d}\mathbf{r}' f_{\text{Hxc}}^{\text{loc}}(\mathbf{r},\mathbf{r}') \partial n(\mathbf{r}'), \tag{5.23}$$

and

$$\partial V_{\text{xc}}^{\text{nl}} |\psi_n\rangle = -\alpha \sum_m^{N_{\text{occ}}} \int \mathrm{d}\mathbf{r}' \left[\partial\psi_m^*(\mathbf{r}')\psi_m(\mathbf{r}) + \psi_m^*(\mathbf{r}')\partial\psi_m(\mathbf{r}) \right] v_c(\mathbf{r},\mathbf{r}')\psi_n(\mathbf{r}'). \tag{5.24}$$

Once the electron-phonon coupling matrices g are obtained, the Fan-Migdal and Debye-Waller self-energies can be computed,

$$\Sigma_n^{\mathrm{FM}}(\omega, T) = \sum_{m\nu} |g_{mn\nu}|^2 \left[\frac{n_\nu + f_m}{\omega - \varepsilon_m + \omega_\nu - i0^+} + \frac{n_\nu + 1 - f_m}{\omega - \varepsilon_m - \omega_\nu - i0^+} \right] \tag{5.25}$$

$$\Sigma_n^{\mathrm{DW}}(T) = -\sum_{m\nu} \sum_{I\alpha J\beta} \frac{2n_\nu + 1}{\varepsilon_n - \varepsilon_m} \frac{1}{4\omega_\nu} \left[\frac{\xi_{I\alpha,\nu}\xi_{I\beta,\nu}}{M_I} + \frac{\xi_{J\alpha,\nu}\xi_{J\beta,\nu}}{M_J} \right] g_{mnI\alpha} g_{mnJ\beta}, \tag{5.26}$$

where n_ν is the occupation number of the frequency ω_ν obeying the Bose-Einstein distribution and f_m is the occupation number of the Kohn-Sham energy levels ε_m obeying the Fermi-Dirac distribution.

In Section 2.5, we introduced the Allen-Heine-Cardona (AHC) formalism and theories beyond the AHC listed in Table 2.1. These theories are also employed in this chapter.

We implemented the formalism above as a part of the `WEST`[51] package.

5.3 Results

5.3.1 Verification of the method

To verify the implementation of the method described above, we first computed the phonon frequencies of selected solids (diamond, silicon and silicon carbide) and the vibrational modes of selected molecules (H_2, N_2, H_2O, CO_2), and compared our results with those of the frozen phonon approach. In Table 5.1 and Table 5.2, we summarize our results for the phonon frequencies in solids and vibrational modes in molecules obtained at the PBE0 functional level of theory and computed by solving either the Liouville equation or or using the frozen phonon approach. The lattice constants used for diamond, silicon and silicon carbide are 6.8695, 10.3257 and 8.2623 Bohr, respectively, and the cell used for molecules is a cube of edge 20 Bohr. For verification purposes, we only computed the phonon modes at the Γ point in the Brillouin zone of the solids. We used an energy cutoff of 60 Ry for the solids and

Table 5.1: A comparison of selected phonon frequencies [cm^{-1}] in diamond, silicon and silicon carbide computed in a primitive cell and the PBE0 functional by solving the Liouville's equation or by using the frozen-phonon approach.

Solid	Liouville	Frozen-phonon	Absolute difference
diamond	2136.21	2131.48	4.73
silicon	737.47	737.28	0.19
silicon carbide	612.77	612.70	0.07

Table 5.2: A comparison of the vibrational modes [cm^{-1}] of selected molecules obtained with the PBE0 functional and computed by solving the Liouville's equation or by using the frozen-phonon approach.

Molecule	Symmetry	Liouville	Frozen-phonon	Absolute difference
H_2	a_1	4421.48	4438.78	17.30
N_2	a_1	2480.36	2480.36	0.00
H_2O	a_1	1652.79	1658.76	5.97
H_2O	b_2	3921.28	3936.57	15.29
H_2O	a_1	4033.68	4048.58	11.90
CO_2	e_{1u}	698.15	698.12	0.03
CO_2	a_{1g}	1375.10	1375.18	0.08
CO_2	a_{1u}	2419.08	2419.23	0.15

50 Ry for the molecules, and the SG15[123] ONCV[57] pseudopotentials for all the solids and molecules.

In Table 5.1, the absolute difference of the phonon frequencies computed with the two methods in silicon and silicon carbide are small, 0.19 and 0.07 cm^{-1}, respectively. The difference of phonon frequency in diamond is larger, but it is still below 5 cm^{-1}. In Table 5.2, we compare the vibrational frequencies of H_2, N_2, H_2O and CO_2 molecules computed by solving the Liouville equation or applying frozen-phonon approach. We found again that the differences of the vibrational modes in N_2 and CO_2 are very small (below 1 cm^{-1}), but they are larger in H_2 and H_2O. The largest difference is found in H_2 (17.30 cm^{-1}), and this is probably due to the numerical inaccuracy of the frozen-phonon approach.

To verify our approach to compute electron-phonon interactions, we computed the renormailization of the HOMO, LUMO levels and HOMO-LUMO gap in the CO_2 molecule within

Table 5.3: Electron-phonon renormalization energies [meV] of HOMO, LUMO energy levels and the HOMO-LUMO gap in the CO_2 molecule, computed by solving the Liouville's equation, using density functional perturbation theory (DFPT), the frozen-phonon (FPH) approach and the path-integral molecular dynamics (PIMD) method. We compare results obtained with different functionals: LDA, PBE, PBE0 and the B3LYP functionals, and include results obtained in Ref. 126.

Method	Functional	HOMO Renorm.	LUMO Renorm.	Gap Renorm.
Liouville	LDA	64	-453	-517
DFPT	LDA	64	-453	-517
Liouville	PBE	65	-350	-415
DFPT	PBE	65	-350	-415
FPH	PBE	53	-325	-378
Liouville	PBE0	68	-69	-137
FPH	PBE0	55	-77	-132
PIMD	PBE0	59	-103	-162
Liouville	B3LYP	67	-107	-174
FPH	B3LYP	54	-89	-143
PIMD	B3LYP	58	-112	-170
	LDA	—	—	-680.7
Literature[126]	PBE+TS	—	—	-716.2
	B3LYP	—	—	-4091.6

the Allen-Heine-Cardona (AHC) formalism, and compared the results obtained with the DFPT, FPH and/or PIMD methods. In Table 5.3, the renormailizations are computed at the LDA, PBE, PBE0 and B3LYP levels of theory, respectively. The frozen-phonon and PIMD results were obtained in collaboration with Dr. Arpan Kundu.

At the LDA and PBE level of theory, we first compared our results by solving the Liouville equation and using the density functional perturbation (DFPT) approach introduced in Chapter 4[92, 147]. At the LDA and PBE/GGA functionals, solving the Liouville equation is exactly equivalent to using the method proposed in Chapter 4, thus renormalizations obtained with the Liouville and DFPT methods are exactly the same: 64 meV for the HOMO level, −453 meV for the LUMO level, and −517 meV for the gap with the LDA functional; 65 meV for the HOMO level, −350 meV for the LUMO level, and −415 meV for the gap with the PBE functional. In addition, the renormalizations at the PBE level were also obtained with the frozen-phonon approach. In the Liouville and DFPT methods, the rigid-ion approximation is applied to obtaine the renormalized results, while it is not used in the frozen-phonon approach. Thus, the frozen-phonon results are slightly different from those of the Liouville and DFPT approaches: 53 meV for the HOMO level, −325 meV for the LUMO level, and −378 meV for the gap. We then carried out calculations with the hybrid functionals, PBE0 and B3LYP, and compared our results with those of the frozen-phonon and PIMD approaches[72]. The PIMD approach circumvents the rigid-ion approximation and also includes ionic anharmonic effects. At the PBE0 level of theory, the results computed with the Liouville equation agree better with the frozen-phonon approach, −137 meV and −132 meV for the gap renormailization, respectively. At the B3LYP level, the results computed with the Liouville equation agree very well with those of the PIMD method, −174 meV and −170 meV, respectively. At the PBE0 level of theory, the Liouville and PIMD results differ by 25 meV; at the B3LYP level, the Liouville and frozen-phonon approaches differ by 31 meV. It is worth noting that in the frozen-phonon and PIMD approaches, one does not

apply the same approximations as in the Liouville approach: the rigid-ion approximation is applied and anharmonicity is not included in the Liouville approach, thus the ~ 30 meV difference is acceptable. We also found that the computed renormalizations of the gap of CO_2 reported in literature,[126] are significantly different from ours, with differences of -680.7 and -716.2 meV with LDA[105] and PBE+TS[138] functionals, respectively. Note that the B3LYP level reported in the literature is -4091.6 meV, i.e., one order of magnitude higher than the result at the LDA and PBE+TS functional level of theory, and hence that result might be called into question for the unusual magnitude.

5.3.2 Renormalization of energy gaps in small molecules

After verifying our method, we carried out a study of the renormalization of the HOMO-LUMO gap of molecules in the G2/97 test set[29] with LDA, PBE, PBE0 and B3LYP functionals. All calculations were carried out in a cubic cell with lattice constant 20 Bohr and a planewave energy cutoff of 50 Ry. The SG15[123] ONCV[57] pseudopotentials were used for all elements. The results are summarized in Table 5.4 and Table 5.5, and are illustrated in Figure 5.2.

Table 5.4 summarizes the renormalizations computed within AHC formalism. For most of the molecules, using hybrid functionals does not significantly change the gap renormalization relative to LDa or PBE results. For example, the energy gap renormalizations of the H_2 molecule computed with LDA, PBE, PBE0 and B3LYP functionals are 58 meV, 61 meV, 63 meV and 63 meV, respectively. However, hybrid functionals do reduce the magnitude of gap renormailization in several systems, and CO_2 and CH_3Cl are representative examples. In CO_2 the renormailization is reduced from -425 meV at the PBE level to -127 meV at the PBE0 level of theory; in CH_3Cl, the renormalization changes from -149 meV (PBE) to -59 meV (PBE0). In these two examples, the renormailizations computed with hybrid functionals are less the 50% of those computed with a GGA functional. This finding highlights

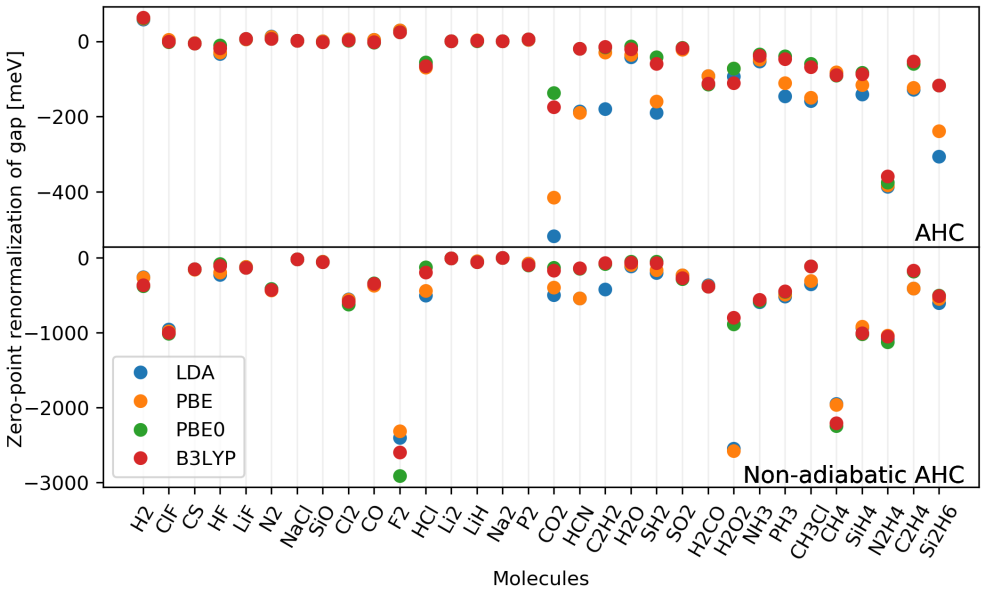

Figure 5.2: Computed zero-point renormalization energies of the HOMO-LUMO gaps of small molecules.

the need to compute electron-phonon renormailizations at the hybrid level of theory.

Next, we go beyond the AHC formalism. Using the so-called non-adiabatic AHC formalism (See Table 2.1), we avoid the approximation that neglects phonon frequencies in Fan-Migdal self-energy, and the results are listed in Table 5.5. The non-adiabatic AHC formalism significantly influences the computed magnitude of the gap renormalization in most of the molecules with exceptions like CO_2. For example, the H_2 gap renormailization changes from 63 meV to −377 meV with the PBE0 functional. The most significant differences are found in the F_2 and H_2O_2 molecules. Within the AHC formalism, the gap renormailizations computed at the PBE0 level in F_2 and H_2O_2 are 25 and −72 meV respectively, but they are −2914 and 891 meV with non-adiabatic AHC method. Not only did the non-adiabaticity change the sign of the renormailization, but the magnitude has also been changed significantly.

Table 5.4: List of HOMO-LUMO energy gaps of small molecules and their zero-point renormalization energy (ZPR) computed within the Allen-Heine-Cardona approximation. All gaps and ZPRs are in eV. We compare results obtained with different energy functionals (LDA, PBE, PBE0 and B3LYP).

Molecule	LDA		PBE		PBE0		B3LYP	
	gap	ZPR	gap	ZPR	gap	ZPR	gap	ZPR
H_2	9.998	0.058	10.164	0.061	11.890	0.063	11.648	0.063
ClF	3.194	0.004	3.167	0.005	6.250	-0.002	5.629	-0.001
CS	3.954	-0.004	4.042	-0.004	6.562	-0.006	6.199	-0.006
HF	8.681	-0.032	8.598	-0.030	11.302	-0.011	10.809	-0.018
LiF	5.108	0.006	4.723	0.006	7.014	0.007	6.601	0.007
N_2	8.221	0.013	8.319	0.013	11.707	0.007	11.179	0.008
NaCl	3.524	0.002	3.225	0.002	5.069	0.002	4.577	0.002
SiO	4.524	0.001	4.549	0.001	6.764	-0.002	6.368	-0.002
Cl_2	2.899	0.006	2.894	0.006	5.503	0.002	4.887	0.003
CO	6.956	0.005	7.074	0.004	10.055	-0.003	9.575	-0.002
F_2	3.495	0.030	3.370	0.029	7.840	0.025	6.917	0.025
HCl	6.768	-0.061	6.784	-0.069	8.858	-0.055	8.417	-0.066
Li_2	1.532	0.001	1.524	0.001	2.582	0.001	2.343	0.001
LiH	2.985	0.002	2.873	0.003	4.424	0.001	4.117	0.002
Na_2	1.564	0.001	1.521	0.001	2.495	0.000	2.264	0.001
P_2	3.649	0.005	3.644	0.005	5.537	0.005	5.107	0.005
CO_2	8.075	-0.517	8.033	-0.415	10.159	-0.137	9.708	-0.174
HCN	7.878	-0.185	7.930	-0.190	10.186	-0.020	9.806	-0.019
H_2O	6.272	-0.042	6.208	-0.036	8.511	-0.013	8.084	-0.020
SH_2	5.212	-0.189	5.238	-0.160	6.942	-0.042	6.593	-0.059
SO_2	3.457	-0.019	3.414	-0.021	6.087	-0.016	5.596	-0.018
H_2CO	3.470	-0.091	3.589	-0.092	6.451	-0.114	5.993	-0.111
H_2O_2	5.028	-0.093	4.887	-0.071	7.780	-0.072	7.505	-0.110
NH_3	5.395	-0.053	5.304	-0.048	7.205	-0.035	6.825	-0.038
PH_3	5.999	-0.146	5.946	-0.110	7.388	-0.039	7.056	-0.047
C_2H_2	6.703	-0.179	6.712	-0.029	8.181	-0.016	7.835	-0.014
CH_3Cl	6.232	-0.158	6.210	-0.149	8.042	-0.059	7.691	-0.068
CH_4	8.799	-0.084	8.820	-0.081	10.647	-0.091	10.320	-0.090
SiH_4	7.727	-0.141	7.772	-0.115	9.440	-0.083	9.187	-0.086
N_2H_4	4.892	-0.386	4.866	-0.383	6.736	-0.375	6.426	-0.359
C_2H_4	5.654	-0.129	5.673	-0.123	7.592	-0.059	7.224	-0.053
Si_2H_6	6.364	-0.305	6.386	-0.238	7.874	-0.117	7.609	-0.117

Table 5.5: List of HOMO-LUMO gaps of small molecules and their zero-point renormalization energies (ZPR) computed within the non-adiabatic Allen-Heine-Cardona approximation. All gaps and ZPRs are in eV. We compare results obtained with different energy functionals (LDA, PBE, PBE0, B3LYP).

Molecule	LDA		PBE		PBE0		B3LYP	
	gap	ZPR	gap	ZPR	gap	ZPR	gap	ZPR
H_2	9.998	-0.260	10.164	-0.263	11.890	-0.377	11.648	-0.366
ClF	3.194	-0.959	3.167	-0.985	6.250	-1.011	5.629	-1.000
CS	3.954	-0.151	4.042	-0.156	6.562	-0.155	6.199	-0.154
HF	8.681	-0.225	8.598	-0.194	11.302	-0.083	10.809	-0.111
LiF	5.108	-0.123	4.723	-0.122	7.014	-0.134	6.601	-0.134
N_2	8.221	-0.418	8.319	-0.432	11.707	-0.418	11.179	-0.428
NaCl	3.524	-0.021	3.225	-0.022	5.069	-0.022	4.577	-0.022
SiO	4.524	-0.052	4.549	-0.054	6.764	-0.056	6.368	-0.055
Cl_2	2.899	-0.557	2.894	-0.560	5.503	-0.622	4.887	-0.589
CO	6.956	-0.361	7.074	-0.373	10.055	-0.338	9.575	-0.346
F_2	3.495	-2.405	3.370	-2.317	7.840	-2.914	6.917	-2.600
HCl	6.768	-0.501	6.784	-0.440	8.858	-0.128	8.417	-0.195
Li_2	1.532	-0.007	1.524	-0.008	2.582	-0.010	2.343	-0.010
LiH	2.985	-0.049	2.873	-0.045	4.424	-0.055	4.117	-0.058
Na_2	1.564	-0.002	1.521	-0.002	2.495	-0.002	2.264	-0.002
P_2	3.649	-0.077	3.644	-0.079	5.537	-0.100	5.107	-0.096
CO_2	8.075	-0.495	8.033	-0.398	10.159	-0.136	9.708	-0.174
HCN	7.878	-0.543	7.930	-0.541	10.186	-0.147	9.806	-0.138
H_2O	6.272	-0.114	6.208	-0.095	8.511	-0.050	8.084	-0.061
SH_2	5.212	-0.203	5.238	-0.166	6.942	-0.050	6.593	-0.069
SO_2	3.457	-0.231	3.414	-0.234	6.087	-0.281	5.596	-0.274
H_2CO	3.470	-0.364	3.589	-0.376	6.451	-0.386	5.993	-0.382
H_2O_2	5.028	-2.549	4.887	-2.582	7.780	-0.891	7.505	-0.799
NH_3	5.395	-0.590	5.304	-0.566	7.205	-0.578	6.825	-0.562
PH_3	5.999	-0.516	5.946	-0.493	7.388	-0.453	7.056	-0.450
C_2H_2	6.703	-0.420	6.712	-0.074	8.181	-0.080	7.835	-0.073
CH_3Cl	6.232	-0.351	6.210	-0.307	8.042	-0.112	7.691	-0.116
CH_4	8.799	-1.950	8.820	-1.961	10.647	-2.245	10.320	-2.210
SiH_4	7.727	-0.931	7.772	-0.916	9.440	-1.019	9.187	-1.007
N_2H_4	4.892	-1.082	4.866	-1.038	6.736	-1.129	6.426	-1.050
C_2H_4	5.654	-0.408	5.673	-0.411	7.592	-0.184	7.224	-0.173
Si_2H_6	6.364	-0.607	6.386	-0.551	7.874	-0.506	7.609	-0.507

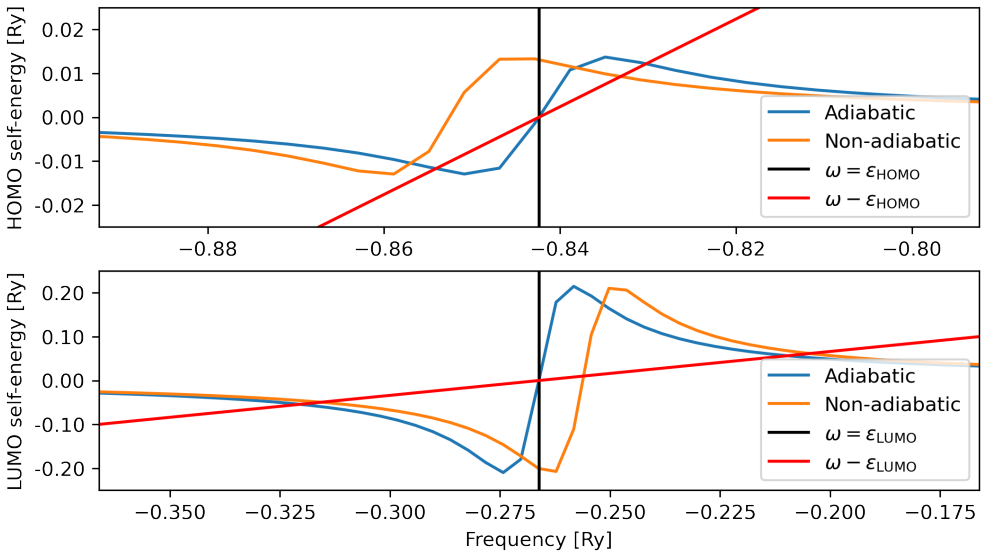

Figure 5.3: Analysis of the frequency-dependent self-energies of the HOMO and LUMO orbitals of the F_2 molecule.

To analyze the reason why the non-adiabatic AHC formalism had such a big effect in the calculation of renormailizations, we computed the frequency-dependent electron-phonon self-energies in the F_2 molecule and they are shown in Figure 5.3. The AHC result reported in Table 5.4 corresponds to the intersection of the black and blue lines, while the non-adiabatic AHC result reported in Table 5.5 corresponds to the intersection of the black and orange lines. From Figure 5.3, we clearly see that the self-energies oscillate near the black line, which corresponds to the HOMO, LUMO energy levels in the upper and lower plots. In the non-adiabatic case, the black line happens to intersect the orange lines at the peak or valley, thus they significantly differ from the intersections of the black and blue lines.

Next, we avoid the on-the-mass-shell (OMS) approximation (see Table 2.1) and solve for the renormalizations using the frequency-dependent self-energies,

$$\omega - \varepsilon_n^{\mathrm{KS}} = \Sigma_n(\omega). \tag{5.27}$$

In the plot, the red line represents $\omega - \epsilon_n^{\mathrm{KS}}$, and the blue and orange curves are fully frequency-dependent adiabatic and non-adiabatic self-energies, respectively. Thus, the solutions of the equation above correspond to the intersections between the red, blue or orange curves in Figure 5.3.

Within the AHC formalism, the approximate renormailization, the intersection between the black and blue curves, happens to be relatively accurate, as the red line intersects the blue line at the the same point. But, with non-adiabatic self-energies, the on-mass-shell approximation is not accurate for the self-consistent solutions, as the black line intersects the orange line far away from the intersection of the red and orange lines. We also notice that the red line intersects the blue and orange lines in multiple locations. This indicates that the quasiparticle approximation does not work well for the F_2 molecules when electron-phonon interactions are considered, and satellite peaks are created. In sum, neither the AHC nor the non-adiabtic AHC formalism correctly describes the self-energies in the full

energy range, and thus we suggest that the frequency-dependent self-energies should always computed whenever possible.

5.3.3 Renormalization of the energy gap of diamond

We computed the electron-phonon renormalization of the energy gap in diamond within the AHC formalism, and beyond the AHC formalism by solving the full frequency-dependent non-adiabatic (FF-NA) self-energies self-consistently (see Table 2.1). The calculations for diamond were carried out in a $3\times3\times3$ supercell with an energy cutoff of 60 Ry and SG15[123] ONCV[57] pseudopotentials.

In Figure 5.4, we present the temperature-dependent indirect gap renormalization computed with the PBE and PBE0 functionals. Within the same level of approximation, e.g., the AHC formalism (circles in the plot), the PBE and PBE0 results are almost the same for temperatures lower than 400 K, but their difference gets larger for higher temperatures. With the same functional, e.g., the PBE0 functional (orange lines in the plot), the results obtained with the full frequency-dependent non-adiabatic self-energies are lower than those obtained with the AHC formalism. In general, the use of the PBE0 hybrid functional does not significantly change the trend of the ZPRs as a function of temperature.

We report the renormalized energy gap in Figure 5.5 with a comparison with experimental measurements, and we list them in Table 5.6. Although the PBE0 hybrid functional does not significantly change the trend of the electron-phonon renormalization as a function of temperature, the renormalized gap are noticeably improved compared to experimental measurements. The indirect energy gap of diamond computed with PBE and PBE0 without electron-phonon renormalizaiton are 4.016 and 6.040 eV, respectively, and the experimental indirect gap measured at approximately 100 K is 5.45 eV.[101] Comparing the computational and experimental results, we find the the PBE gap is about 1.5 eV lower while the PBE0 gap is about 0.60 eV higher than the experimental gap. By including electron-phonon renormal-

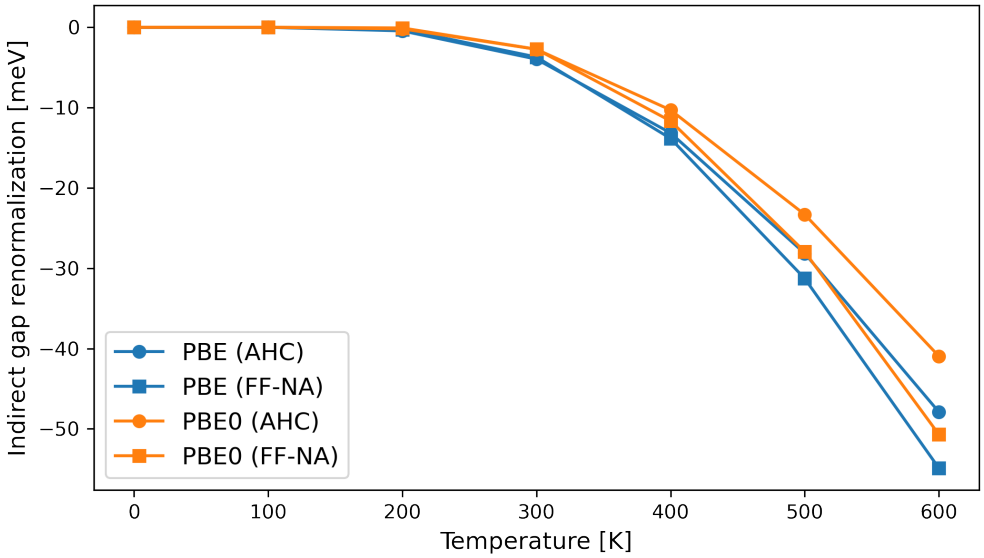

Figure 5.4: The electron-phonon renormalization energy computed within the Allen-Heine-Cardona (AHC) approximation, and beyond the AHC approximation by computing the full frequency-dependent non-adiabatic (FF-NA) self-energy self-consistently. The renormailzation energy at zero temperature has been shifted to zero.

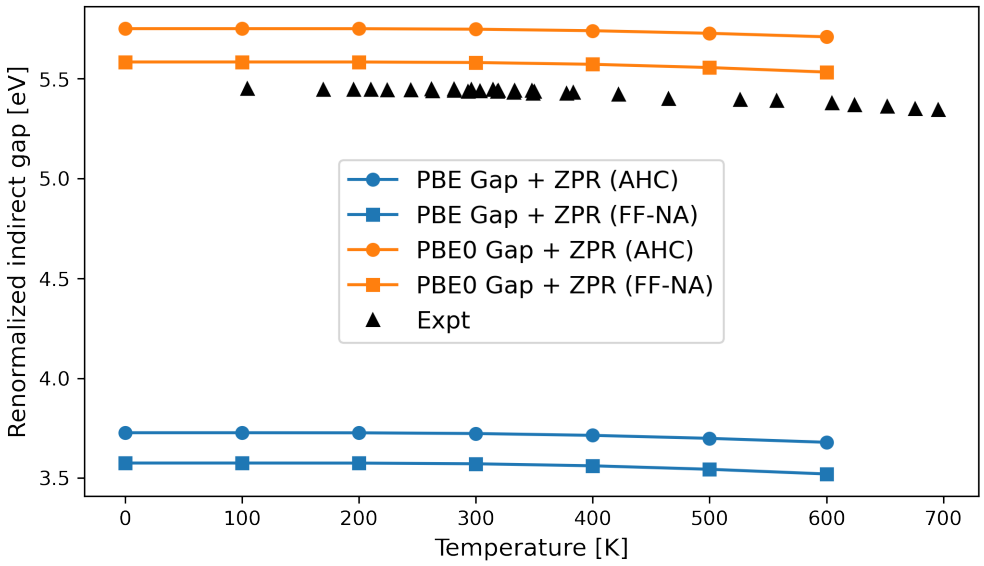

Figure 5.5: The electron-phonon renormalized indirect energy gap in diamond computed with the PBE and PBE0 functionals compared to experimental measurements.[101] We show calculations performed with the Allen-Heine-Cardona (AHC) formalism and with the full frequency-dependent non-adiabatic (FF-NA) self-energies.

Table 5.6: The temperature-dependent zero-point renormalization energy (ZPR) and renormalized indirect energy gap (Gap+ZPR) computed with the PBE and PBE0 functionals and using the Allen-Heine-Cardona (AHC) formalism or the full frequency-dependent non-adiabatic (FF-NA) self-energies. The energy gaps computed at the PBE and PBE0 level of theory, without electron-phonon interaction, are 4.016 and 6.040 eV respectively. All energies are reported in eV.

T[K]	PBE(AHC)		PBE(FF-NA)		PBE0(AHC)		PBE0(FF-NA)	
	ZPR	Gap+ZPR	ZPR	Gap+ZPR	ZPR	Gap+ZPR	ZPR	Gap+ZPR
0	-0.288	3.727	-0.440	3.575	-0.290	5.750	-0.457	5.584
100	-0.288	3.727	-0.440	3.575	-0.290	5.750	-0.457	5.584
200	-0.288	3.727	-0.440	3.575	-0.290	5.750	-0.457	5.584
300	-0.292	3.723	-0.444	3.572	-0.292	5.748	-0.459	5.581
400	-0.302	3.714	-0.454	3.562	-0.300	5.740	-0.468	5.572
500	-0.317	3.699	-0.471	3.544	-0.313	5.727	-0.485	5.556
600	-0.336	3.679	-0.495	3.520	-0.331	5.710	-0.507	5.533

izaitons, we can see that the results computed at the PBE0 level of theory agree well with the experimental measurements (see Figure 5.5 and Table 5.6). The renormalized indirect gap computed with the PBE0 functional at 100 K is 5.75 eV when the AHC formalism is used, while it is 5.584 eV when the self-consistent full frequency-dependent non-adiabatic (FF-NA) self-energies are used. Compared to experiment 5.45 eV, the difference is only 0.3 and 0.13 eV with AHC and FF-NA, respectively. Thus, computing electron-phonon interactions at the hybrid level of theory is a promising protocol to obtain results comparable to experiments.

5.4 Conclusions

In conclusion, we implemented the calculatins of phonon and electron-phonon interaction at the level of hybrid functionals by applying density matrix perturbation theory and by solving the Liouville equation. Using this approach, we obtain phonon frequencies that are comparable to those of the frozen-phonon approach and electron-phonon self-energies comparable to those of the frozen-phonon and PIMD approaches. By using the Lanczos

algorithm, we computed the full frequency-dependent non-adiabatic electron-phonon self-energies beyond the AHC formalism.

We carried out a study of a set of small molecules with LDA, PBE, B3LYP and PBE0 functionals, and found it was necessary to analyze the frequency-dependent self-energies to fully understand the electronic structure of these molecules. In addition, we conducted calculations of the electronic structure of diamond with the PBE and PBE0 functionals, and found that the PBE0 funtional noticeably improved the renormalized energy gap compared to experimental measurements. Computing electron-phonon interactions at the hybrid functional level of theory is a promising protocol to understand experiments and to obtain accurate predictions of the electronic structure of materials, e.g., for materials discovery purposes. The method proposed in this chapter can incorporate spin polarizations to study the electron-phonon interactions in open-shell molecules, e.g., O_2, and spin defects, e.g., NV^- in diamond and its full spin-polarized implementation is work in progress.

CHAPTER 6

CONCLUSIONS AND OUTLOOK

This dissertation focuses on developing first principles methods to compute electron-electron and electron-phonon interactions in solids and molecules.

We first developed an approach to generate approximate eigenvectors of dielectric matrices by solving an approximate form of the Sternheimer equation. The approximate eigenvectors were used in G_0W_0 calculations, which were verified by computing the vertical ionization potentials and affinity energies of a set of small molecules. After verification, we computed the energy levels of the C_{60} molecule and the band alignments at the silicon/silicon nitride interface. Using our approximate basis, we found results in good agreement with those obtained without approximations and we reduced the computational cost by 50%.

We evaluated the electron-phonon renormailization of electronic energy levels by generalizing a method that combines the calculations of the electron-electron and electron-phonon interactions in solids. We first verified our implementation with existing literature results reported for diamond. Then we conducted a detailed study of the zero-point renormailization in diamond with our method. To showcase our ability to perform calculations for large scale systems, we computed the renormailization of defects in diamond. In addition, our implementation allows one to perform calculations beyond the Allen-Heine-Cardona (AHC) formalism, and we showed that going beyond the AHC approximation can significantly influence the results.

The method to combine electron-electron and electron-phonon interactions described in Chapter 4 only introduced G_0W_0 corrections to energy levels in electron-phonon calculations, but the single particle wavefuntions were not modified. To further improve our calculations, we implemented the evaluation of electron-phonon interactions at the level of hybrid functionals. In this way, not only did we change the eigenvalues used in the expression of the electron-phonon interaction, but we also improved the single particle wavefunctions. To ver-

ify our implementation, we compared our computed phonon frequencies with those of the frozen-phonon approach, and compared the electron-phonon self-energies with those of the frozen-phonon and path integral molecular dynamics approaches. Then we computed the renormailizations due to electron-phonon interactions for a set of small molecules within the AHC formalism and going beyond that formalism. We also realized that including the full frequency-dependent self-energies is necessary for some of the molecules in order to obtain accurate results.

Our method to compute phonons and electron-phonon interactions at the hybrid functional level of theory, which solves the Liouville equation, can be extended to include spin polarization and such an implementation is in progress.

In summary, predicting the electronic structure of molecules and solids is one of the most fundamental problems in quantum chemistry, and to attack this problem it is necessary to develop theoretical and numerical techniques to accurately describe both electron-electron and electron-phonon interactions. This thesis is a contribution to such developments as well as applications encompassing the electronic structure of solids and small molecules.

6.1 List of publications

1. **Han Yang**, Marco Govoni, and Giulia Galli. Improving the efficiency of G_0W_0 calculations with approximate spectral decompositions of dielectric matrices. *J. Chem. Phys.*, 151(22):224102, 2019.

2. Arpan Kundu, Marco Govoni, **Han Yang**, Michele Ceriotti, Francois Gygi, and Giulia Galli. Quantum Vibronic Effects on the Electronic Properties of Solid and Molecular Carbon. *Phys. Rev. Mat.*, 5(7):L070801, 2021.

3. **Han Yang**, Marco Govoni, Arpan Kundu and Giulia Galli. Combined first-principles calculations of electron-electron and electron-phonon self-energies in condensed sys-

tems. Submitted. arXiv:2106.13073, 2021

4. **Han Yang**, Arpan Kundu, Marco Govoni, and Giulia Galli. Electron-phonon interactions at the level of hybrid functionals. In preparation.

6.2 Code development

1. Solving the kinetic Sternheimer equation to generate the kinetic PDEP basis as a part of the `WEST` code.

2. Combining the calculations of GW approximation and electron-phonon interactions in solids, with $\mathbf{k}$ and $\mathbf{q}$ sampling, as a part of the `WEST` code.

3. Electron-phonon interactions at the level of hybrid functional by solving the Liouville equation, as a part of the `WEST` code.

APPENDIX A

CALCULATION OF PHONONS WITHIN LINEAR RESPONSE THEORY

A.1 Born-von Kármán boundary conditions

We describe a solid using Born-von Kármán periodic boundary conditions: we consider wavefunctions to be periodic within a supercell (with volume Ω_s), which contains N_c replicas of the unit cell (with volume Ω_c), so that $N_c = \frac{\Omega_c}{\Omega_s}$. We use μ to label the index of the unit cell within the supercell, and I to label the index of one atom within one unit cell. There are N_{at} and $N_c \times N_{at}$ in one unit cell and in the supercell, respectively.

A.2 Force constants and dynamical matrices

The total energy of a supercell, $E_{\rm tot}(\{\mathbf{R}_{\mu I}\})$, is a function of the coordinates of $N_c \times N_{at}$ ions. We displace all ions within the supercell by $\mathbf{u}_{\mu I}$, and proceed with the following Taylor expansion

$$E_{\rm tot}(\{\mathbf{R}_{\mu I} + \mathbf{u}_{\mu I}\}) = E_{\rm tot}(\{\mathbf{R}_{\mu I}\}) + \sum_{\mu I \alpha} \frac{\partial E_{\rm tot}}{\partial u_{\mu I \alpha}} u_{\mu I \alpha} \tag{A.1}$$

$$+ \frac{1}{2} \sum_{\mu I \alpha, \mu' J \beta} u_{\mu I \alpha} \frac{\partial^2 E_{\rm tot}}{\partial u_{\mu I \alpha} \partial u_{\mu' J \beta}} u_{\mu' J \beta}, \tag{A.2}$$

and the kinetic operator can be written as

$$\hat{K} = -\frac{1}{2} \sum_{\mu I \alpha} \frac{1}{M_I} \frac{\partial^2}{\partial u_{\mu I \alpha}^2} \tag{A.3}$$

where $x_{\mu I\alpha}$ is the displacement of I-th atom, in the μ-th cell, and along α Cartesian direction. The displacements u satisfy the following Fourier transform relations,

$$u_{\mu I\alpha} = \frac{1}{\sqrt{N_c}} \sum_{\mathbf{q}} u_{I\alpha\mathbf{q}} e^{i\mathbf{q}\cdot\mathbf{R}_\mu} \tag{A.4}$$

$$u_{I\alpha\mathbf{q}} = \frac{1}{\sqrt{N_c}} \sum_{\mu} u_{\mu I\alpha} e^{-i\mathbf{q}\cdot\mathbf{R}_\mu} \tag{A.5}$$

where $\mathbf{q}$ is a wave vector and N_c is the number of unit cells in the supercell. $u_{I\alpha\mathbf{q}}$ is periodic in terms of unit cells.

Using the equations above, we can also write the equations for their derivatives,

$$\frac{\partial}{\partial u_{I\alpha\mathbf{q}}} = \frac{1}{\sqrt{N_c}} \sum_{\mu} e^{i\mathbf{q}\cdot\mathbf{R}_\mu} \frac{\partial}{\partial u_{\mu I\alpha}} \tag{A.6}$$

$$\frac{\partial}{\partial u_{\mu I\alpha}} = \frac{1}{\sqrt{N_c}} \sum_{\mathbf{q}} e^{-i\mathbf{q}\cdot\mathbf{R}_\mu} \frac{\partial}{\partial u_{I\alpha\mathbf{q}}} \tag{A.7}$$

So, we can rewrite kinetic energy as

$$\hat{K} = -\frac{1}{2} \sum_{I\alpha\mathbf{q}} \frac{1}{M_I} \frac{\partial^2}{\partial u^*_{I\alpha\mathbf{q}} \partial u_{I\alpha\mathbf{q}}} \tag{A.8}$$

and second derivative of potential energy as

$$\sum_{\mu I\alpha,\nu J\beta} u_{\mu I\alpha} \frac{\partial^2 E_{\text{tot}}}{\partial u_{\mu I\alpha} \partial u_{\mu' J\beta}} u_{\mu' J\beta} = \sum_{I\alpha,J\beta} \sum_{\mathbf{q}} u^*_{I\alpha\mathbf{q}} \frac{\partial^2 E_{\text{tot}}}{\partial u^*_{I\alpha\mathbf{q}} \partial u_{J\beta\mathbf{q}}} u_{J\beta\mathbf{q}} \tag{A.9}$$

and we define

$$C_{I\alpha,J\beta}(\mathbf{q}) = \frac{\partial^2 E_{\text{tot}}}{\partial u^*_{I\alpha\mathbf{q}} \partial u_{J\beta\mathbf{q}}} \tag{A.10}$$

the force constant matrix and

$$D_{I\alpha,J\beta}(\mathbf{q}) = \frac{1}{\sqrt{M_I M_J}} C_{I\alpha,J\beta}(\mathbf{q}) \tag{A.11}$$

the dynamical matrix. $D_{I\alpha,J\beta}(\mathbf{q})$ is a $\mathbf{q}$-dependent $(3 \times N_{at}) \times (3 \times N_{at})$ matrix.

A.3 Derivatives of wavefunction, density and potential

Before discussing Sternheimer equation, we first analyze the periodicity of the derivatives of wavefunction,

$$\frac{\partial \psi_{n\mathbf{k}}(\mathbf{r})}{\partial u_{I\alpha\mathbf{q}}} = e^{i\mathbf{k}\cdot\mathbf{r}} \frac{\partial \phi_{n\mathbf{k}}(\mathbf{r})}{\partial u_{I\alpha\mathbf{q}}} \tag{A.12}$$

where $\psi_{n\mathbf{k}} = \phi_{n\mathbf{k}} e^{+i\mathbf{k}\cdot\mathbf{r}}$ according to Bloch theorem and $\phi_{n\mathbf{k}}$ is lattice periodic. However, the derivative of $\phi_{n\mathbf{k}}$ with respect to $u_{I\alpha\mathbf{q}}$ is not lattice periodic.

Lemma A.3.1. *$e^{-i\mathbf{q}\cdot\mathbf{r}} \frac{\partial \phi_{n\mathbf{k}}}{\partial u_{I\alpha\mathbf{q}}}$ is lattice periodic.*

Proof.

$$\begin{aligned}
\frac{\partial \phi_{n\mathbf{k}}(\mathbf{r}+\mathbf{R}_{\mu'})}{\partial u_{I\alpha\mathbf{q}}} e^{-i\mathbf{q}\cdot(\mathbf{r}+\mathbf{R}_{\mu'})} &= \frac{1}{\sqrt{N_c}} \sum_{\mu} \frac{\partial \phi_{n\mathbf{k}}(\mathbf{r}+\mathbf{R}_{\mu'})}{\partial u_{\mu I\alpha}} e^{i\mathbf{q}\cdot\mathbf{R}_{\mu}} e^{-i\mathbf{q}\cdot(\mathbf{r}+\mathbf{R}_{\mu'})} \\
&= \frac{1}{\sqrt{N_c}} \sum_{\mu} \frac{\partial \phi_{n\mathbf{k}}(\mathbf{r})}{\partial u_{\mu-\mu',I\alpha}} e^{i\mathbf{q}\cdot(\mathbf{R}_{\mu}-\mathbf{R}_{\mu'})} e^{-i\mathbf{q}\cdot\mathbf{r}} \\
&= \frac{\partial \phi_{n\mathbf{k}}(\mathbf{r})}{\partial u_{I\alpha\mathbf{q}}} e^{-i\mathbf{q}\cdot\mathbf{r}}
\end{aligned} \tag{A.13}$$

□

Now, we define

$$\frac{\partial \phi_{n\mathbf{k}}(\mathbf{r})}{\partial u_{I\alpha\mathbf{q}}} = e^{+i\mathbf{q}\cdot\mathbf{r}} \frac{\tilde{\partial} \phi_{n\mathbf{k}}(\mathbf{r})}{u_{I\alpha\mathbf{q}}} \tag{A.14}$$

where $\tilde{\partial}\phi_{n\mathbf{k}}/u_{I\alpha\mathbf{q}}$ is a lattice periodic function. So, we have

$$\frac{\partial\psi_{n\mathbf{k}}(\mathbf{r})}{\partial u_{I\alpha\mathbf{q}}} = e^{i(\mathbf{k}+\mathbf{q})\cdot\mathbf{r}}\frac{\tilde{\partial}\phi_{n\mathbf{k}}(\mathbf{r})}{\partial u_{I\alpha\mathbf{q}}}. \tag{A.15}$$

Using the same approach above, we define the derivatives of potentials

$$\frac{\partial V(\mathbf{r})}{\partial u_{I\alpha\mathbf{q}}} = e^{+i\mathbf{q}\cdot\mathbf{r}}\frac{\tilde{\partial}V(\mathbf{r})}{\partial u_{I\alpha\mathbf{q}}}, \tag{A.16}$$

where $\tilde{\partial}V/\partial u_{I\alpha\mathbf{q}}$ is lattice periodic, and the derivatives of charge densities,

$$\frac{\partial n(\mathbf{r})}{\partial u_{I\alpha\mathbf{q}}} = e^{i\mathbf{q}\cdot\mathbf{r}}\frac{\tilde{\partial}n(\mathbf{r})}{\partial u_{I\alpha\mathbf{q}}}, \tag{A.17}$$

where $\tilde{\partial}n(\mathbf{r})/\partial u_{I\alpha\mathbf{q}}$ is lattice periodic.

In addition, second derivatives of potentials $\frac{\partial^2 V(\mathbf{r})}{\partial u^*_{I\alpha\mathbf{q}}\partial u_{J\beta\mathbf{q}}}$ are lattice periodic. The potentials above are generic; they can be external potential V_{ext} or scf potential V_{scf}.

A.4 Sternheimer equation

Now, we derive Sternheimer equation to connect the derivatives of wavefunctions, potentials and charge densities.

We start from Kohn-Sham equation,

$$(H^{\text{KS}} - \varepsilon_{n\mathbf{k}})\psi_{n\mathbf{k}} = 0, \tag{A.18}$$

where $H^{\text{KS}} = -\nabla^2/2 + V_{\text{scf}}$ is the Kohn-Sham Hamiltonian, $\varepsilon_{n\mathbf{k}}$ is the n-th energy level at

k point and $\psi_{n\mathbf{k}}$ is the Kohn-Sham orbital. We expand the quantities in Taylor expansion,

$$\begin{aligned} V_{\text{scf}} &= V^0_{\text{scf}} + \sum_{I\alpha} \frac{\partial V_{\text{scf}}}{\partial u_{I\alpha\mathbf{q}}} u_{I\alpha\mathbf{q}} \\ \psi_{n\mathbf{k}} &= \psi^0_{n\mathbf{k}} + \sum_{I\alpha} \frac{\psi_{n\mathbf{k}}}{\partial u_{I\alpha\mathbf{q}}} u_{I\alpha\mathbf{q}}. \end{aligned} \tag{A.19}$$

where the quantities with superscipts 0 are those of the unperturbed system. Putting the potentials and wavefunctions into the Kohn-Sham equation and keeping terms up to first order in spirit of linear response theory, we have the Sternherimer's equation

$$(H^{\text{KS}} - \varepsilon_{n\mathbf{k}}) \frac{\partial \psi_{n\mathbf{k}}}{\partial u_{I\alpha\mathbf{q}}} = -\frac{\partial V_{\text{scf}}}{\partial u_{I\alpha\mathbf{q}}} \psi_{n\mathbf{k}} \tag{A.20}$$

The change of density is

$$\begin{aligned} \frac{\partial n}{\partial u_{I\alpha\mathbf{q}}} = 2 \sum_{\mu}^{N_{\text{occ}}} \sum_{\mathbf{k}} \Bigg[& \mathcal{P}^c \frac{\partial \psi^*_{n\mathbf{k}}}{\partial u_{I\alpha\mathbf{q}}} \psi_{n\mathbf{k}} + \psi^*_{n\mathbf{k}} \mathcal{P}^c \frac{\partial \psi_{n\mathbf{k}}}{\partial u_{I\alpha\mathbf{q}}} \\ & + \mathcal{P}^v \frac{\partial \psi^*_{n\mathbf{k}}}{\partial u_{I\alpha\mathbf{q}}} \psi_{n\mathbf{k}} + \psi^*_{n\mathbf{k}} \mathcal{P}^v \frac{\partial \psi_{n\mathbf{k}}}{\partial u_{I\alpha\mathbf{q}}} \Bigg], \end{aligned} \tag{A.21}$$

where $\mathcal{P}^v$ and $\mathcal{P}^c$ are projection operators onto valence and conduction bands. The sum of the two terms containing $\mathcal{P}^v$ is zero. So the change of density depends only on $\mathcal{P}^c \partial\psi/\partial u$. Now, we can rewrite Sternheimer equation,

$$(H^{\text{KS}} - \epsilon_{n\mathbf{k}}) \mathcal{P}^c \frac{\partial \psi_{n\mathbf{k}}}{\partial u_{I\alpha\mathbf{q}}} = -\mathcal{P}^c \frac{\partial V_{\text{scf}}}{\partial u_{I\alpha\mathbf{q}}} \psi_{n\mathbf{k}}. \tag{A.22}$$

This can be further simplified by using the lattice periodic functions introduced above. Note

that,

$$\begin{aligned}\mathcal{P}^c &= 2\sum_{n}^{N_{\text{occ}}}\sum_{\mathbf{k}'}\psi_{n\mathbf{k}'}(\mathbf{r})\psi^*_{n\mathbf{k}'}(\mathbf{r}') \\ &= 2\sum_{n}^{N_{\text{occ}}}\sum_{\mathbf{k}'}e^{+i\mathbf{k}'\cdot\mathbf{r}}\phi_{n\mathbf{k}'}(\mathbf{r})\phi_{n\mathbf{k}'}(\mathbf{r}')e^{-i\mathbf{k}'\cdot\mathbf{r}'}\end{aligned} \tag{A.23}$$

and

$$\frac{\partial\psi_{n\mathbf{k}}}{\partial u_{I\alpha\mathbf{q}}} = e^{+i(\mathbf{k}+\mathbf{q})\cdot\mathbf{r}}\frac{\tilde{\partial}\phi_{n\mathbf{k}}}{\partial u_{I\alpha\mathbf{q}}}. \tag{A.24}$$

So, only the component $\mathbf{k}' = \mathbf{k}+\mathbf{q}$ gives nonzero contribution. This conclusion is also applicable to the derivative of potential on the right hand side of Sternheimer equation. The Sternheimer equation now reads

$$(H^{\text{KS}} - \epsilon_{n\mathbf{k}})e^{-i(\mathbf{k}+\mathbf{q})\cdot\mathbf{r}}\mathcal{P}^c_{\mathbf{k}+\mathbf{q}}\frac{\tilde{\partial}\phi_{n\mathbf{k}}}{\partial u_{I\alpha\mathbf{q}}} = -e^{i(\mathbf{k}+\mathbf{q})\cdot\mathbf{r}}\mathcal{P}^c_{\mathbf{k}+\mathbf{q}}\frac{\tilde{\partial}v_{\text{scf}}}{\partial u_{I\alpha\mathbf{q}}}\phi_{n\mathbf{k}} \tag{A.25}$$

So,

$$(H^{\text{HS}}_{\mathbf{k}+\mathbf{q}} - \epsilon_{n\mathbf{k}})\mathcal{P}^c_{\mathbf{k}+\mathbf{q}}\frac{\tilde{\partial}\phi_{n\mathbf{k}}}{\partial u_{I\alpha\mathbf{q}}} = -\mathcal{P}^c_{\mathbf{k}+\mathbf{q}}\frac{\tilde{\partial}V_{\text{scf}}}{\partial u_{I\alpha\mathbf{q}}}\phi_{n\mathbf{k}}, \tag{A.26}$$

where $H^{\text{KS}}_{\mathbf{k}+\mathbf{q}}$ is the deflated Hamiltonian $\mathcal{P}^c_{\mathbf{k}+\mathbf{q}}H^{\text{KS}}\mathcal{P}^c_{\mathbf{k}+\mathbf{q}}$.

It is worth noting that, we did not distinguish the lattice periodic wavefunction $\phi_{n\mathbf{k}}$ from $\psi_{n\mathbf{k}}$ in the main text for convenience, but the lattice periodic wavefunction should be used in implementation.

The change of density is

$$\frac{\tilde{\partial}n(\mathbf{r})}{\partial u_{I\alpha\mathbf{q}}} = 2\sum_{n}^{N_{\text{occ}}}\sum_{\mathbf{k}}\left[\phi^*_{n\mathbf{k}}(\mathbf{r})\mathcal{P}^c_{\mathbf{k}+\mathbf{q}}\frac{\tilde{\partial}\phi_{n\mathbf{k}}(\mathbf{r})}{\partial u_{I\alpha\mathbf{q}}} + c.c.\right] \tag{A.27}$$

where the prefactor 2 accounts for spins.

A.5 Evaluation of force constants

Recall that the Born-Oppenheimer[16] approximation decomposes the Hamiltonian into the electronic and ionic part, thus the force constants also consist the electronic and ionic part,

$$C_{I\alpha,J\beta}(\mathbf{q}) = C^{\text{el}}_{I\alpha,J\beta}(\mathbf{q}) + C^{\text{ion}}_{I\alpha,J\beta}(\mathbf{q}) \tag{A.28}$$

The ionic part is trivial to evaluate and its expression can be found in the appendix of Ref. 10.

The electronic part consists the following parts,

$$\begin{aligned} C^{\text{el}}_{I\alpha,J\beta}(\mathbf{q}) = 2\sum_{n}^{N_{\text{occ}}}\sum_{\mathbf{k}}\Bigg[&\left\langle \frac{\partial\psi_{n\mathbf{k}}}{\partial u_{I\alpha\mathbf{q}}}\middle|\frac{\partial V_{\text{ext}}}{\partial u_{J\beta\mathbf{q}}}\middle|\psi_{n\mathbf{k}}\right\rangle + c.c. \\ &+\left\langle \psi_{n\mathbf{k}}\middle|\frac{\partial^2 V_{\text{ext}}}{\partial u^*_{I\alpha\mathbf{q}}\partial_{J\beta\mathbf{q}}}\middle|\psi_{n\mathbf{k}}\right\rangle\Bigg] \end{aligned} \tag{A.29}$$

The last term is,

$$\left\langle \psi_{n\mathbf{k}}\middle|\frac{\partial^2 V_{\text{ext}}}{\partial u^*_{I\alpha\mathbf{q}}\partial u_{J\beta\mathbf{q}}}\middle|\psi_{n\mathbf{k}}\right\rangle = \delta_{IJ}\left\langle \phi_{n\mathbf{k}}\middle|\frac{\partial^2 V_{\text{ext}}}{\partial u^*_{I\alpha}(\mathbf{q}=\mathbf{0})\partial u_{J\beta}(\mathbf{q}=\mathbf{0})}\middle|\phi_{n\mathbf{k}}\right\rangle \tag{A.30}$$

and its expression can also be found in the appendix of Ref. 10. This quantity remains the same for all $\mathbf{q}$ points.

The rest term requires more effort,

$$C_{I\alpha,J\beta}(\mathbf{q}) \propto \left\langle \frac{\partial\psi_{n\mathbf{k}}}{\partial u_{I\alpha\mathbf{q}}}\middle|\frac{\partial V_{\text{ext}}}{\partial u_{J\beta\mathbf{q}}}\middle|\psi_{n\mathbf{k}}\right\rangle, \tag{A.31}$$

and it is the main topic of Chapter 4 and Chapter 5.

REFERENCES

[1] C. Adamo and V. Barone. Toward reliable density functional methods without adjustable parameters: The PBE0 model. *J. Chem. Phys.*, 110(13):6158–6170, Apr. 1999.

[2] S. L. Adler. Quantum theory of the dielectric constant in real solids. *Phys. Rev.*, 126(2):413, 1962.

[3] P. B. Allen and M. Cardona. Theory of the temperature dependence of the direct gap of germanium. *Phys. Rev. B*, 23(4):1495, Feb. 1981.

[4] P. B. Allen and V. Heine. Theory of the temperature dependence of electronic band structures. *J. Phys. C: Solid State Phys.*, 9(12):2305, June 1976.

[5] P. W. Anderson. More is different. *Science*, 177(4047):393–396, Aug. 1972.

[6] G. Antonius, S. Poncé, P. Boulanger, M. Côté, and X. Gonze. Many-body effects on the zero-point renormalization of the band structure. *Phys. Rev. Lett.*, 112(21):215501, May 2014.

[7] G. Antonius, S. Poncé, E. Lantagne-Hurtubise, G. Auclair, X. Gonze, and M. Côté. Dynamical and anharmonic effects on the electron-phonon coupling and the zero-point renormalization of the electronic structure. *Phys. Rev. B*, 92(8):085137, Aug. 2015.

[8] F. Aryasetiawan and O. Gunnarsson. The GW method. *Rep. Prog. Phys.*, 61(3):237–312, Mar. 1998.

[9] J. Bardeen, L. N. Cooper, and J. R. Schrieffer. Microscopic theory of superconductivity. *Phys. Rev.*, 106(1):162–164, Apr. 1957.

[10] S. Baroni, S. de Gironcoli, A. D. Corso, and P. Giannozzi. Phonons and related crystal properties from density-functional perturbation theory. *Rev. Mod. Phys.*, 73(2):515–562, July 2001.

[11] J. Bauer. Optical properties, band gap, and surface roughness of Si_3N_4. *Phys. Status Solidi A*, 39(2):411–418, 1977.

[12] A. D. Becke. Density-functional exchange-energy approximation with correct asymptotic behavior. *Phys. Rev. A*, 38(6):3098–3100, Sept. 1988.

[13] A. D. Becke. A new mixing of hartree–fock and local density-functional theories. *J. Chem. Phys.*, 98(2):1372–1377, Jan. 1993.

[14] M. Bernardi, D. Vigil-Fowler, J. Lischner, J. B. Neaton, and S. G. Louie. Ab InitioStudy of hot carriers in the first picosecond after sunlight absorption in silicon. *Phys. Rev. Lett.*, 112(25):257402, June 2014.

[15] F. Bloch. Über die quantenmechanik der elektronen in kristallgittern. *Z. Phys.*, 52(7-8):555–600, July 1929.

[16] M. Born and R. Oppenheimer. Zur quantentheorie der molekeln. *Ann. Phys. (Berlin)*, 389(20):457–484, 1927.

[17] N. P. Brawand, M. Govoni, M. Vörös, and G. Galli. Performance and self-consistency of the generalized dielectric dependent hybrid functional. *J. Chem. Theory Comput.*, 13(7):3318–3325, June 2017.

[18] N. P. Brawand, M. Vörös, M. Govoni, and G. Galli. Generalization of dielectric-dependent hybrid functionals to finite systems. *Phys. Rev. X*, 6(4):041002, Oct. 2016.

[19] F. Bruneval and X. Gonze. Accurate *gw* self-energies in a plane-wave basis using only a few empty states: Towards large systems. *Phys. Rev. B*, 78:085125, Aug. 2008.

[20] F. Bruneval, N. Vast, and L. Reining. Effect of self-consistency on quasiparticles in solids. *Phys. Rev. B*, 74(4):045102, July 2006.

[21] K. Burke. *The ABC of DFT*. 2007.

[22] E. Cannuccia and A. Marini. Effect of the quantum zero-point atomic motion on the optical and electronic properties of diamond and trans-polyacetylene. *Phys. Rev. Lett.*, 107(25):255501, Dec. 2011.

[23] E. Cannuccia and A. Marini. Zero point motion effect on the electronic properties of diamond, trans-polyacetylene and polyethylene. *Eur. Phys. J. B*, 85(9):320, Sept. 2012.

[24] R. B. Capaz, C. D. Spataru, P. Tangney, M. L. Cohen, and S. G. Louie. Temperature dependence of the band gap of semiconducting carbon nanotubes. *Phys. Rev. Lett.*, 94(3):036801, Jan. 2005.

[25] M. E. Casida. Time-dependent density functional response theory for molecules. In *Recent Advances in Density Functional Methods*, pages 155–192. World Scientific, Nov. 1995.

[26] M. Ceriotti and D. E. Manolopoulos. Efficient first-principles calculation of the quantum kinetic energy and momentum distribution of nuclei. *Phys. Rev. Lett.*, 109(10):100604, Sept. 2012.

[27] K. J. Chang, M. M. Dacorogna, M. L. Cohen, J. M. Mignot, G. Chouteau, and G. Martinez. Superconductivity in high-pressure metallic phases of si. *Phys. Rev. Lett.*, 54(21):2375–2378, May 1985.

[28] J. Čížek. On the correlation problem in atomic and molecular systems. calculation of wavefunction components in ursell-type expansion using quantum-field theoretical methods. *J. Chem. Phys.*, 45(11):4256–4266, Dec. 1966.

[29] L. A. Curtiss, P. C. Redfern, K. Raghavachari, and J. A. Pople. Assessment of gaussian-2 and density functional theories for the computation of ionization potentials and electron affinities. *J. Chem. Phys.*, 109(1):42–55, 1998.

[30] M. M. Dacorogna, M. L. Cohen, and P. K. Lam. Self-consistent calculation of the **q** dependence of the electron-phonon coupling in aluminum. *Phys. Rev. Lett.*, 55(8):837–840, Aug. 1985.

[31] S. V. Deshpande, E. Gulari, S. W. Brown, and S. C. Rand. Optical properties of silicon nitride films deposited by hot filament chemical vapor deposition. *J. Appl. Phys.*, 77(12):6534–6541, 1995.

[32] J. Deslippe, G. Samsonidze, D. A. Strubbe, M. Jain, M. L. Cohen, and S. G. Louie. Berkeleygw: A massively parallel computer package for the calculation of the quasiparticle and optical properties of materials and nanostructures. *Comput. Phys. Commun.*, 183(6):1269–1289, June 2012.

[33] P. A. M. Dirac. Quantum mechanics of many-electron systems. *Proc. R. Soc. London A.*, 123(792):714–733, Apr. 1929.

[34] H. Y. Fan. Temperature dependence of the energy gap in semiconductors. *Phys. Rev.*, 82(6):900, June 1951.

[35] A. Franceschetti. First-principles calculations of the temperature dependence of the band gap of si nanocrystals. *Phys. Rev. B*, 76(16):161301, Oct. 2007.

[36] H. Fröhlich, H. Pelzer, and S. Zienau. XX. properties of slow electrons in polar materials. *London, Edinburgh Dublin Philos. Mag. J. Sci.*, 41(314):221–242, Mar. 1950.

[37] M. Fuchs and M. Scheffler. Ab initio pseudopotentials for electronic structure calculations of poly-atomic systems using density-functional theory. *Comput. Phys. Commun.*, 119(1):67–98, June 1999.

[38] W. Gao, W. Xia, X. Gao, and P. Zhang. Speeding up *gw* calculations to meet the challenge of large scale quasiparticle predictions. *Sci. Rep.*, 6:36849, 2016.

[39] M. Gell-Mann and K. A. Brueckner. Correlation energy of an electron gas at high density. *Phys. Rev.*, 106(2):364–368, Apr. 1957.

[40] P. Giannozzi, O. Andreussi, T. Brumme, O. Bunau, M. B. Nardelli, M. Calandra, R. Car, C. Cavazzoni, D. Ceresoli, M. Cococcioni, N. Colonna, I. Carnimeo, A. D. Corso, S. de Gironcoli, P. Delugas, R. A. DiStasio, A. Ferretti, A. Floris, G. Fratesi, G. Fugallo, R. Gebauer, U. Gerstmann, F. Giustino, T. Gorni, J. Jia, M. Kawamura, H.-Y. Ko, A. Kokalj, E. Küçükbenli, M. Lazzeri, M. Marsili, N. Marzari, F. Mauri, N. L. Nguyen, H.-V. Nguyen, A. O. de-la Roza, L. Paulatto, S. Poncé, D. Rocca, R. Sabatini, B. Santra, M. Schlipf, A. P. Seitsonen, A. Smogunov, I. Timrov, T. Thonhauser, P. Umari, N. Vast, X. Wu, and S. Baroni. Advanced capabilities for materials modelling with quantum ESPRESSO. *J. Phys.: Condens. Matter*, 29(46):465901, Oct. 2017.

[41] P. Giannozzi, S. Baroni, N. Bonini, M. Calandra, R. Car, C. Cavazzoni, D. Ceresoli, G. L. Chiarotti, M. Cococcioni, I. Dabo, et al. Quantum espresso: a modular and open-source software project for quantum simulations of materials. *J. Phys.: Condens. Matter*, 21(39):395502, 2009.

[42] P. Giannozzi, S. de Gironcoli, P. Pavone, and S. Baroni. Ab initiocalculation of phonon dispersions in semiconductors. *Phys. Rev. B*, 43(9):7231–7242, Mar. 1991.

[43] F. Giustino. Electron-phonon interactions from first principles. *Rev. Mod. Phys.*, 89(1):015003, Feb. 2017.

[44] F. Giustino, M. L. Cohen, and S. G. Louie. Electron-phonon interaction using wannier functions. *Phys. Rev. B*, 76(16):165108, Oct. 2007.

[45] F. Giustino, S. G. Louie, and M. L. Cohen. Electron-phonon renormalization of the direct band gap of diamond. *Phys. Rev. Lett.*, 105(26):265501, Dec. 2010.

[46] R. W. Godby, M. Schlüter, and L. Sham. Self-energy operators and exchange-correlation potentials in semiconductors. *Phys. Rev. B*, 37(17):10159, June 1988.

[47] D. Golze, M. Dvorak, and P. Rinke. The GW compendium: A practical guide to theoretical photoemission spectroscopy. *Front. Chem.*, 7, July 2019.

[48] X. Gonze, B. Amadon, G. Antonius, F. Arnardi, L. Baguet, J.-M. Beuken, J. Bieder, F. Bottin, J. Bouchet, E. Bousquet, et al. The abinit project: Impact, environment and recent developments. *Comput. Phys. Commun.*, 248:107042, Mar. 2020.

[49] X. Gonze, P. Boulanger, and M. Côté. Theoretical approaches to the temperature and zero-point motion effects on the electronic band structure. *Ann. Phys.*, 523(1-2):168–178, Nov. 2011.

[50] A. M. Goodman. Photoemission of electrons and holes into silicon nitride. *Appl. Phys. Lett.*, 13(8):275–277, 1968.

[51] M. Govoni and G. Galli. Large scale GW calculations. *J. Chem. Theory Comput.*, 11(6):2680–2696, May 2015.

[52] M. Govoni and G. Galli. GW100: Comparison of methods and accuracy of results obtained with the WEST code. *J. Chem. Theory Comput.*, 14(4):1895–1909, Feb. 2018.

[53] D. Griffiths. *Introduction to quantum mechanics*. Cambridge University Press, Cambridge, 2017.

[54] V. A. Gritsenko, A. V. Shaposhnikov, W. Kwok, H. Wong, and G. M. Jidomirov. Valence band offset at silicon/silicon nitride and silicon nitride/silicon oxide interfaces. *Thin Solid Films*, 437(1):135–139, 2003.

[55] E. K. U. Gross, E. Runge, and O. Heinonen. *Many-particle theory.* A. Hilger, Bristol Philadelphia, 1991.

[56] F. Gygi and A. Baldereschi. Self-consistent hartree-fock and screened-exchange calculations in solids: Application to silicon. *Phys. Rev. B*, 34(6):4405–4408, Sept. 1986.

[57] D. R. Hamann. Optimized norm-conserving vanderbilt pseudopotentials. *Phys. Rev. B*, 88(8):085117, 2013.

[58] D. R. Hamann, M. Schlüter, and C. Chiang. Norm-conserving pseudopotentials. *Phys. Rev. Lett.*, 43(20):1494–1497, Nov. 1979.

[59] D. R. Hartree. The wave mechanics of an atom with a non-coulomb central field. part II. some results and discussion. *Math. Proc. Cambridge Philos. Soc.*, 24(1):111–132, Jan. 1928.

[60] D. R. Hartree and W. Hartree. Self-consistent field, with exchange, for beryllium. *Proc. R. Soc. London A - Math Phys. Sci.*, 150(869):9–33, May 1935.

[61] L. Hedin. New method for calculating the one-particle green's function with application to the electron-gas problem. *Phys. Rev.*, 139(3A):A796–A823, Aug. 1965.

[62] M. Higuchi, S. Sugawa, E. Ikenaga, J. Ushio, H. Nohira, T. Maruizumi, A. Teramoto, T. Ohmi, and T. Hattori. Subnitride and valence band offset at Si_3N_4/Si interface formed using nitrogen-hydrogen radicals. *Appl. Phys. Lett.*, 90(12):123114, 2007.

[63] P. Hohenberg and W. Kohn. Inhomogeneous electron gas. *Phys. Rev.*, 136(3B):B864–B871, Nov. 1964.

[64] M. S. Hybertsen and S. G. Louie. Electron correlation and the band gap in ionic crystals. *Phys. Rev. B*, 32:7005–7008, Nov. 1985.

[65] M. S. Hybertsen and S. G. Louie. First-principles theory of quasiparticles: Calculation of band gaps in semiconductors and insulators. *Phys. Rev. Lett.*, 55(13):1418–1421, Sept. 1985.

[66] M. S. Hybertsen and S. G. Louie. Electron correlation in semiconductors and insulators: Band gaps and quasiparticle energies. *Phys. Rev. B*, 34(8):5390, 1986.

[67] E. R. D. J. III. *NIST Computational Chemistry Comparison and Benchmark Database, NIST Standard Reference Database Number 101, Release 18*, 2016.

[68] F. Karsai, M. Engel, E. Flage-Larsen, and G. Kresse. Electron–phonon coupling in semiconductors within the *gw* approximation. *New J. Phys.*, 20(12):123008, 2018.

[69] J. W. Keister, J. E. Rowe, J. J. Kolodziej, H. Niimi, T. E. Madey, and G. Lucovsky. Band offsets for ultrathin SiO_2 and Si_3N_4 films on Si(111) and Si(100) from photoemission spectroscopy. *J. Vac. Sci. Technol., B: Microelectron. Nanometer Struct.–Process., Meas., Phenom.*, 17(4):1831–1835, 1999.

[70] C. Kittel. *Introduction to solid state physics*. Wiley, 2005.

[71] W. Kohn and L. J. Sham. Self-consistent equations including exchange and correlation effects. *Phys. Rev.*, 140(4A):A1133–A1138, Nov. 1965.

[72] A. Kundu, M. Govoni, H. Yang, M. Ceriotti, F. Gygi, and G. Galli. Quantum vibronic effects on the electronic properties of solid and molecular carbon. *Phys. Rev. Materials*, 5(7):L070801, July 2021.

[73] H. Lambert and F. Giustino. Ab initioSternheimer-GW method for quasiparticle calculations using plane waves. *Phys. Rev. B*, 88(7):075117, Aug. 2013.

[74] C. Lanczos. An iteration method for the solution of the eigenvalue problem of linear differential and integral operators. *J. Res. Natl. Bur. Stand.*, 45(4):255, Oct. 1950.

[75] Z. Li, G. Antonius, M. Wu, H. Felipe, and S. G. Louie. Electron-phonon coupling from ab initio linear-response theory within the *gw* method: Correlation-enhanced interactions and superconductivity in $Ba_{1-x}K_xBiO_3$. *Phys. Rev. Lett.*, 122(18):186402, May 2019.

[76] Z. Li, M. Wu, Y.-H. Chan, and S. G. Louie. Unmasking the origin of kinks in the photoemission spectra of cuprate superconductors. *Phys. Rev. Lett.*, 126(14):146401, Apr. 2021.

[77] D. L. Lichtenberger, K. W. Nebesny, C. D. Ray, D. R. Huffman, and L. D. Lamb. Valence and core photoelectron spectroscopy of c60, buckminsterfullerene. *Chem. Phys. Lett.*, 176(2):203–208, Jan. 1991.

[78] V. L. Lignères and E. A. Carter. An introduction to orbital-free density functional theory. In *Handbook of Materials Modeling*, pages 137–148. Springer Netherlands, 2005.

[79] J. Lindhard. On the properties of a gas of charged particles. *Dan. Vid. Selsk Mat.-Fys. Medd.*, 28:8, 1954.

[80] E. P. J. Linstrom and W. G. Mallard. *NIST Chemistry WebBook, NIST Standard Reference Database Number 69, National Institute of Standards and Technology, Gaithersburg MD, 20899.*

[81] S. Logothetidis, J. Petalas, H. Polatoglou, and D. Fuchs. Origin and temperature dependence of the first direct gap of diamond. *Phys. Rev. B*, 46(8):4483, Aug. 1992.

[82] D. Lu, F. Gygi, and G. Galli. Dielectric properties of ice and liquid water from first-principles calculations. *Phys. Rev. Lett.*, 100:147601, Apr. 2008.

[83] D. Lu, Y. Li, D. Rocca, and G. Galli. Ab initio calculation of van der waals bonded molecular crystals. *Phys. Rev. Lett.*, 102:206411, May 2009.

[84] H. Ma, M. Govoni, F. Gygi, and G. Galli. A finite-field approach for gw calculations beyond the random phase approximation. *J. Chem. Theory Comput.*, 15(1):154–164, Dec. 2018.

[85] J. Ma, A. S. Nissimagoudar, and W. Li. First-principles study of electron and hole mobilities of si and GaAs. *Phys. Rev. B*, 97(4):045201, Jan. 2018.

[86] E. Maggio, P. Liu, M. J. van Setten, and G. Kresse. GW 100: a plane wave perspective for small molecules. *J. Chem. Theory Comput.*, 13(2):635–648, 2017.

[87] G. D. Mahan. *Many-Particle Physics*. Springer US, Oct. 2000.

[88] A. A. Maradudin and S. H. Vosko. Symmetry properties of the normal vibrations of a crystal. *Rev. Mod. Phys.*, 40(1):1–37, Jan. 1968.

[89] A. Marini, C. Hogan, M. Grüning, and D. Varsano. Yambo: an ab initio tool for excited state calculations. *Comput. Phys. Commun.*, 180(8):1392–1403, Aug. 2009.

[90] R. M. Martin. *Electronic structure : basic theory and practical methods*. Cambridge University Press, Cambridge, UK New York, 2004.

[91] R. M. Martin, L. Reining, and D. M. Ceperley. *Interacting Electrons*. Cambridge University Press, June 2016.

[92] R. L. McAvoy, M. Govoni, and G. Galli. Coupling first-principles calculations of electron–electron and electron–phonon scattering, and applications to carbon-based nanostructures. *J. Chem. Theory Comput.*, 14(12):6269–6275, Oct. 2018.

[93] A. Miglio, V. Brousseau-Couture, E. Godbout, G. Antonius, Y.-H. Chan, S. G. Louie, M. Côté, M. Giantomassi, and X. Gonze. Predominance of non-adiabatic effects in zero-point renormalization of the electronic band gap. *npj Comput. Mater.*, 6(1):1–8, Nov. 2020.

[94] B. Monserrat. Correlation effects on electron-phonon coupling in semiconductors: Many-body theory along thermal lines. *Phys. Rev. B*, 93(10):100301, 2016.

[95] B. Monserrat. Electron–phonon coupling from finite differences. *J. Phys.: Condens. Matter*, 30(8):083001, Feb. 2018.

[96] B. Monserrat and R. Needs. Comparing electron-phonon coupling strength in diamond, silicon, and silicon carbide: First-principles study. *Phys. Rev. B*, 89(21):214304, June 2014.

[97] H.-V. Nguyen and S. de Gironcoli. Efficient calculation of exact exchange and rpa correlation energies in the adiabatic-connection fluctuation-dissipation theory. *Phys. Rev. B*, 79(20):205114, May 2009.

[98] H.-V. Nguyen, T. A. Pham, D. Rocca, and G. Galli. Improving accuracy and efficiency of calculations of photoemission spectra within the many-body perturbation theory. *Phys. Rev. B*, 85(8):081101, Feb. 2012.

[99] N. L. Nguyen, H. Ma, M. Govoni, F. Gygi, and G. Galli. Finite-field approach to solving the bethe-salpeter equation. *Phys. Rev. Lett.*, 122(23):237402, June 2019.

[100] G. Onida, L. Reining, and A. Rubio. Electronic excitations: density-functional versus many-body green's-function approaches. *Rev. Mod. Phys.*, 74(2):601–659, June 2002.

[101] K. P. O'donnell and X. Chen. Temperature dependence of semiconductor band gaps. *Appl. Phys. Lett.*, 58(25):2924–2926, June 1991.

[102] W. Pauli. Über den zusammenhang des abschlusses der elektronengruppen im atom mit der komplexstruktur der spektren. *Z. Physik*, 31(1):765–783, Feb. 1925.

[103] J. P. Perdew, K. Burke, and M. Ernzerhof. Generalized gradient approximation made simple. *Phys. Rev. Lett.*, 77:3865–3868, Oct. 1996.

[104] J. P. Perdew, M. Ernzerhof, and K. Burke. Rationale for mixing exact exchange with density functional approximations. *J. Chem. Phys.*, 105(22):9982–9985, Dec. 1996.

[105] J. P. Perdew and A. Zunger. Self-interaction correction to density-functional approximations for many-electron systems. *Phys. Rev. B*, 23(10):5048, May 1981.

[106] T. A. Pham, T. Li, H.-V. Nguyen, S. Shankar, F. Gygi, and G. Galli. Band offsets and dielectric properties of the amorphous si3n4/si(100) interface: A first-principles study. *Appl. Phys. Lett.*, 102(24):241603, June 2013.

[107] T. A. Pham, H.-V. Nguyen, D. Rocca, and G. Galli. GW calculations using the spectral decomposition of the dielectric matrix: Verification, validation, and comparison of methods. *Phys. Rev. B*, 87(15):155148, Apr. 2013.

[108] G. Pizzi, V. Vitale, R. Arita, S. Blügel, F. Freimuth, G. Géranton, M. Gibertini, D. Gresch, C. Johnson, T. Koretsune, J. Ibañez-Azpiroz, H. Lee, J.-M. Lihm, D. Marchand, A. Marrazzo, Y. Mokrousov, J. I. Mustafa, Y. Nohara, Y. Nomura, L. Paulatto, S. Poncé, T. Ponweiser, J. Qiao, F. Thöle, S. S. Tsirkin, M. Wierzbowska, N. Marzari, D. Vanderbilt, I. Souza, A. A. Mostofi, and J. R. Yates. Wannier90 as a community code: new features and applications. *J. Phys.: Condens. Matter*, 32(16):165902, Jan. 2020.

[109] S. Poncé, G. Antonius, Y. Gillet, P. Boulanger, J. L. Janssen, A. Marini, M. Côté, and X. Gonze. Temperature dependence of electronic eigenenergies in the adiabatic harmonic approximation. *Phys. Rev. B*, 90(21):214304, Dec. 2014.

[110] S. Poncé, Y. Gillet, J. L. Janssen, A. Marini, M. Verstraete, and X. Gonze. Temperature dependence of the electronic structure of semiconductors and insulators. *J. Chem. Phys.*, 143(10):102813, Sept. 2015.

[111] S. Poncé, E. Margine, C. Verdi, and F. Giustino. EPW: Electron–phonon coupling, transport and superconducting properties using maximally localized wannier functions. *Comput. Phys. Commun.*, 209:116–133, Dec. 2016.

[112] X. Qian, P. Umari, and N. Marzari. First-principles investigation of organic photovoltaic materialsC60, c70, [c60]PCBM, and bis-[c60]PCBMusing a many-bodyG0w0-lanczos approach. *Phys. Rev. B*, 91(24):245105, June 2015.

[113] R. Ramírez, C. P. Herrero, and E. R. Hernández. Path-integral molecular dynamics simulation of diamond. *Phys. Rev. B*, 73(24):245202, June 2006.

[114] R. Ramírez, C. P. Herrero, E. R. Hernández, and M. Cardona. Path-integral molecular dynamics simulation of3c-SiC. *Phys. Rev. B*, 77(4):045210, Jan. 2008.

[115] D. Rocca. *Time-dependent density functional perturbation theory: new algorithms with applications to molecular spectra*. PhD thesis, Scuola Internazionale Superiore di Studi Avanzati, Oct. 2007.

[116] D. Rocca. Random-phase approximation correlation energies from lanczos chains and an optimal basis set: Theory and applications to the benzene dimer. *J. Chem. Phys.*, 140(18):18A501, May 2014.

[117] D. Rocca, R. Gebauer, Y. Saad, and S. Baroni. Turbo charging time-dependent density-functional theory with lanczos chains. *J. Chem. Phys.*, 128(15):154105, Apr. 2008.

[118] D. Rocca, D. Lu, and G. Galli. Ab initio calculations of optical absorption spectra: Solution of the bethe–salpeter equation within density matrix perturbation theory. *J. Chem. Phys.*, 133(16):164109, Oct. 2010.

[119] D. Rocca, Y. Ping, R. Gebauer, and G. Galli. Solution of the bethe-salpeter equation without empty electronic states: Application to the absorption spectra of bulk systems. *Phys. Rev. B*, 85(4):045116, Jan. 2012.

[120] M. Rohlfing and S. G. Louie. Electron-hole excitations and optical spectra from first principles. *Phys. Rev. B*, 62(8):4927–4944, Aug. 2000.

[121] G. Samsonidze, M. Jain, J. Deslippe, M. L. Cohen, and S. G. Louie. Simple approximate physical orbitals for GW quasiparticle calculations. *Phys. Rev. Lett.*, 107(18):186404, 2011.

[122] P. Scherpelz, M. Govoni, I. Hamada, and G. Galli. Implementation and validation of fully relativistic GW calculations: Spin–orbit coupling in molecules, nanocrystals, and solids. *J. Chem. Theory Comput.*, 12(8):3523–3544, July 2016.

[123] M. Schlipf and F. Gygi. Optimization algorithm for the generation of oncv pseudopotentials. *Comput. Phys. Commun.*, 196:36–44, 2015.

[124] E. Schrödinger. An undulatory theory of the mechanics of atoms and molecules. *Phys. Rev.*, 28(6):1049–1070, Dec. 1926.

[125] P. Schwerdtfeger. The pseudopotential approximation in electronic structure theory. *ChemPhysChem*, 12(17):3143–3155, Aug. 2011.

[126] H. Shang and J. Yang. Capturing the electron–phonon renormalization in molecules from first-principles. *J. Phys. Chem. A*, 125(12):2682–2689, Mar. 2021.

[127] C. D. Sherrill and H. F. Schaefer. The configuration interaction method: Advances in highly correlated approaches. In *Advances in Quantum Chemistry*, pages 143–269. Elsevier, 1999.

[128] J. H. Skone, M. Govoni, and G. Galli. Self-consistent hybrid functional for condensed systems. *Phys. Rev. B*, 89(19):195112, May 2014.

[129] J. H. Skone, M. Govoni, and G. Galli. Nonempirical range-separated hybrid functionals for solids and molecules. *Phys. Rev. B*, 93(23):235106, June 2016.

[130] J. C. Slater. The theory of complex spectra. *Phys. Rev.*, 34(10):1293–1322, Nov. 1929.

[131] J. Soininen, J. Rehr, and E. L. Shirley. Electron self-energy calculation using a general multi-pole approximation. *J. Phys.: Condens. Matter*, 15(17):2573, 2003.

[132] R. Sternheimer. Electronic polarizabilities of ions from the hartree-fock wave functions. *Phys. Rev.*, 96(4):951, 1954.

[133] G. Strinati, H. Mattausch, and W. Hanke. Dynamical correlation effects on the quasiparticle bloch states of a covalent crystal. *Phys. Rev. Lett.*, 45(4):290, 1980.

[134] G. Strinati, H. Mattausch, and W. Hanke. Dynamical aspects of correlation corrections in a covalent crystal. *Phys. Rev. B*, 25(4):2867, 1982.

[135] D. A. Strubbe, L. Lehtovaara, A. Rubio, M. A. L. Marques, and S. G. Louie. Response functions in TDDFT: Concepts and implementation. In *Fundamentals of Time-Dependent Density Functional Theory*, pages 139–166. Springer Berlin Heidelberg, 2012.

[136] R. Sundararaman and Y. Ping. First-principles electrostatic potentials for reliable alignment at interfaces and defects. *J. Chem. Phys.*, 146(10):104109, 2017.

[137] L. H. Thomas. The calculation of atomic fields. *Math. Proc. Cambridge Philos. Soc.*, 23(5):542–548, Jan. 1927.

[138] A. Tkatchenko and M. Scheffler. Accurate molecular van der waals interactions from ground-state electron density and free-atom reference data. *Phys. Rev. Lett.*, 102(7):073005, Feb. 2009.

[139] N. Troullier and J. L. Martins. Efficient pseudopotentials for plane-wave calculations. *Phys. Rev. B*, 43(3):1993, Jan. 1991.

[140] C. G. Van de Walle and R. M. Martin. Theoretical study of band offsets at semiconductor interfaces. *Phys. Rev. B*, 35:8154–8165, May 1987.

[141] M. van Schilfgaarde, T. Kotani, and S. Faleev. Quasiparticle self-consistent GW theory. *Phys. Rev. Lett.*, 96(22):226402, June 2006.

[142] M. J. van Setten, F. Caruso, S. Sharifzadeh, X. Ren, M. Scheffler, F. Liu, J. Lischner, L. Lin, J. R. Deslippe, S. G. Louie, C. Yang, F. Weigend, J. B. Neaton, F. Evers, and P. Rinke. GW100: Benchmarking g0w0 for molecular systems. *J. Chem. Theory Comput.*, 11(12):5665–5687, Nov. 2015.

[143] H. F. Wilson, F. Gygi, and G. Galli. Efficient iterative method for calculations of dielectric matrices. *Phys. Rev. B*, 78(11):113303, Sept. 2008.

[144] H. F. Wilson, D. Lu, F. Gygi, and G. Galli. Iterative calculations of dielectric eigenvalue spectra. *Phys. Rev. B*, 79(24):245106, June 2009.

[145] N. Wiser. Dielectric constant with local field effects included. *Phys. Rev.*, 129(1):62, 1963.

[146] T. Yamasaki, C. Kaneta, T. Uchiyama, T. Uda, and K. Terakura. Geometric and electronic structures of SiO_2/Si(001) interfaces. *Phys. Rev. B*, 63:115314, Mar. 2001.

[147] H. Yang, M. Govoni, and G. Galli. Improving the efficiency of g0w0 calculations with approximate spectral decompositions of dielectric matrices. *J. Chem. Phys.*, 151(22):224102, Dec. 2019.

[148] H. Yang, M. Govoni, A. Kundu, and G. Galli. Combined first-principles calculations of electron-electron and electron-phonon self-energies in condensed systems, 2021.

[149] J.-J. Zhou, J. Park, I.-T. Lu, I. Maliyov, X. Tong, and M. Bernardi. Perturbo: A software package for ab initio electron–phonon interactions, charge transport and ultrafast dynamics. *Comput. Phys. Commun.*, 264:107970, July 2021.